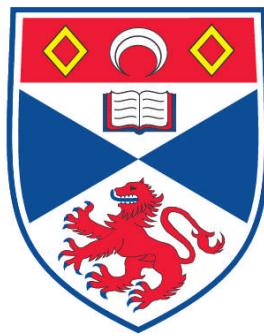


**THE ROLE OF THE PLASMON RESONANCE FOR ENHANCED  
OPTICAL FORCES**

**Martin Ploschner**

**A Thesis Submitted for the Degree of PhD  
at the  
University of St. Andrews**



**2012**

**Full metadata for this item is available in  
Research@StAndrews:FullText  
at:**

**<http://research-repository.st-andrews.ac.uk/>**

**Please use this identifier to cite or link to this item:**

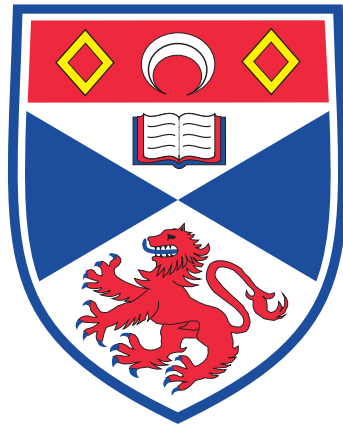
**<http://hdl.handle.net/10023/3189>**

**This item is protected by original copyright**

**This item is licensed under a  
Creative Commons License**

# The role of the plasmon resonance for enhanced optical forces

Martin Plöschner



University  
of  
St Andrews

Thesis submitted for the degree of Doctor of Philosophy at the  
University of St Andrews

May 29, 2012



# Declaration

I, Martin Plöschner, hereby certify that this thesis, which is approximately 30,000 words in length, has been written by me, that it is the record of work carried out by me and that it has not been submitted in any previous application for a higher degree. I was admitted as a research student in August 2008 and as a candidate for the degree of Doctor of Philosophy in August 2008; the higher study for which this is a record was carried out in the University of St Andrews between 2008 and 2012.

Signature of Candidate: ..... Date: .....

---

I hereby certify that the candidate has fulfilled the conditions of the Resolution and Regulations appropriate for the degree of Doctor of Philosophy at the University of St Andrews and that the candidate is qualified to submit this thesis in application for that degree.

Signature of Supervisor: ..... Date: .....

---

In submitting this thesis to the University of St Andrews we understand that we are giving permission for it to be made available for use in accordance with the regulations of the University Library for the time being in force, subject to any copyright vested in the work not being affected thereby. We also understand that the title and abstract will be published, and that a copy of the work may be made and supplied to any bona fide library or research worker, that my thesis will be electronically accessible for personal or research use unless exempt by award of an embargo as requested below, and that the library has the right to migrate my thesis into new electronic forms as required to ensure continued access to the thesis. We have obtained any third-party copyright permissions that may be required in order to allow such access and migration, or have requested the appropriate embargo below. The following is an agreed request by candidate and supervisor regarding the electronic publication of this thesis: Access to Printed copy and electronic publication of thesis through the University of St Andrews.

Signature of Candidate: ..... Signature of Supervisor: .....

Date: .....



# Acknowledgements

I would like to thank both of my supervisors Prof. Kishan Dholakia and Prof. Thomas F. Krauss for their support and encouragement throughout the years. Their unique view on science was a true inspiration during the course of my PhD. I will especially remember the simple, yet far-reaching, questions raised by Thomas and I will never forget the feeling, that everything is possible, after leaving Kishan's office.

Special thanks also go to Tomáš Čížmár, to whom I owe a lot of the ideas presented in this thesis. It was his initiative to use plasmon resonances for bidirectional sorting of gold nanoparticles and it was his support, in moments when I lost the faith, that made it all possible.

I cannot thank enough Michael Mazilu, who spend hours and hours discussing his view of physics with me and who provided immense help when I had some problems with the simulations. Also, I greatly appreciate his "riddles" that I usually solve several years later.

Another special thanks goes to Andrea Di Falco, who spend a lot of time with me in the clean-room, and who later, when I left the clean-room, continued in fabrication of nanoantennas and who provided some of the SEM images presented in this thesis.

I cannot forget on Sebastian Kosmeier, with whom I shared my rage over some unfairly interpreted data in research journals. He also shared many ideas with me which made my life in lab easier. Finally, I have to thank him for proof-reading the thesis.

I also thank Tom Vettenburg who keeps asking questions until you do not have the answer.

Finally, I must thank my wife Michaela who supported me in everything over the past few years.



# List of publications

- **M. Ploschner**, T. Čižmár, M. Mazilu, A. Di Falco and K. Dholakia, "Bidirectional sorting of gold nanoparticles", *Nano Letters*, 12(4):1923–7, 2012  
(Selected for Nature research highlights at <http://www.nature.com/nature/journal/v484/n7393/full/484144e.html>, "Lasers sort particles by size", *Nature*, 484:144–145, 2012)
- **M. Ploschner**, M. Mazilu, T. Čižmár and K. Dholakia, "Passive optical sorting of plasmon nanoparticles: Numerical investigation of optimal illumination", *AIP Conf. Proc.*, 1398:85–87, 2011.
- **M. Ploschner**, M. Mazilu, T. Čižmár and K. Dholakia, "Numerical investigation of passive optical sorting of plasmon nanoparticles", *Optics Express*, 19(15):13922–13933, 2011.
- A. Di Falco, **M. Ploschner**, T. F. Krauss, "Flexible metamaterials at visible wavelengths", *New Journal of Physics*, 12:113006, 2010. <http://www.bbc.co.uk/news/science-environment-11686303>
- **M. Ploschner**, M. Mazilu, T. F. Krauss and K. Dholakia, "Determination of optical forces in the proximity of a nanoantenna", *Proceedings of the SPIE*, 7762:77620L–77620L-9, 2010.
- M. L. Torres-Mapa, L. Angus, **M. Ploschner**, K. Dholakia, F. J. Gunn-Moore, "Transient transfection of mammalian cells using a violet diode laser", *Journal of Biomedical Optics*, 15:041506, 2010.
- **M. Ploschner**, M. Mazilu., T. F. Krauss and K. Dholakia, "Optical forces near a nanoantenna", *Jornal of Nanophotonics*, 4:041570, 2010.
- **M. Ploschner**, A. Di Falco, M. Mazilu and T. F. Krauss, "The potential of single-slit split-ring resonators for optical trapping", *Proceedings of the 3rd International Congress on Advanced Electromagnetic Materials in Microwaves and Optics*, 776–778, 2009.

# Conferences and courses attended

- International Workshop on Theoretical and Computational Nano-Photonics - TaCoNa-Photonics, October 2011, contributed talk
- DPG - Physics School "Nano - Antennas", September 2011, poster

- SPIE conference - Optical Trapping and Optical Micromanipulation VII, San Diego, California, August 2010, contributed talk
- Functionalized plasmonic nanostructures for biosensing, Ascona, April 2010, poster.
- 3rd International Congress on Advanced Electromagnetic Materials in Microwaves and Optics, London, September 2009, poster
- Fourth International Conference on Surface Plasmon Photonics, Amsterdam, June 2009.
- COST MP0604 General Meeting in Aberfoyle, Scotland, May 2009.

# Abstract

Optical manipulation of nanoscale objects is studied with particular emphasis on the role of plasmon resonance for enhancement of optical forces. The thesis provides an introduction to plasmon resonance and its role in confinement of light to a sub-diffraction volume. The strong light confinement and related enhancement of optical forces is then theoretically studied for a special case of nanoantenna supporting plasmon resonances. The calculation of optical forces, based on the Maxwell stress tensor approach, reveals relatively weak optical forces for incident powers that are used in typical realisations of trapping with nanoantenna. The optical forces are so weak that other non-optical effects should be considered to explain the observed trapping. These effects include heating induced convection, thermoporesis and chemical binding.

The thesis also studies the optical effects of plasmon resonances for a fundamentally different application - size-based optical sorting of gold nanoparticles. Here, the plasmon resonances are not utilised for sub-diffraction light confinement but rather for their ability to increase the apparent cross-section of the particles for their respective resonant sizes. Exploiting these resonances, we realise sorting in a system of two counter-propagating evanescent waves, each at different wavelength that selectively guide gold nanoparticles of different sizes in opposite directions. The method is experimentally demonstrated for bidirectional sorting of gold nanoparticles of either 150 or 130 nm in diameter from those of 100 nm in diameter within a mixture.

We conclude the thesis with a numerical study of the optimal beam-shape for optical sorting applications. The developed theoretical framework, based on the force optical eigenmode method, is able to find an illumination of the back-focal plane of the objective such that the force difference between nanoparticles of various sizes in the sample plane is maximised.



*Our imagination is stretched to the utmost, not, as in fiction, to imagine things which are not really there, but just to comprehend those things which are there.*

**Richard P. Feynman**



# CONTENTS

<b>1</b>	<b>Introduction to plasmon resonances</b>	<b>1</b>
1.1	Plasmon resonance . . . . .	2
1.2	Plasmon resonance in metals . . . . .	5
1.3	Field enhancement and heating introduced by plasmon resonance . . . . .	6
1.4	Plasmon resonance of confined plasma . . . . .	9
1.5	Mode volume: metals vs dielectrics . . . . .	12
1.6	Coupling between two resonant structures . . . . .	14
1.7	Outline of the thesis . . . . .	16
<b>2</b>	<b>The enhancement of optical forces using plasmon resonances</b>	<b>19</b>
2.1	Optical forces . . . . .	20
2.2	Optical trapping of small objects . . . . .	22
2.3	Plasmon resonances and the Heisenberg uncertainty principle . . . . .	25
2.4	Fundamental physics of plasmon polaritons . . . . .	28
2.4.1	SPP mode . . . . .	30
2.4.2	LSPP mode . . . . .	33
2.5	Utilisation of LSPP mode for particle sorting . . . . .	35
2.6	Conclusion . . . . .	36
<b>3</b>	<b>Enhanced optical forces and heating near plasmon resonant nanoantenna</b>	<b>37</b>
3.1	The theory of the optical forces . . . . .	39
3.1.1	The Maxwell stress tensor method . . . . .	39
3.1.2	Model for solving $E_i$ and $H_i$ . . . . .	41
3.1.3	Validation of the model . . . . .	45
3.2	Optical forces near a nanoantenna . . . . .	49
3.2.1	Case 1: normal incidence . . . . .	50
3.2.2	Case 2: total internal reflection incidence . . . . .	55
3.2.3	Comparison of the two nanoantenna geometries . . . . .	59
3.2.4	Heating issues . . . . .	60
3.3	Attempts to differentiate heating and optical effects . . . . .	61
3.4	Conclusion . . . . .	64

<b>4</b>	<b>Plasmon resonances in optical sorting</b>	<b>65</b>
4.1	Why does the size of a nanoparticle matter? . . . . .	66
4.2	Methods for sorting nanoparticles by size . . . . .	67
4.3	Bidirectional sorting of gold nanoparticles . . . . .	68
4.3.1	Selection of operating wavelengths . . . . .	69
4.3.2	Forces and velocities in evanescent field . . . . .	71
4.3.3	The experimental setup . . . . .	73
4.3.4	Results of the sorting experiment . . . . .	75
4.3.5	Resolution of the method . . . . .	79
4.3.6	Further improvements . . . . .	81
4.3.7	Limitations of the method . . . . .	82
4.4	Conclusion . . . . .	84
<b>5</b>	<b>Optimisation of optical sorting of gold nanoparticles</b>	<b>87</b>
5.1	The beam-shape for the optimal push force . . . . .	88
5.2	Numerical modelling . . . . .	90
5.3	Heating effects in the system . . . . .	91
5.4	Optimising the force difference in the region of interest (ROI) . . . . .	94
5.5	Deflection of particles in a microfluidic channel . . . . .	98
5.6	Conclusion . . . . .	100
<b>6</b>	<b>Summary and Outlook</b>	<b>103</b>
	<b>Appendix A Dispersion relation of SPP mode</b>	<b>107</b>
	<b>Appendix B Derivation of LSPP mode</b>	<b>111</b>

# Chapter 1

## Introduction to plasmon resonances

We have all been there as children - summer afternoon playground with fragrant flowers in the air, glowing sunshine, a swing-set, slide, sandbox and laughing. And although I did not know it at the time, for me, one thing in particular on this playground, would become the topic of my PhD thesis - the swing. Of course not the swing itself, but the physical phenomenon driving its motion - the resonance.

Resonances are all around us. They are a cornerstone for a myriad of technological advances of the last century and as such they have changed our lives more than we realise. Simple tuning of your favourite TV or radio show requires you to match the resonance condition of an LC circuit to the transmission frequency of the airing show. A microwave oven, probably the most common cavity resonator, found its way to almost all hassle-free cooking households. Knowledge of resonances allows engineers to build modern oil rigs, bridges and skyscrapers in a way that avoids destructive resonances with ocean waves, wind and earthquakes. Our voice, unique to each of us, is nothing else than the resonance of vocal cords. And with so many parameters determining the resonance of vocal cords; their shape, tightness and size; not a single voice ever was the same. We spontaneously create the resonance condition without thinking about it. However, a small inflammation from a cold can bring the resonance to frequencies we are not used to generate and this might result in temporary loss of our voice. The resonances are also at the heart of music - centrepiece of human creativity and art. Basically all musical instruments rely on resonances.

The Earth itself is full of resonances. Tidal waves resonantly trapped between the coast and continental shelf can greatly increase the tidal range in some places. The space between Earth's surface and ionosphere is effectively also a resonant cavity. This cavity is naturally excited by lightning in many storms raging around the globe at any moment and accounts for sustained peaks in electromagnetic spectrum of Earth. This might sound boring at first sight, but the same resonances are the key trigger for various types of upper atmospheric lightning effects such as sprites, elves and jets. The resonances in ionosphere are also absolutely crucial for radio communication.

An even more astonishing example of a resonance is the relationship between one particular carpenter bee and the orphium frutescens plant. Here, the goal of the plant is to deliver its pollen to another plant of the same species without wasting too much pollen in the process. The goal of the bee is to eat. The solution for both is breathtaking. When the carpenter bee lands on the flower, the rate of beating of its wings changes to a frequency that is resonant with the stamens containing the pollen. The violent oscillation generated by resonance condition unlocks the stamens and releases the pollen. Since no other insect has the correct beating frequency and the food gain for bee is high, the pollen is delivered to another plant of the same species in a very efficient way.

## 1.1 Plasmon resonance

The paragraphs above should give you an idea of how widespread the resonances are in our world and how useful they can be. It comes as no surprise then, that even the cutting-edge research today still studies and explores various resonance phenomena and their potential applications. In fact, most of the scientific journals have at least one article in each issue studying some type of resonance effect.

There is one type of resonance, in particular, that has become popular in the last decade - the resonance of a plasma. It is not a new phenomenon. Its physics has been known since the advent of radio communication as the plasma oscillations in the ionosphere are essential for propagation of radio waves. The radio station uses the ionosphere as a mirror to communicate with receiver beyond the horizon. In essence, free electrons in the ionosphere move under the influence of radio waves and this movement itself generates radio waves that are reflected back to Earth (more details in Section 1.3).<sup>1</sup>

However, not all radio waves are reflected back. Some radio frequencies can easily propagate through the ionosphere into outer space. These frequencies are obviously essential for communication with various satellites around the Earth. The critical frequency, for which the behaviour of the ionosphere changes from mirror-like to transparent, is called the plasma frequency. It is a natural resonance of a plasma system.

To understand the principle of this type of resonance, let us consider a box filled with a plasma. In the first approximation, we model the plasma as a grid of positive ions that are fixed in position (they are significantly heavier than the electrons) surrounded by free electron gas. If we switch on an electric field  $E_x$  (x-component), electrons will move to one side of the box leaving positive ions behind. When we now switch off the field  $E_x$ , the electrons will move towards the positive ions, miss

---

<sup>1</sup>There is quite an interesting twist to this story and you might have noticed this in your everyday life. Some radio stations with frequency around 10 MHz have crystal clear signal during the night, but they almost disappear during the day. The explanation is quite simple. During the day, additional ionisation processes appear in lower ionosphere and create the so called D-layer. This layer is very lossy for the radio-waves (any movement of electrons induced by radio wave is quickly damped by electron collisions). Some stations correct for this by changing the power output of the transmitter during the day and night.

them and go to the opposite side of the box until they lose all their kinetic energy. At that point they will reverse and go back to their original position. Fig. 1.1 shows the initial unperturbed system (electron cloud confined between boundaries  $a_1$  and

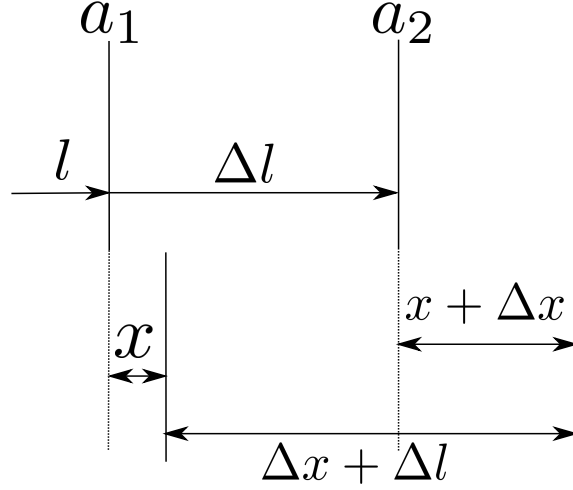


Fig. 1.1: The electron cloud between lines  $a_1$  and  $a_2$  is displaced by the distance  $x$  from  $a_1$  and by the distance  $x + \Delta x$  from  $a_2$ . This leads to the change of electron density in the cloud which is responsible for linear restoring force acting on the displaced electrons.

$a_2$ ) and the system where the electrons cloud is displaced by a distance  $x$  from  $a_1$  and by  $x + \Delta x$  from  $a_2$ . Please note that this means that the density of the electron cloud after the displacement is changed. If we denote the density of the electron cloud in the unperturbed state by  $n_0$  then the number of electrons confined between  $a_1$  and  $a_2$  is proportional to  $n_0 \Delta l$ . After the displacement, the same number of electrons must be confined within a region  $\Delta l + \Delta x$ , which implies that the density of the electron cloud changes to

$$n = \frac{n_0 \Delta l}{\Delta l + \Delta x}. \quad (1.1)$$

If we assume only a small change in the density of the electron cloud we can write the resulting density as

$$n \approx n_0 \left( 1 - \frac{\Delta x}{\Delta l} \right). \quad (1.2)$$

As the positive ions are assumed to be fixed, we can write the charge density at any point as

$$\rho = n_0 e - n_0 e \left( 1 - \frac{\Delta x}{\Delta l} \right) = n_0 e \frac{\Delta x}{\Delta l}, \quad (1.3)$$

where  $e$  is the elementary charge of an electron. The charge density is further related to the electric field by

$$\nabla \cdot E = \frac{\rho}{\epsilon_0}. \quad (1.4)$$

For one-dimensional problem and assuming that there are no other fields than those present due to the displacement of the electron cloud leads to the following differential equation

$$\frac{dE}{dl} = \frac{n_0 e}{\epsilon_0} \frac{dx}{dl}. \quad (1.5)$$

Integrating and using the initial condition  $E = 0$  for  $x = 0$  gives

$$E = \frac{n_0 e}{\epsilon_0} x, \quad (1.6)$$

which finally leads to the force acting on a displaced electron

$$F = -\frac{n_0 e^2}{\epsilon_0} x. \quad (1.7)$$

This is nothing else than the harmonic oscillator described by the following equation of motion

$$m_e \frac{\partial^2 x}{\partial t^2} + \frac{n_0 e^2}{\epsilon_0} x = 0 \quad (1.8)$$

with natural frequency, called plasma frequency, equal to

$$\omega_p^2 = \frac{n_0 e^2}{\epsilon_0 m_e}, \quad (1.9)$$

where  $n_0$  is the density of electrons in the unperturbed system,  $m_e$  is the mass of the electron,  $e$  is the elementary charge of the electron and  $\epsilon_0$  is the permittivity of vacuum. As the oscillation of the electrons is collective, it can be treated as a quasi-particle termed a **plasmon**. In this simple example,  $x$  is the displacement of the plasmon quasi-particle from equilibrium position and the  $\omega_p$  can be seen as plasmon frequency. Driving the system at this frequency would result in a plasmon resonance. At this point it is important to note that we have derived Eq. (1.8) in a simplified situation that results in a restoring force linearly proportional to the displacement. In the realistic systems, this is no longer necessarily satisfied and the anharmonic terms have to be included. However as the first two chapters attempt to describe the qualitative nature of our problem, we will neglect the anharmonic terms for the moment. This leaves us with three parameters of interest for our resonant systems - natural resonance frequency  $\omega_n$  (also called a plasmon frequency in our situation), the damping term  $\Gamma$  and the force  $F$  driving the system.

Plasmon resonances can exist in any medium which can be described as a plasma. Apart from ionised gas, plasmon resonances also occur in metals, metal alloys and doped semiconductors. Noble metals in particular are widely regarded as the best available plasmonic materials [1] and, as a result, many applications harvesting the effects of plasmon resonances are based on gold and silver nanostructures.<sup>2</sup> For this reason let us now turn our attention to plasmon resonances in metals.

---

<sup>2</sup>In the course of my PhD, new and possibly more effective plasmonic materials have been proposed. One of the most prominent candidates for this next generation plasmonics is graphene. However, to date the plasmon resonance in graphene was predicted only theoretically and not observed experimentally [2].

## 1.2 Plasmon resonance in metals

The model of plasma oscillations developed above needs to be significantly modified in realistic metal systems. First of all, the thermal motion of ions leads to electron scattering, which results in damping of the system. We can account for damping by introducing the damping term  $\Gamma = v_F/l$ , where  $v_F$  is the Fermi velocity, which describes the velocity of electrons that participate in electrical conduction, and  $l$  is the mean free path of electrons between scattering events. This means that  $\Gamma$  describes the frequency of collisions experienced by an electron. Secondly, in a damped oscillator without an external driving force, the oscillations quickly vanish. As we are interested in sustained oscillations in metals, we need to drive the system with an external field. After introducing the driving force and damping, the modified equation of motion becomes

$$\frac{\partial^2 x}{\partial t^2} + \Gamma \frac{\partial x}{\partial t} + \omega_p^2 x = \frac{(-eE_x)}{m_e} \cos(\omega t + \Delta), \quad (1.10)$$

which is just an equation of the driven damped oscillator, where  $\Gamma$  is the damping term,  $\Delta$  is the phase of the driving force and  $E_x$  is the electric field in x-direction. The steady-state solution (remember, we are interested in sustained oscillations in metals and not transient effects) of this equation results in the following equation for displacement

$$x = A(-eE_x) \cos(\omega t + \Delta + \theta), \quad (1.11)$$

where  $A$  is the amplitude of oscillation and  $\theta$  is the phase shift of collective electron oscillation (plasmon) with respect to driving force. The square of the amplitude of oscillation has the following form

$$A^2 = \frac{1}{m_e^2 [(\omega^2 - \omega_p^2)^2 + \Gamma^2 \omega^2]}. \quad (1.12)$$

and the phase of the plasmon quasi-particle with respect to the driving field is given by

$$\theta = \arctan \left( \frac{-\Gamma \omega}{\omega_p^2 - \omega^2} \right). \quad (1.13)$$

The power dissipated by the system can also be easily calculated from the drag force  $F_{drag} = -m_e \Gamma \dot{x}$ . Using  $P = F_{drag} \dot{x}$  and averaging over one optical cycle, we can write the dissipated power as

$$P = -m_e \Gamma \dot{x}^2 = -\frac{\Gamma}{2m_e} \frac{(eE_x)^2 \omega^2}{[(\omega^2 - \omega_p^2)^2 + \Gamma^2 \omega^2]}, \quad (1.14)$$

where the minus sign appears due to power being dissipated in the system.

This is the basic physics of the plasmon resonance in metals - completely analogous to the resonance of the driven damped oscillator.

### 1.3 Field enhancement and heating introduced by plasmon resonance

The natural frequency of plasma, given by Eq. (1.9), increases as the electron density  $n_0$  becomes larger. Since the density of electrons in metals is much higher than the density of electrons in the ionosphere, we expect a shift of resonance frequency in metals from radio waves to much shorter wavelengths. If we take gold as our model system and use a free electron density of  $n_0 = 5.9 \times 10^{28} \text{ m}^{-3}$  and damping constant  $\Gamma = 1.075 \times 10^{14} \text{ s}^{-1}$  as input parameters for Eq. (1.12), we find a resonance peak that is shown on Fig. 1.2a. This shows that the plasma frequency of gold, indicative

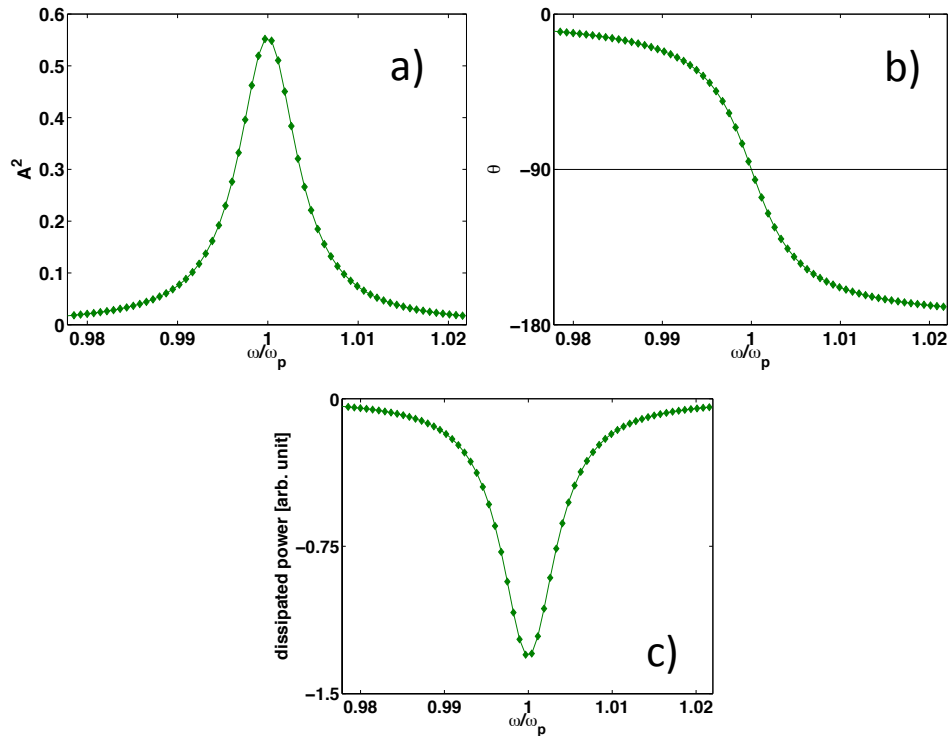


Fig. 1.2: (a) The plasma frequency was calculated for a Drude-Sommerfeld model of gold with free electron density of  $n_0 = 5.9 \times 10^{28} \text{ m}^{-3}$  and damping term  $\Gamma = 1.075 \times 10^{14} \text{ s}^{-1}$ . The plasma frequency, in this case, lies in the ultraviolet range of the spectrum; (b) Phase delay of electron cloud displacement with respect to the phase of the driving electric field (the anti-phase shift of  $\pi$  is not included for clarity). For low frequencies the electrons are able to follow the changes of the field and they reflect the light well; at resonance the phase delay is  $\pi/2$ , which ensures maximum coupling of energy into the oscillating system; for even higher frequencies, electrons lose the ability to follow the changes of the field and the metal becomes transparent; (c) The dissipated power  $P$  calculated using Eq. 1.14 shows that the maximum amplitude of oscillator and the maximum heating appears for the same frequency (only valid for small damping  $\Gamma$ ).

of most of the metals, lies in the ultraviolet range. But what is the physical meaning of this frequency and how does the metal behave below and above this frequency?

To answer these questions let us study Eq. (1.13) in more detail. Fig. 1.2b shows the phase  $\theta$  of the electron cloud displacement as a function of the driving frequency  $\omega$  for the same input parameters  $\omega_p$  and  $\Gamma$  as above. Considering the negative charge of the electron we can see that for the low frequencies the displacement of the electron cloud is in antiphase with the driving field. This essentially means that the field inside the metal is completely cancelled out at any given moment. If the variable field is normal incident onto the metal surface, then the electrons at the surface screen the field and the field cannot penetrate further into metal. Without losses, no field would get into the metal and all light would be reflected back resulting in a perfect electric conductor. Because the conductivity of metals is large, they reflect light very well, which is one of the reasons why we use silver mirrors in the lab.

As we increase the frequency further, the electrons are no longer able to follow the quickly changing field and their displacement picks up a phase delay with respect to the driving field. At exactly the plasmon frequency ( $\omega_p$ ) the phase delay is  $\pi/2$  radians (Figure. 1.3). This is quite unexpected result because it means that the

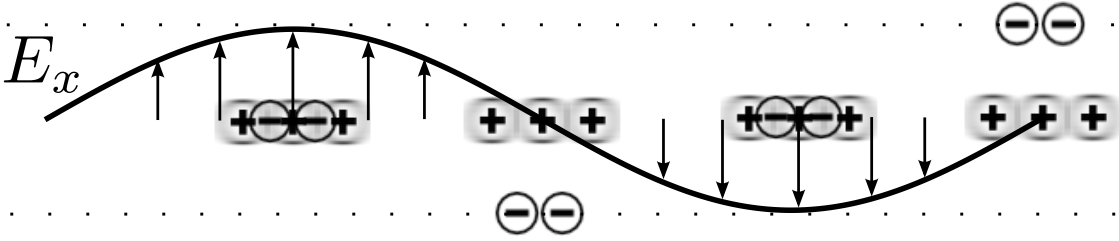


Fig. 1.3: The displacement of electron cloud is shifted by  $\pi/2$  with respect to the driving electric field at the resonance frequency. This means that the induced electric field is maximised for zero external field amplitude (this does not alter the fact that the field averaged over one optical cycle is maximised for resonant condition). The phase shift of  $\pi/2$  ensures that the current density always points in the same direction (remember that current density is defined to have opposite direction to the electron velocity) as the driving field. This guarantees maximum coupling of energy into the oscillating system.

induced field is maximised for zero external field amplitude. In order to understand the importance of the  $\pi/2$  phase factor, let us first calculate the current density inside the metal from Eq. (1.11) using

$$j_x = -n_0 e \frac{dx}{dt}. \quad (1.15)$$

Interestingly, if we express the sine function resulting from the derivative of Eq. (1.11) as a cosine (shift of  $\pi/2$ ), we obtain

$$j_x = n_0 e^2 E_x A \cos(\omega t + \Delta), \quad (1.16)$$

which means that the driving field  $E_x \cos(\omega t + \Delta)$  in Eq. (1.10) and the current density  $j_x$  are in phase. They always point in the same direction. This means that the electrons are always pushed in the direction they are moving (they always have the wind on their back). This makes perfect sense, because we should be able to couple the maximum amount of energy into the oscillating system at its resonance frequency and this can only happen when the above condition is met. Why?

We know that all the oscillating systems are very efficient in transforming kinetic energy into potential energy and vice versa. Kinetic energy is related to the magnitude of velocity and the potential energy is related to the magnitude of displacement. For undamped systems, those two types of energy are transformed into each other without losses. In the damped system, losses limit the transformation. Part of the coupled (kinetic) energy is lost in the damping process and this means that maximum kinetic and maximum potential energy are not equal any more. It thus makes sense to maximise kinetic energy of the oscillator, rather than its potential energy, as the kinetic energy represents the total energy coupled into the oscillator. This means that in order to maximise the energy coupled into damped oscillator (to satisfy resonant condition), we have to maximise the amplitude of velocity (current) and not the amplitude of displacement. And this is exactly what happens in the situation described above.<sup>3</sup>

The ability of the metal resonator to store the energy from the external electromagnetic field is at the core of success of plasmon resonance based structures. The confinement of plasma oscillations within the structure's boundary leads to a charge density accumulation at the boundary. The stored energy, related to the charge density accumulation, is then projected into field enhancement in the close proximity of the resonating metal structure. This is then utilised for a wide range of applications ranging from biochemical sensing to waveguiding [3]. Recent years have also seen an advent of optical manipulation using the field enhancement in the proximity of resonant nanostructures. The basic idea of this approach, described in more detail in Chapter 2, is based on the fact that the objects of higher refractive index than the surrounding medium tend to localise themselves in the highest intensity region of the field. Crucially, the strength of the object confinement within this region depends on how quickly the intensity fades away or, in other words, on the gradient of intensity around the highest intensity region. This is where plasmonic resonators dominate over dielectric based resonators<sup>4</sup> as plasmonic resonators offer much smaller effective mode volumes (see Sec. 1.5) and thus, in general, much steeper gradient of intensity.

---

<sup>3</sup>For the gold nanostructures considered in the thesis the damping is relatively small and this means that the frequency, for which the kinetic energy is maximised, is very close to the frequency for which the potential energy is maximised. This in turn corresponds to a large amplitude of the electron cloud displacement which enhances the field around the nanostructure.

<sup>4</sup>Another advantage of plasmon-based resonators for trapping lies in the broad plasmon resonance lineshape (plasmon resonance line-shapes of nanostructures are usually much broader than the bulk plasma resonance in Fig. 1.2) which ensures that the field enhancement is preserved even when the particle enters the vicinity of the resonator. Dielectric resonators have very narrow lineshape and even a minute change of the surrounding refractive index usually produces significant resonance shift which consequently results in lost of field enhancement.

However, it is important to note that this exceptionally small mode volume comes at a price. The damping or Ohmic losses inside the metal cause non-negligible heating of the metal and this effect is highly detrimental for optical manipulation as it may introduce convection currents and thermophoresis (force acting on the objects due to the presence of the temperature gradient). In fact, we will show, in Chapter 3, that one of the first experimental realisations of optical trapping in the proximity of resonant nanoantenna [4] might have been completely dominated by heating effects in the system. Our investigation (Chapter 3 and Ref. [5]) reveals that the optical forces acting on the dielectric sphere in the proximity of nanoantenna, presented in Ref. [4], were too small to observe stable optical-based trapping. Our research encouraged further development of the plasmon-based trapping and a milestone in this area, spurred by our investigation, was realised by Wang et. al. [6]. Their approach, based on introduction of effective heatsink into the system essentially removes the problem of the heating in plasmon-based optical trapping.

This is currently the only method for mitigating the effects of heating as the two phenomena - the field enhancement and the heating - are closely intertwined (see Fig. 1.2c). This is especially true for weakly damped oscillators where the maximum potential energy, related to field enhancement, and the maximum kinetic energy, closely related to Ohmic losses, appear for essentially the same frequencies (details in Chapter 2). The difference is small enough even for relatively heavily damped gold structures and the two often competing phenomena - localised heating and field enhancement - cannot be easily decoupled. They are always side by side in any plasmon resonant system.

## 1.4 Plasmon resonance of confined plasma

So far we have mainly discussed the **volume** or **bulk plasmons**. For example, the box considered in Section 1.1 was bounded only in the direction of the oscillating plasma but not in directions perpendicular to it. Unfortunately, this type of plasmon cannot be excited by light, because all the electrons in unbounded electron cloud have to be in phase and this cannot be achieved with transverse electromagnetic waves (Fig. 1.4a).

However, the situation changes quickly if we confine the plasma within some very small 3D volume which is the case of metal nanoparticles and metal nanostructures. In such a situation the transversal component of the electric field can be in phase with all the electrons confined within a boundary (Fig. 1.4b) and the coupling of light with electron plasma can exist. This type of resonance is called a **localised plasmon polariton**. The name reflects the intimate coupling of light (polariton) and electron plasma (plasmon). The detailed discussion of this type of resonance based on solution of Maxwell's equations and the optical properties of metals will be given in the next chapter. But before we proceed to a rigorous solution of the problem, it is useful to derive the effects of boundary size and shape on localised plasma from our model of the driven damped oscillator.

Let us consider the following very simplified situation. We displace the electron

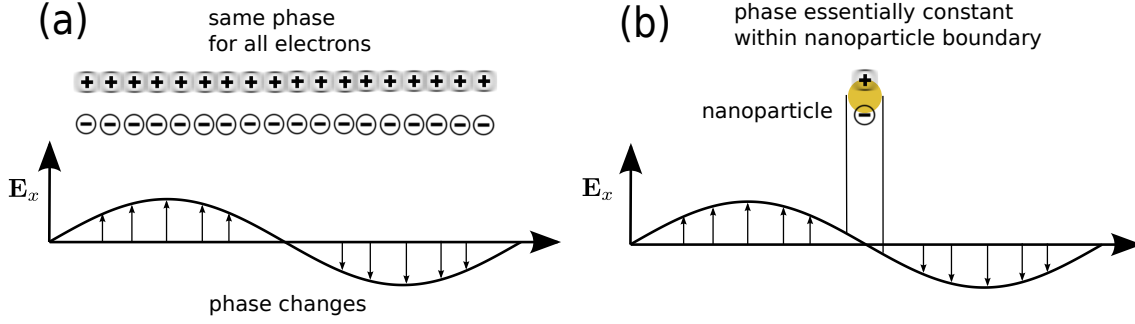


Fig. 1.4: (a) Bulk (or volume) plasmons cannot be excited with transversal electromagnetic waves because all the electrons have to move in phase at resonance condition and the phase of light changes; (b) For strongly confined plasma, the phase within the boundaries of the particles is constant, which allows for light-plasmon coupling.

cloud in a metallic nanoparticle in one direction by  $\Delta x$  (positive ions are assumed fixed). This will lead to a build up of the electric charge  $\pm Q \propto \pm neA\Delta x$ , where  $A\Delta x$  is the volume of the displaced cloud and  $n$  is the electron cloud density. This build up of the electric charge at the respective poles of the sphere is depicted in Fig. 1.5a. The Coulomb potential energy for an averaged distance  $R$  between the charges is then equal to

$$U(\Delta x) = \frac{1}{4\pi\epsilon_0} \frac{(neA)^2}{R} (\Delta x)^2, \quad (1.17)$$

which means that the restoring force is proportional to

$$F(\Delta x) = -\frac{dU(\Delta x)}{d\Delta x} = -\frac{1}{2\pi\epsilon_0} \frac{(neA)^2}{R} \Delta x. \quad (1.18)$$

This means that the positive charge on the opposite side of the particle creates a restoring Coulomb's force acting on the electrons. The average strength of this force affects the natural frequency  $\omega_n$  of such a system. Now, if we increase the diameter of the sphere, the average distance  $R$  between the positive and negative charge will increase. This, in turn, will lead to a smaller average restoring force (Fig. 1.5b).<sup>5</sup> And the smaller average restoring force will finally lead to a decreased natural frequency  $\omega_n$  of the system. The just described red-shift of the plasmon resonance peak with increasing particle size is the core idea behind size-based optical sorting of gold nanoparticles, which forms one of the pillars of this thesis (Chapter 4). The essence of the idea is very simple. Gold nanoparticles of diameters  $d_1 > d_2$  will have different plasmon resonance frequencies  $\omega_1 < \omega_2$ . Incident light of frequency  $\omega_1$  will couple very strongly with particle of size  $d_1$  and relatively weakly with particle of size  $d_2$ .

<sup>5</sup>Of course, in reality, the increased diameter of the sphere also influences the parameter  $A$  but we will neglect this important change at the moment to get the general feeling for the problem. We will come back to it at the beginning of Chapter 4.

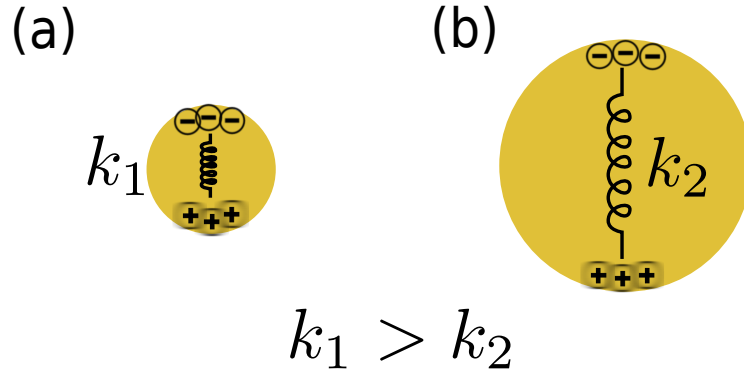


Fig. 1.5: The size of the boundary confining plasma has significant effect on natural frequency  $\omega_n$  of the system. Roughly speaking, the average restoring force due to the Coulomb interaction is stronger in (a) than in (b). This results in red shift of plasmon resonance peak with increasing particle size.

The momentum transfer from light to particle will push both particle types in the direction of light propagation but the magnitude of this push will vary. Similarly, the incident light of frequency  $\omega_2$  will couple more strongly with a particle of size  $d_2$ . If we now illuminate a solution, containing a mixture of gold nanoparticles of diameters  $d_1$  and  $d_2$ , with two counter-propagating beams of different frequencies  $\omega_1$  and  $\omega_2$ , the net result will be size selective movement of gold nanoparticles to opposite directions. The detailed discussion of the conditions necessary for such sorting is given in Chapter 4.

The optical sorting of gold nanoparticles is a novel experimental concept that has never been realised before. To date the optical sorting methods have mainly focused on sorting of dielectric spheres or cells where they proved to be very useful mainly due to exceptional size sensitivity and sterility. However, an efficient method for realising the same idea was missing in the case of metallic objects. This inability to optically differentiate and deliver metallic nanoparticles hindered several applications where the output strongly depends on the precise size of the gold nanoparticles. The research area most affected was the field of biomedical optics with applications of gold nanoparticles ranging from Surface Enhanced Raman Spectroscopy to tumour targeting. We believe that our research, presented in Chapter 4, delivers a generic method that will find many applications in the field of life sciences in the near future.

The red-shift of the plasmon resonance also appears when we elongate the sphere's boundary. The explanation is similar to the one presented above. As we elongate the boundary in the direction parallel to the mode oscillation, the distance between positive and negative charge increases which affects the restoring force and subsequently the natural frequency of the system.<sup>6</sup> This type of red-shift is one of the reasons for the immense popularity of nanoantennas (presented in Chapter 3) as

<sup>6</sup>Furthermore, even the resonance lineshape can be slightly tuned by the presence of the boundary because the additional scattering of electrons at the boundary affects the damping constant  $\Gamma$ .

it allows for a relatively simple tunability of the resonance frequency - making the arms of nanoantenna longer does not usually require any adjustments to fabrication recipe whereas different shapes and scales of the fabricated structures require some minor or even major adjustments.

One of the most colourful and striking manifestations of the boundary size effect can be seen on the stained windows in Notre-Dame de Paris (Fig. 1.6). Here, the

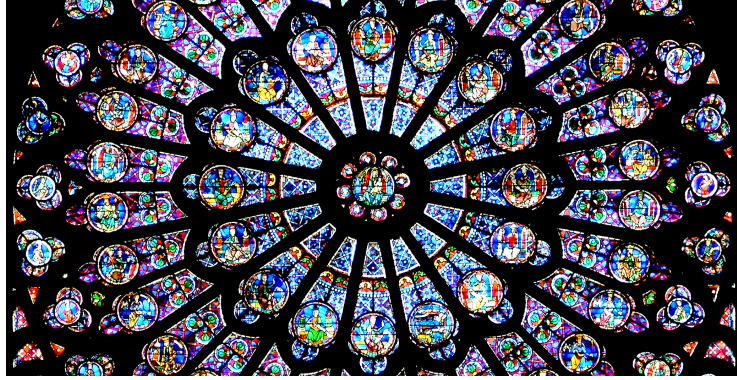


Fig. 1.6: The beautiful spectrum of colours that can be seen through stained glass in Notre-Dame de Paris is a result of boundary effects in confined plasma. (source wiki)

spectrum of colours in stained glass was achieved by adding gold colloids of different sizes into glass. As the daylight passes through the glass, certain wavelengths resonantly couple with electron plasma in nanoparticles and this changes the spectrum of light transmitted through the glass.

We can conclude that the 3D confinement of plasma, through the use of metallic nanoparticles, allows for extreme tunability of plasmon resonance over a wide range of wavelengths, and crucially overlaps with optical and near-infra-red frequencies, where the bulk of the information about our world exists. But what makes metals and semiconductors so special compared to their dielectric counterparts?

## 1.5 Mode volume: metals vs dielectrics

If we go back to Sec. 1.3 we can see what happens if we increase the frequency of the driving field beyond the resonance frequency. In such a case the electrons will be increasingly more and more left behind. In the limit of very high frequencies, the changes of the field become so abrupt, that the electrons basically appear stationary in one optical cycle. They do not even have the time to react to the changes. At this point the metal becomes transparent and behaves like a dielectric. The reason is simple. The electrostatic field from stationary electrons does not alter propagation of electromagnetic waves. For even higher frequencies, even the bound electrons within atoms do not have the time to react to field changes and at that point all dielectrics will have the same dielectric constant. However, at optical frequencies the bound

electrons in atoms still react to the changing field and this reveals the importance of electron dynamics for light propagation. Without this electron motion, all materials would be equivalent to vacuum.

So at very high frequencies there is no difference between metals and dielectrics. The reason is that the conduction electrons no longer play an important role in the physics of the system. Fortunately for our purposes, at optical frequencies, conduction electrons make metals and dielectrics fundamentally different.

We have already mentioned that the plasmonic nanostructures offer unique properties that cannot be reproduced with dielectrics. One of them is the exceptionally strong field enhancement around plasmonic nanostructures and the second is the related strong localised heating in plasmonic nanostructures. The localised heating is easy to understand. We simply have a significant damping of electron movement in the metal which is not present in dielectric. The situation with strong field enhancement is not so straightforward. There are dielectric resonant cavities, for example photonic crystal cavities, with very high field enhancement. However, the crucial difference is in the way the field is enhanced. Dielectric cavities locally enhance intensity by resonantly trapping light, so that it spends more time in a relatively large volume [7]. On the other hand, the mode volume in plasmonic nanostructures is squeezed to a fraction of  $\lambda^3$  ( $0.00033\lambda^3$  in Ref. [8]). The latter is thus of more interest for optical manipulation as we need small mode volumes and the related strong intensity gradients, rather than large intensity, for efficient confinement of very small objects.

But why is the field confinement and related field enhancement more profound in metals than in dielectrics? The difference in response is due to a much stronger interaction of electrons with light in the metallic case. The situation is somehow analogous to the following simplified example. Imagine you have two glasses of whisky. You leave one as it is and you divide the second one into several smaller compartments by inserting some partition walls. If you then drive the systems at their respective resonant frequencies, you notice that the amplitude of whisky in the glass without partitioning is much higher than in the glass of whisky divided into several partitions (Figure. 1.7). If you now substitute whisky for the electron cloud and realise that electrons are surrounded by their field, you recognise why the control and confinement of light in plasmonic nanostructures offers much better results than in the case of dielectrics. We will discuss this problem in much more detail in Chapter 2.

## 1.6 Coupling between two resonant structures

To further demonstrate the power of a model of plasmon resonant system as a damped driven oscillator, let us consider a resonance frequency of a nanoparticle dimer. This situation is quite common as most of the nanoantennas constitute of two nanostructures with a gap in between them.

Instead of a single damped driven oscillator, we now have two coupled damped

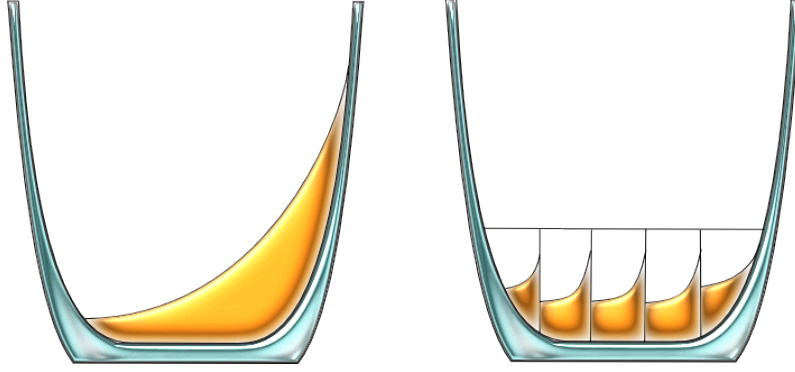


Fig. 1.7: The schematic explanation of the main reason for stronger field enhancement and confinement in case of metal. (left) Metal contains a “sea” of electrons that are not bounded to any atoms and displace fairly well. The electron density can be high at the boundary of glass (structure). (right) In dielectrics, electrons are bound within the atom (depicted as partitioning). They are able to be displaced, but the electron density cannot be changed significantly.

and driven oscillators. The equations of motion for the respective oscillators are

$$\frac{\partial^2 x_1}{\partial t^2} + \Gamma \frac{\partial x_1}{\partial t} + \omega_n^2 x_1 + \frac{\kappa}{m_e} (x_1 - x_2) = \frac{eE_x}{m_e} \cos(\omega t + \Delta) \quad (1.19)$$

$$\frac{\partial^2 x_2}{\partial t^2} + \Gamma \frac{\partial x_2}{\partial t} + \omega_n^2 x_2 + \frac{\kappa}{m_e} (x_2 - x_1) = \frac{eE_x}{m_e} \cos(\omega t + \Delta), \quad (1.20)$$

where  $x_1$  and  $x_2$  are the displacements from equilibrium positions for oscillator 1 and 2 respectively. We also assumed that the natural frequencies  $\omega_n$  are the same for both oscillators. The coupling strength is described with constant  $\kappa$ .

Adding the two equations together leads to

$$\frac{\partial^2 u_b}{\partial t^2} + \Gamma \frac{\partial u_b}{\partial t} + \omega_b^2 u_b = \frac{2eE_x}{m_e} \cos(\omega t + \Delta), \quad (1.21)$$

where we substituted  $x_1 + x_2 = u_b$  and  $\omega_b^2 = \omega_n^2$ . This is just Eq. (1.10) with the same solution (up to a factor 2 in the amplitude of the driving force). We know that the normal mode corresponding to this solution is equivalent to two harmonic oscillators that oscillate in phase (Figure 1.8(left)). Since they are in phase, coupling in between them essentially disappears from equations and the two systems behave as if they were independent. This also explains why the resonance frequency of the coupled system  $\omega_b$  is the same as the natural frequency  $\omega_n$  of the individual systems.

Subtracting the two equations of motion leads to

$$\frac{\partial^2 u_d}{\partial t^2} + \Gamma \frac{\partial u_d}{\partial t} + \omega_d^2 u_d = 0, \quad (1.22)$$

where  $x_1 - x_2 = u_d$  and  $\omega_d^2 = \omega_n^2 + \frac{2\kappa}{m_e}$ . We know that this normal mode corresponds to the harmonic oscillators being out of phase (Figure. 1.8(right)). The overall energy

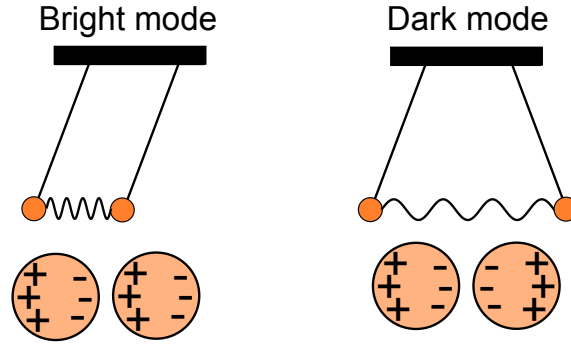


Fig. 1.8: (left) Two oscillators are in phase. The system has a net dipole moment and radiates into far-field. (right) Two oscillators are out of phase. The net dipole moment is equal to zero. System has quadrupole character. The radiated field decays much faster than in the case of a dipole (minimum radiative losses).

of the system is higher due to additional coupling energy introduced by spring  $\kappa$ . This additional energy translates into higher resonant frequency compared to the previous case. There is, however, another very significant change: the driving field completely disappears from the equation of motion. This basically means that the excitation of the mode is very difficult. Furthermore, even if the mode is initially present in the system it disappears very quickly due to damping introduced by  $\Gamma$ . The difficulty in mode excitation exists because the two oscillators are out of phase whereas the driving field is in phase. This means that while one oscillator gains energy from the driving field, the second oscillator, being out of phase with the first one, loses it and vice versa. The net effect of the driving field is thus zero. This mode is called a dark mode because it cannot be detected in normal circumstances (it has zero dipole moment).

Dark modes are very important for the control of resonance lineshape. The potential drawback of plasmon resonances is their broad line-width introduced through large damping<sup>7</sup>. This particularly limits the use of plasmonic structures in sensing applications, simply because the broad line-width decreases the detection sensitivity. Dark modes can be used to tailor the lineshape of the plasmonic structure and decrease the line-width of the resonance by decreasing the damping. This is possible by utilising the quadrupole character of the dark mode which significantly decreases radiative losses. Total damping is then almost solely due to electron scattering in metal and radiative losses can be neglected. The decreased damping makes the resonance much sharper [9]. Furthermore, the decreased losses due to dark modes have potential in metamaterial research where the losses severely limit all applications [9].

Liu et. al. [9] also showed that the dark modes do not only minimise the radiative losses, but also substantially decrease the non-radiative damping in the system by

<sup>7</sup> $\Gamma$  in our model describes only the resistive losses. However, the radiative losses also contribute to damping. Due to the quadrupole character of the dark mode, the radiative losses are significantly decreased, which means that the resonance lineshape might become sharper.

shifting a significant portion of the field outside of the metal into the dielectric medium. This delicate shifting of the balance between metal and dielectric portions of the localised plasmon mode can be, in fact, another answer to the heating problem in optical trapping applications. However, the maximum achievable decrease in heating by introducing the dark modes is probably not large enough to mitigate the negative effects of heating for optical trapping purposes and the excitation of the dark modes is also relatively cumbersome. For these reasons, we believe that the heat-sink method presented by Wang et.al. [6] provides more applicable solution particularly when recognising that the amount of local heating can be reduced by two orders of magnitude by using this method.

## 1.7 Outline of the thesis

In this chapter, we have discussed the fundamental physics of plasmon resonances. We have also briefly pointed out some of the key characteristics associated with plasmon resonances. In particular, the strong field confinement, localised heating and the red shift of the plasmon resonance that appears with increasing particle size have been discussed.

The first two prominent features of plasmon resonances, the strong field confinement and localised heating, play a key role in one of the most rapidly developing fields of optical manipulation - optical trapping using plasmonic nanostructures. This research field utilises the fact that the strong field confinement translates into very strong object confinement. This happens since, typically, objects of higher refractive index than the surrounding medium tend to localise themselves in the highest intensity region of the field. Furthermore, such trapping can be realised using very low powers, which is usually presented as a bio-friendly property. Unfortunately, the strong field confinement is also inevitably intertwined with the localised heating. As a consequence, some disruptive effects on the trapping process - like convective currents - can appear. Also, the additional heating in plasmonic structures can be, in fact, very strong even for extremely low powers used for trapping. The research papers, at the start of my PhD, basically overlooked the effects of heating. For this reason, we have decided to explore in detail the interplay between the optical forces induced by field confinement and the related heating near the popular plasmonic trapping structure - nanoantenna. The results of this research will be presented in Chapter 3.

The last mentioned prominent feature of the plasmon resonances, the red-shift of the resonance peak for increasing size of the particle, sparked an idea that such a phenomenon might be useful to optically differentiate between particles of different sizes. We further thought that such a method could potentially outperform existing sorting methods, such as sedimentation and centrifugation, that differentiate particle size based purely on the physical size of the particle. The outcome of such method has to be relatively poor in situations when two particles of very similar sizes needs to be differentiated. The problem is somehow analogous to the following situation. Imagine you have two spheres with almost identical diameter.

Under normal circumstances, it is not easy to tell which one is bigger and which one is smaller. They both look almost the same. But is there a way to simplify the differentiation of the spheres? Fortunately, there is. The thing with light is that the particles can actually appear much bigger or smaller than they really are when illuminated with light of a certain wavelength (Fig. 1.9). The "shadow" of

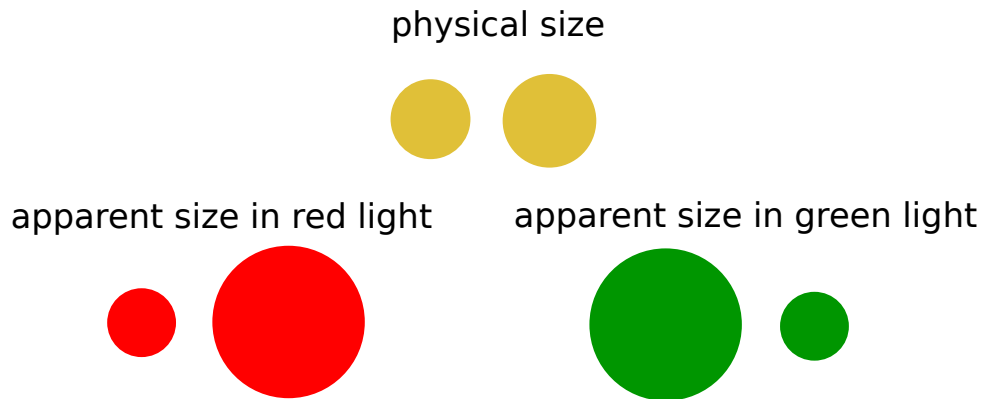


Fig. 1.9: The differentiation of two particles of very similar physical size is difficult. However, the apparent size of the same particles when illuminated by light of certain wavelengths can be very different. We have used this simple phenomenon for optical sorting of gold nanoparticles which is presented in Chapter 4.

the particles can be much larger (or smaller) than their actual geometrical cross-section for certain wavelengths. Very roughly speaking, even the light that does not directly hit the particle can be still diffracted by it and vice versa, even the light going through the particle can be undiffracted. Using this trick, we can "inflate" or "shrink" the apparent size of the particles so that the size difference appears bigger than the actual difference in physical size. This is the main advantage of the novel all-optical sorting method of gold nanoparticles presented in Chapter 4 - the advantage over conventional methods is hidden in this trick. Basically, even if the physical size of the particles is barely different, the apparent particles sizes, for resonant wavelengths, can appear miles apart.

Another advantage of the all-optical plasmonic sorting is the ability to sort particles in small volumes and in situ. This may be useful for biological applications in which a particle of given properties has to be delivered close to a targeted specimen. The modifications of the method developed in Chapter 4, resolving the issues of particle diffusion, hold promise for the realisation of plasmonic conveyor belt, based on the tilted washboard potential similar to Ref. [10] that realises this idea for dielectric particles. The conveyor belt would enable much better control of plasmonic nanoparticles over an extended region of space with the combined capability to deliver and identify the type of the gold nanoparticle. This would improve the reliability of the output of the repeated measurements on the biological specimens. We would also like to note that the all-optical plasmonic sorting is capable of addressing single particle whereas the other non-optical methods, like sedimentation,

lack this single particle specificity. This is a crucial difference which makes the optical sorting much more modular for precise biological experiments.

We finally conclude the thesis with Chapter 5 that theoretically explores the possibility to make the apparent difference in size of the particles even larger. The developed theoretical framework is able to find the optimal beam shape that maximises the apparent size difference between particles. We also briefly discuss the choice of the optimal wavelengths with respect to minimal heating during the sorting process.

We will start our discussion in Chapter 2 where we will introduce the two essential pillars of the thesis - the strong field confinement due to plasmon resonance and related heating - from a more rigorous point of view. The rigorous treatment of the last pillar of the thesis - the red-shift of the plasmon resonance peak with particle size - is presented in Chapter 4. Please bear in mind that although some of the following chapters contain significant amount of details necessary to understand the behaviour of the systems concerned, the basic physics, in all the following chapters, is always the same and very simple - the physics of damped driven oscillator. After all, the beauty of physics is in its ability to harbour seemingly unconnected phenomena under one single roof. With all that said, enjoy the story of resonances that follows.

## Chapter 2

# The enhancement of optical forces using plasmon resonances

Many technological advances in recent years require the manipulation and control of matter with incredible precision and at ever smaller size/distance scales [11,12]. The main technological problem is to manipulate objects that are only a few nanometers in size. The conventional mechanical tools do not seem to be appropriate or even practical if the object's size becomes smaller than a millimetre. Fortunately, there is an unexpected solution to the problem.

As early as in 17th century astronomers observed that the tails of comets always point away from the Sun. Soon afterwards, Johannes Kepler suggested that the observed effect might be caused by radiation pressure exerted by light. This pressure indeed exists and although the pressure does not seem to be very strong in everyday life, it is, in fact, strong enough to oppose tremendous gravitational force in some of the hottest stars. Without the radiation pressure, some stars would simply collapse. The radiation pressure effect of light is also significant at very small scales, where the momentum carried by photons is sufficient to observe noticeable mechanical effects. These mechanical effects, in turn, can be used for efficient optical manipulation of very small objects.

But in order to completely control the mechanical effects of light one needs to be able to control the light itself. Unfortunately light seems to be quite evasive. However, it is in human nature to tame uncontrollable and wild things around us. All the major technological leaps in human history overlap with the time when we tamed unimaginable - e.g. fire, fossil fuels, nuclear power. A similar breakthrough is happening right at this moment - we are in a process of taming the light for delicate manipulation of objects. The first attempts to control the light were based on simple optical elements like lenses and mirrors. The capabilities of these optical elements to control light were more than acceptable throughout the history, however, the accuracy to which the light can be controlled using these far-field optical elements is limited. This limit is very small. Nevertheless, the limit now became a major problem for optical manipulation research - particularly for optical trapping of nanoscale objects.

The field of optical trapping evolved abruptly over the recent years and it became one of the major candidates for revealing the secrets of the molecular dynamic in the cells. It is this cutting-edge optical trapping, reaching into single-molecule levels, that suffers most from the limit of far-field optical elements to control light at the nanoscale.

This chapter starts with the discussion of optical forces acting on objects in electromagnetic fields. We then present the major drawbacks of the far-field trapping at a very small scale and present a possible solution that utilises the enhanced interaction of light with structures supporting the plasmon resonance. This forms a theoretical basis for the optical trapping of dielectric spheres near nanoantenna presented in Chapter 3.

## 2.1 Optical forces

We start our discussion with the study of optical forces acting on very small spheres. "Small", in this particular case, is defined by the condition that the radius of the sphere  $r$  has to be much smaller than the wavelength of light  $\lambda$ .

Let us insert this small sphere into a beam of photons. The photons will be scattered and absorbed by the sphere and, as a result, the momentum of photons will change. Consequently, to conserve the momentum of the whole system composed of sphere and photons, the momentum of the sphere also has to change. Using Newton's second law we have<sup>1</sup>

$$F_{\text{push}} = \frac{\Delta p}{\Delta t}. \quad (2.1)$$

The momentum of a photon  $p$  and its energy  $E$  in a medium with refractive index  $n_2$  (no dispersion) are related by (Minkowski version)

$$p = \frac{n_2}{c} E, \quad (2.2)$$

which allows us to write the 'push' force in the form

$$F_{\text{push}} = \frac{n_2}{c} \left( \frac{\Delta E_{\text{scattered}}}{\Delta t} + \frac{\Delta E_{\text{absorbed}}}{\Delta t} \right). \quad (2.3)$$

The scattered ( $\Delta E_{\text{scattered}}/\Delta t$ ) and absorbed ( $\Delta E_{\text{absorbed}}/\Delta t$ ) powers are proportional to the incoming intensity  $I$  and to the scattering  $C_{\text{sca}}$  and absorption  $C_{\text{abs}}$  cross-sections of the spherical particle. This means that the 'push' force can be written as

$$F_{\text{push}} = \frac{n_2 I}{c} (C_{\text{sca}} + C_{\text{abs}}). \quad (2.4)$$

For the special case of the dielectric sphere,  $C_{\text{abs}}$  is usually very close to zero and the 'push' force reduces to the **scattering force**

$$F_{\text{sca}} = \frac{n_2 I}{c} C_{\text{sca}}. \quad (2.5)$$

---

<sup>1</sup>Assuming that the net momentum change is in one direction only.

After inserting the value of the scattering cross-section for the case of small spherical particles from Ref. [13], we finally get

$$F_{\text{sca}} = \frac{n_2 I}{c} \frac{128\pi^5 r^6}{3\lambda^4} \left( \frac{m^2 - 1}{m^2 - 2} \right)^2, \quad (2.6)$$

where  $m = n_1/n_2$ , with  $n_1$  denoting the refractive index of the sphere. Please note that the scattering cross-section  $C_{\text{sca}}$ , and thus also the scattering force, is proportional to  $r^6$ . This is a very important result for our further discussion.

The scattering force  $F_{\text{sca}}$  is not the only light induced force that acts on a small sphere. There is one additional force. For a very small dielectric sphere, the condition  $r \ll \lambda$  ensures that the phase of the light is constant within the volume of the sphere. This phase-constant external field induces positive and negative charges on the opposite poles of the sphere. This induces a polarisation of the sphere equal to

$$\mathbf{p} = \varepsilon_0 \varepsilon_2 \alpha \mathbf{E}, \quad (2.7)$$

where  $\alpha$  is the polarizability of the sphere which will be derived in Sec. 2.4.2 and  $\varepsilon_2 = (n_2)^2$ . Using the Lorentz force equation on the respective induced charges results in the following force acting on the sphere<sup>2</sup>

$$\mathbf{F}_{\text{grad}} = \frac{1}{4} \varepsilon_0 \varepsilon_2 \alpha \nabla I(\mathbf{r}) \quad (2.8)$$

Inserting the value for polarizability  $\alpha$  derived in Sec. 2.4.2 finally gives<sup>3</sup>

$$\mathbf{F}_{\text{grad}} = \pi r^3 \varepsilon_0 \varepsilon_2 \frac{\varepsilon_1 - \varepsilon_2}{\varepsilon_1 + 2\varepsilon_2} \nabla I(\mathbf{r}). \quad (2.9)$$

This force is called the **gradient force** as it depends on the gradient of intensity of the applied field. For the typical case of particle with larger refractive index than the surrounding medium ( $\varepsilon_1 > \varepsilon_2$ ), the force is directed towards highest intensity regions of the field and this can be readily applied to 3D trapping of objects.

The decomposition of the optical forces into scattering and gradient components immediately reveals the three potential applications for enhancement of the optical forces through utilisation of plasmon resonance:

1. **Enhanced trapping of metallic spheres** - The denominator of Eq. (2.9) suggests that the gradient forces might be significantly enhanced when the denominator  $|\varepsilon_1 + 2\varepsilon_2|$  is minimised. This indeed happens at certain frequencies for metallic spheres. Unfortunately, the absorption is also enhanced which partially cancels out the effects of enhanced gradient forces. Furthermore, the polarizability also changes a sign around resonance condition, which might actually reverse the sign of the gradient force. This behaviour was used to confine objects in the lowest intensity region of the beam [15].

---

<sup>2</sup>The Lorentz force equation applied to a dipole actually also provides the term corresponding to  $F_{\text{sca}}$ . The complete derivation can be found in Ref. [14]. We also note that both the  $F_{\text{sca}}$  and  $\mathbf{F}_{\text{grad}}$  are averaged over one optical cycle.

<sup>3</sup>In the case of metallic nanoparticles  $\Re(\alpha)$  instead of  $\alpha$  has to be used in Eq. (2.8).

2. **Enhanced trapping of nano-objects in the close proximity of plasmon resonant structure** - For small dielectric (non-absorbing) nanoparticles the gradient force scales with volume of the particles  $\mathbf{F}_{\text{grad}} \propto r^3$  whereas the scattering force scales with the volume of the particle squared  $\mathbf{F}_{\text{sca}} \propto r^6$ . As a result, we can neglect the scattering force when considering trapping of small dielectric objects and the optical trapping is then completely governed by the gradient forces in the system. Furthermore, we can see that the gradient force can be enhanced by increasing the gradient of intensity  $\nabla I(\mathbf{r})$ . We have seen in Sec. 1.5 that the plasmon resonant structures exhibit extremely small mode volumes that are orders of magnitude smaller than the mode volumes of dielectric resonators.<sup>4</sup> It thus seems only natural to use structures supporting plasmon resonances for confinement of very small particles. Unfortunately, as already mentioned before, the extremely strong field confinement comes at a price of heating.
3. **Enhancement of 'push' force acting on nanoparticles for optical sorting applications** - We will see later in this chapter that both scattering and absorption cross-sections are enhanced for the plasmon resonance condition. This means that resonant nanoparticles are 'pushed' more strongly than the non-resonant ones and this can be used for size-based optical sorting of nanoparticles.

This thesis contains the discussion of latter two applications of the plasmon resonances as the first application was already investigated in detail by [15]. Let us start with a background for the second application in the above list.

## 2.2 Optical trapping of small objects

We have seen that the gradient force plays a key role in the optical trapping of small spheres. But what tools do we have to create steep gradients of intensity and why are people interested in strong field confinement around plasmon resonant structures? After all, the three-dimensional confinement of objects can be easily realised in the focus of the Gaussian beam which has the intensity profile given by [16]

$$I(R, z) = I_0 \left( \frac{w_0}{w(z)} \right)^2 \exp \left( -\frac{2R^2}{w(z)^2} \right), \quad w(z) = w_0 \sqrt{1 + \left( \frac{z\lambda}{\pi w_0^2} \right)^2}, \quad (2.10)$$

where  $w_0$  is the beam waist and  $I_0 = I(0, 0)$ . The Gaussian beam profile in xy and yz-plane (Fig. 2.1) shows an intensity "hotspot" confined in all three dimensions. This means that the trapping of very small objects should be, at least in principle, possible using simple Gaussian beam configuration. In reality, the situation is slightly more complicated.

---

<sup>4</sup>There is of course a subtle difference between maximum gradient of intensity and the level of field confinement, but the two phenomena are usually strongly correlated and this allows us to refer directly to field confinement in the following discussions.

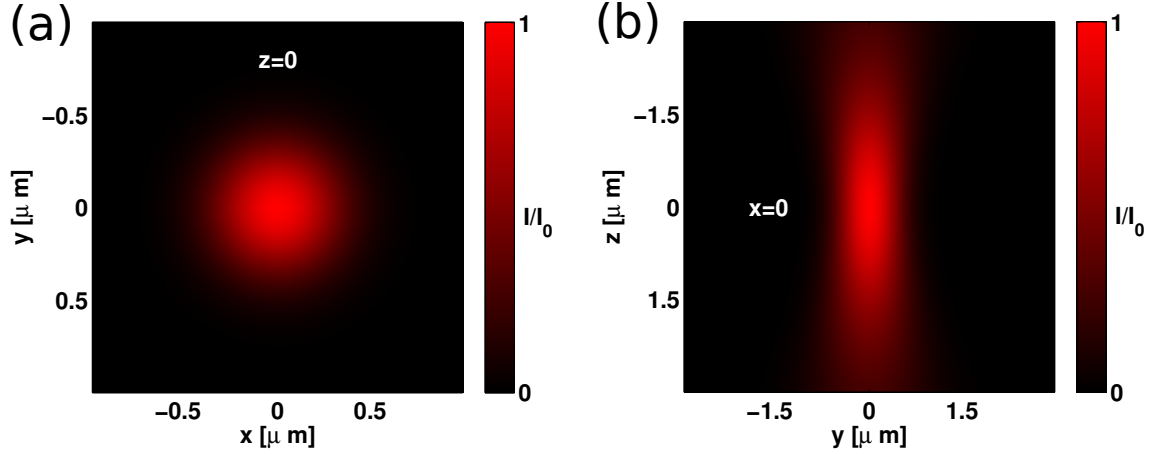


Fig. 2.1: The intensity profile of the Gaussian beam in the (a)  $xy$  and (b)  $yz$  -plane calculated for parameters of  $\lambda = 633$  nm,  $w_0 = 500$  nm and  $I_0 = 1$  (the intensity scale is normalised with respect to this number).

The major problem of the Gaussian beam based optical trapping can be understood from a simple dimensional analysis of the trapping situation.

There are two competing phenomena in optical trapping of small particles. We have just seen that the gradient force can be used to trap the particle in the focal spot of the Gaussian beam. The gradient force is thus the constructive effect in optical trapping. However, there is, another, destructive effect that cannot be neglected at the nanoscale - the inevitable thermal motion of the particle. This thermal motion introduces random "kicks" to the movement of the particle and this sometimes leads to the particle leaving the trap. Both processes can be described by their respective characteristic times - trap formation time  $\tau_f$  and trap decay time  $\tau_d$ . Let us also introduce a characteristic size of the trap  $l$ . This number will define the boundaries of the trap within which the particle can move.

The trap formation, caused by the  $\mathbf{F}_{\text{grad}}$ , can be averaged over the characteristic length  $l$  of the trap to get an order of magnitude estimate for the average gradient force within the trap - denoted by  $\bar{F}_{\text{grad}}$ . Since the spherical particle moves in a medium of viscosity  $\eta$ , we can estimate the average speed with which the particle falls into trap from the Stoke's drag equation

$$v \propto \frac{\bar{F}_{\text{grad}}}{6\pi\eta r}. \quad (2.11)$$

Consequently, the time needed to get the particle from the edge to the centre of the trap (the trap formation time) is roughly proportional to

$$\tau_f \propto \frac{6\pi\eta r l}{\bar{F}_{\text{grad}}}. \quad (2.12)$$

We can decompose the contribution to the average gradient force  $\bar{F}_{\text{grad}}$  inside the trap into three components. The first component is the average gradient of the

intensity in the trap described by a factor  $G$ . The second component is the peak intensity of the trap  $I_0$  and the last component is related to the size of the particle being confined in the trap. This means that we can write the gradient force as

$$\bar{F}_{\text{grad}} \propto \varepsilon_0 G I_0 r^3, \quad (2.13)$$

where  $G = \frac{1}{I_0} \overline{\nabla I(\mathbf{r})}$  with  $\overline{\nabla I(\mathbf{r})}$  denoting the average intensity gradient in the trap. Using this relation, we can finally express the trap formation time  $\tau_f$  given by Eq. (2.12) as

$$\tau_f \propto \frac{6\pi\eta l}{\varepsilon_0 G I_0 r^2}. \quad (2.14)$$

On the other hand, the trap decay time  $\tau_d$  is governed by the diffusion of the particle out of the trap. The diffusion coefficient for spherical particles is given by [17]

$$D = \frac{k_B T}{6\pi\eta r}, \quad (2.15)$$

where  $k_B$  is the Boltzmann constant and  $T$  is the temperature. Using the diffusion coefficient we can estimate the time for the particle to diffuse from the centre to the edge of the trap as

$$l^2 \propto D \tau_d \rightarrow \tau_d \propto \frac{6\pi\eta r l^2}{k_B T}. \quad (2.16)$$

If we require a stable trap then the trap formation time  $\tau_f$  should be much shorter than the trap decay time  $\tau_d$ , which means that the condition for stable trapping can be expressed as

$$\frac{\tau_f}{\tau_d} \propto \frac{k_B T}{\varepsilon_0 G I_0 r^3 l} \ll 1. \quad (2.17)$$

Investigation of this equation reveals the main complication that precludes simple trapping of very small particles - the above condition is very difficult to satisfy for small  $r$ . The situation becomes even more complicated when we notice that the characteristic length of the trap  $l$  appears in the denominator. This essentially means that the situation for trapping the nanoparticles is even worse than it seems to be, because in an ideal case, we would like to confine the nanoparticle in a trap of a characteristic length of the same order as the particle size. The condition for stable trapping in such a case reduces to

$$\frac{k_B T}{\varepsilon_0 G I_0 r^4} \ll 1.^5 \quad (2.18)$$

This equation leaves only two options for achieving stable trapping of extremely small particles. The first and the simplest solution is to increase the power of the laser  $I_0$ . This is, in fact, a common solution. Unfortunately, the intensity cannot be increased arbitrarily high since the absorbed heat in the nanoparticle, even for the

---

<sup>5</sup>For the typical optical trapping values of  $I_0 = 10^{12} \text{ Wm}^{-2}$ ,  $G = 10^6 \text{ m}^{-1}$ ,  $k_B T = 10^{-21} \text{ J}$  and for the particle size of  $r = 10^{-7} \text{ m}$ , the ratio is  $\approx 1$  which confirms the difficulty of the optical trapping at this scale.

dielectric case, eventually reaches a damage threshold of the nanoparticle. Due to this reason, the smallest particles ever trapped, in the Gaussian beam configuration, are of the order of 10 nm in diameter [18].

The second option is to increase the factor  $G$ . The increase of factor  $G$  is basically equivalent to steeper transition from the low to the high intensity regions of the field. But in order to achieve this steep transition we would have to be able to squeeze the light to very small volumes. As a matter of fact, for stable optical trapping of very small particles at modest optical powers, this volume would have to be so small that even the most powerful far-field optical elements fail to produce it. And the reason why the far-field optical elements fail to produce it is not in our inability to manufacture these elements with acceptable precision. The minimum achievable volume of the focus can be understood by using the fundamental law of nature - the Heisenberg uncertainty principle (alternative derivation can be found using the Fourier formalism). Intriguingly, the near-field optical elements can play tricks with this fundamental principle of nature and for structures supporting plasmon resonances the ingenuity and resourcefulness of these tricks reaches its peak which allows for extremely small volume of the focus. <sup>6</sup>

## 2.3 Plasmon resonances and the Heisenberg uncertainty principle

The smallest volume to which the light can be squeezed by far-field optical elements is given by the Heisenberg uncertainty principle which prohibits simultaneous measurement of certain pairs of physical quantities with absolute accuracy. Position and momentum is an example of such a pair of physical quantities. The law states that if we do a repeated measurement of position and momentum on an ensemble of systems then the product of standard deviations of measured position and momentum has to satisfy the following inequality

$$\sigma_x \cdot \sigma_{p_x} \geq \frac{\hbar}{2}, \quad \sigma_y \cdot \sigma_{p_y} \geq \frac{\hbar}{2}, \quad \sigma_z \cdot \sigma_{p_z} \geq \frac{\hbar}{2}. \quad (2.19)$$

Using the relation between momentum and wavevector of a photon,  $\mathbf{p} = \hbar\mathbf{k}$ , we can re-write the above equations to

$$\sigma_x \cdot \sigma_{k_x} \geq \frac{1}{2}, \quad \sigma_y \cdot \sigma_{k_y} \geq \frac{1}{2}, \quad \sigma_z \cdot \sigma_{k_z} \geq \frac{1}{2}. \quad (2.20)$$

Now let us consider the following situation. We create an ensemble of photons in which all the photons have momentum only in the z-direction,  $\mathbf{k}_0 = (0, 0, k_0)$ , where

$$k_0 = \frac{2\pi}{\lambda_0} = \sqrt{k_x^2 + k_y^2 + k_z^2}. \quad (2.21)$$

---

<sup>6</sup>We note that the near-field optical elements do not violate Heisenberg's uncertainty principle. The near-field optical elements only allow for more intriguing momentum distributions compared to the far-field elements. This in turn allows to achieve more interesting position distributions that possess better field confinement.

For such an ensemble the values of wavevector components are fixed ( $k_x = 0$ ,  $k_y = 0$ ,  $k_z = k_0$ ) and this means that the respective standard deviations in momentum are all equal to zero

$$\sigma_{k_x} = 0, \quad \sigma_{k_y} = 0, \quad \sigma_{k_z} = 0. \quad (2.22)$$

This further means that, in order to satisfy Eq. (2.20), the standard deviations in position  $\sigma_x, \sigma_y$  and  $\sigma_z$  need to be infinite in all three directions. This result should not be surprising, because the above situation, in which all the photons have momentum in one direction, is equivalent to a plane-wave and the plane-wave has infinite extend.

Let us now place a lens into the path of this ensemble (Fig. 2.2). We assume that

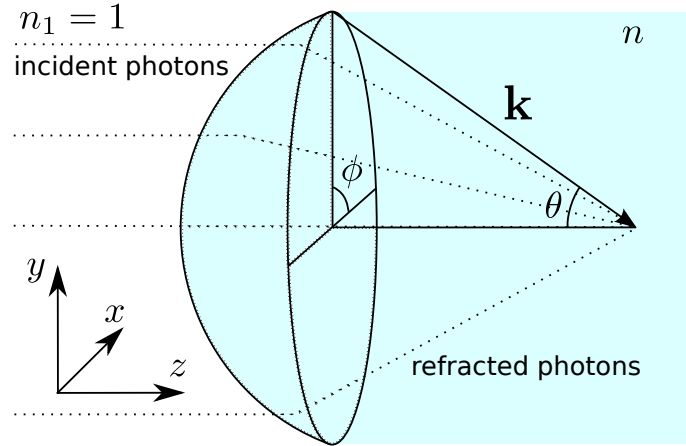


Fig. 2.2: The momentum distribution of incident ensemble of photons is changed by the lens.

the photons are incident from the vacuum ( $n_1 = 1$ ). We further assume that the material to the right of the spherical surface of the lens has refractive index  $n$ . The lens will introduce a specific transformation to each and single  $\mathbf{k}_0$  in the ensemble. If we assume zero reflection on the surface of the lens then all photons are refracted and the resulting wavevectors of refracted photons are given by

$$k_x = -k \sin \theta \cos \phi, \quad k_y = -k \sin \theta \sin \phi, \quad k_z = k \cos \theta, \quad (2.23)$$

where  $k = 2\pi n/\lambda_0$  and  $\theta, \phi$  describe angular position of incident photons on a sphere representing the lens. The lens thus modifies the distribution of  $k_x, k_y$  and  $k_z$  in the ensemble of photons and as a consequence also modifies the corresponding standard deviations  $\sigma_x, \sigma_y$  and  $\sigma_z$ .

Monte Carlo simulations of  $N = 10^6$  photons incident on the lens with maximum half-angle of  $\theta_{max} = 40^\circ$  give distributions of  $k_x, k_y$  and  $k_z$  shown on Fig. 2.3a. The standard deviations in momenta,  $\sigma_{k_x} \approx 0.32 k$ ,  $\sigma_{k_y} \approx 0.32 k$  and  $\sigma_{k_z} \approx 0.07 k$ , calculated from these distributions can be inserted back into Eq. (2.20) to get the following standard deviations in position

$$\sigma_x \geq \frac{1}{0.32} \frac{\lambda_0}{4\pi n}, \quad \sigma_y \geq \frac{1}{0.32} \frac{\lambda_0}{4\pi n}, \quad \sigma_z \geq \frac{1}{0.07} \frac{\lambda_0}{4\pi n}. \quad (2.24)$$

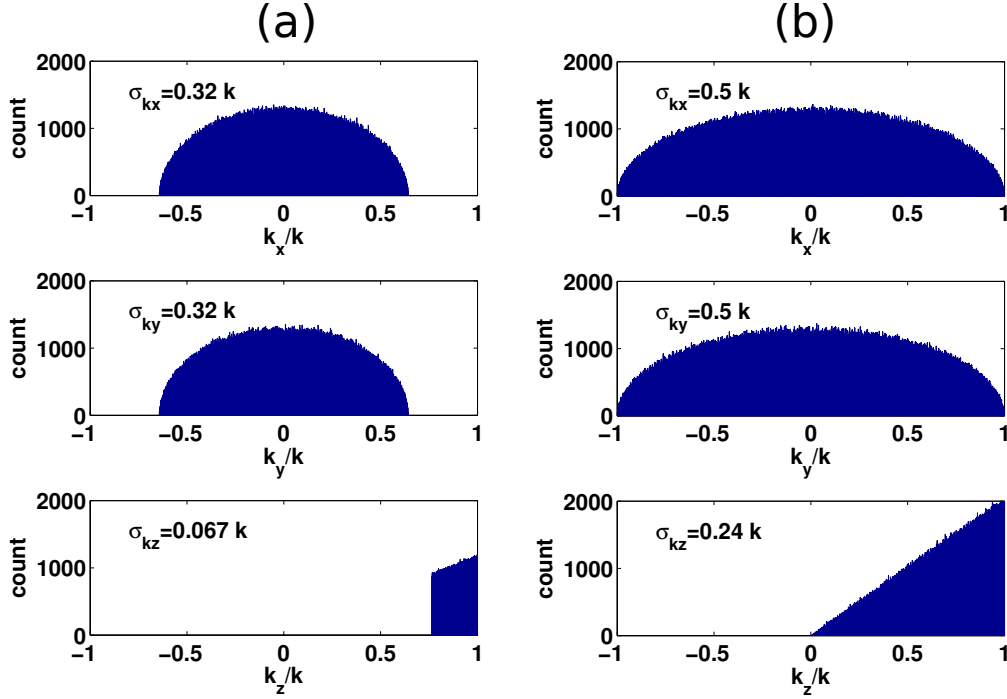


Fig. 2.3: The distribution of momentum in the ensemble of photons transformed by a lens with half-angle (a)  $\theta_{max} = 40^\circ$  and (b)  $\theta_{max} = 90^\circ$ .

The ensemble of photons transformed by the lens has several characteristics. For example, we can see that the better confinement in position can be achieved for photons with shorter wavelength  $\lambda_0$  and for high refractive index  $n$  (equivalent to shorter wavelength). We can also see that the confinement in  $z$ -direction is lower than in  $x$  and  $y$ . This is a well known result for a lens system. The reason for this discrepancy stems from the asymmetry of transformation introduced by the lens (see Fig. 2.3a,b). The lens simply cannot spread the momenta of photons in  $z$  as much as in  $x$  and  $y$ . Furthermore, if we increase the half-angle to  $\theta_{max} = 90^\circ$ , the width of momentum distribution will increase (Fig. 2.3b). This means that a lens with larger half-angle can achieve better confinement of light in all three directions.

However, even the lens with maximum achievable half-angle  $\theta_{max} = 90^\circ$  creates a momentum distribution with a finite standard deviation. The limit exists in any far-field scenario because the transformed momentum value always falls within  $\langle 0, k \rangle$  range. As a consequence, the position distribution of the photon ensemble cannot be made arbitrarily small using far-field optical elements.

Fortunately, there is way to increase the width of momentum distribution - introduce imaginary  $k_x$ ,  $k_y$  or  $k_z$ . For example if we choose  $k_z = ia$  and use Eq. (2.21), we get

$$k_0 = \sqrt{k_x^2 + k_y^2 - a^2}. \quad (2.25)$$

Now, the larger the factor  $a$  the bigger the wavevectors  $k_x$  and  $k_y$  can be. There is

no theoretical limit. Crucially, both  $k_x$  and  $k_y$  can be larger than  $k_0$ , which means that we can, at least in principle, have infinitely wide distributions of  $\sigma_{k_x}$  and  $\sigma_{k_y}$ . The situation with imaginary momentum  $k_z$  corresponds to a solution of Maxwell's equations called evanescent wave. The intensity of such a wave fades away in the  $z$ -direction. For this reason, the far-field optical elements cannot access these waves and this, in turn, limits their ability to confine light. On the other hand, near-field optical elements can readily access these waves and this gives them the ability to confine light to much smaller volumes.

The realisation that near-field optical elements can go beyond diffraction limit sparked an avalanche of new interest in near-field optics. And soon afterwards, people realised that noble metals are an exceptionally good choice of material when it comes to near-field optics as they enable to achieve very large decay factor  $a$ . The reason for this lies in the unique interaction of metal with light - the plasmon polariton. This unique coupled state of light and oscillating plasma opens up the possibilities for light-control, sculpting and shaping with incredible accuracy and elegance. Using the unique properties of plasmon polaritons, we can confine, concentrate and direct light and its energy with incredible accuracy.<sup>7</sup> In its essence, plasmon polariton offered a new toolbox for shaping the light. And since light is such a valuable source of information about our world, having a finer control over it, simply means that we can access information that was so far hidden. On the other hand, we would like to stress again that the extreme light confinement in the near-field of plasmon resonators comes at the cost of heating and losses, which complicates all their potential applications. Let us now have a closer look at some of the basic physics of plasmon polaritons. This will help us to understand the origin of the very strong field confinement in the proximity of plasmon resonators and its connection to the optical trapping applications.

## 2.4 Fundamental physics of plasmon polaritons

In order to quantify and fully understand the interaction of light with various metallic structures, we need to abandon the qualitative model of driven damped oscillator developed in the previous chapter. Even though the model is extremely viable for qualitative studies, it does not allow to include small nuances of light-metal interaction in a simple way. The major problem is the determination of the key parameters of the system - like the natural frequency  $\omega_n$  of the damped driven oscillator. For example, we have seen in Sec. 1.4, that the shape and size of the region where the electron cloud is bounded influences the natural frequency  $\omega_n$  of such a system. But how can we find the exact frequency  $\omega_n$  of this natural mode? Calculating the natural frequency by displacing the charge density in a spherical particle and obtaining the subsequent movement of this charge using Newton's and Coulomb's law is not very practical. Furthermore, the calculation of the damping term  $\Gamma$  that

---

<sup>7</sup>The accuracy of this field focusing property is limited by the geometry supporting the plasmon. The number of atoms in this structure needs to be sufficiently large such that the "sea of electrons" still exists. Only then can the plasmon exist and only then is the field enhanced by the plasmon effect.

accounts for all the solid state effects and the presence of the boundary adds even more complexity to this task.

Fortunately, the interaction of light with matter can be readily described by Maxwell's equations (no external sources) [3]

$$\nabla \times \mathbf{E}(\mathbf{r}, t) = -\frac{\partial \mathbf{B}(\mathbf{r}, t)}{\partial t}, \quad (2.26)$$

$$\nabla \times \mathbf{H}(\mathbf{r}, t) = \frac{\partial \mathbf{D}(\mathbf{r}, t)}{\partial t}, \quad (2.27)$$

$$\nabla \cdot \mathbf{D}(\mathbf{r}, t) = 0, \quad (2.28)$$

$$\nabla \cdot \mathbf{B}(\mathbf{r}, t) = 0. \quad (2.29)$$

and by the related constitutive relations

$$\mathbf{D} = \varepsilon_0 \varepsilon \mathbf{E}, \quad (2.30)$$

$$\mathbf{B} = \mu_0 \mu \mathbf{H}, \quad (2.31)$$

that describe the behaviour of matter under the influence of an electromagnetic field. Since we will only deal with non-magnetic materials, we can simply assume  $\mu = 1$ . This leaves us with a single complex function  $\varepsilon$  describing the response of matter under the influence of electromagnetic fields. This number is called the permittivity. It can be measured by ellipsometry for bulk materials, but the bulk value of permittivity is usually valid even for very small nanoparticles. As such, the value of permittivity is a very useful number. Crucially, this number contains the physics of all processes that take place on the microscopic scale in a material. For example, the electron scattering on the crystal lattice, interband transitions and even the relativistic corrections of electron wave-functions for materials with heavy atoms. Consequently, being equipped with Maxwell's equations and the value of permittivity, we can easily study the light-metal interaction for any linear problem.

In particular, there are two solutions (modes) of Maxwell's equations that are of interest for metal based near-field optics. The first solution is called the **surface plasmon polariton** (SPP). It denotes a mode confined at the metal-dielectric interface and propagating along it. The second type of plasmon mode is called the **localised surface plasmon polariton** (LSPP). As opposed to SPP, this mode is a non-travelling mode. It is confined on the surface of metallic nanoparticles.

Both of these modes became an essential tool in a wide range of applications such as biomolecular sensing [19–21], highly localised heating [22, 23], wave-guiding [24–27], in transformational optics using metamaterials [28, 29] and for optical switching [30]. The modes are also widely utilised for the enhancement of fluorescence [31] and the Raman signals [32, 33]. And, as we already know, these modes also found their way to optical manipulation research [4, 6, 34–45]. To understand the reason for such a success, it is useful to explore the properties of these modes by solving Maxwell's equations. Let us begin with the SPP mode.

### 2.4.1 SPP mode

Starting from Maxwell's equations we can derive the following dispersion relations for the SPP mode (see full derivation in Appendix A)

$$k_x = \sqrt{\frac{\varepsilon_1 \varepsilon_2}{\varepsilon_1 + \varepsilon_2}} \frac{\omega}{c}, \quad (2.32)$$

$$k_{j,z} = -\sqrt{\frac{\varepsilon_j^2}{\varepsilon_1 + \varepsilon_2}} \frac{\omega}{c}, \quad (2.33)$$

where  $k_x$  denotes the wavevector of the mode along the metal-dielectric interface and the  $k_{j,z}$  denotes the wavevector of the mode perpendicular to the interface ( $z$ -direction) in respective dielectric ( $j = 2$ ) and metal ( $j = 1$ ) half-spaces.

The dispersion relation of this mode (for  $k_x$ -wavevector), for the specific case of gold-glass interface, is plotted on Fig. 2.4a. We can see that the real part of

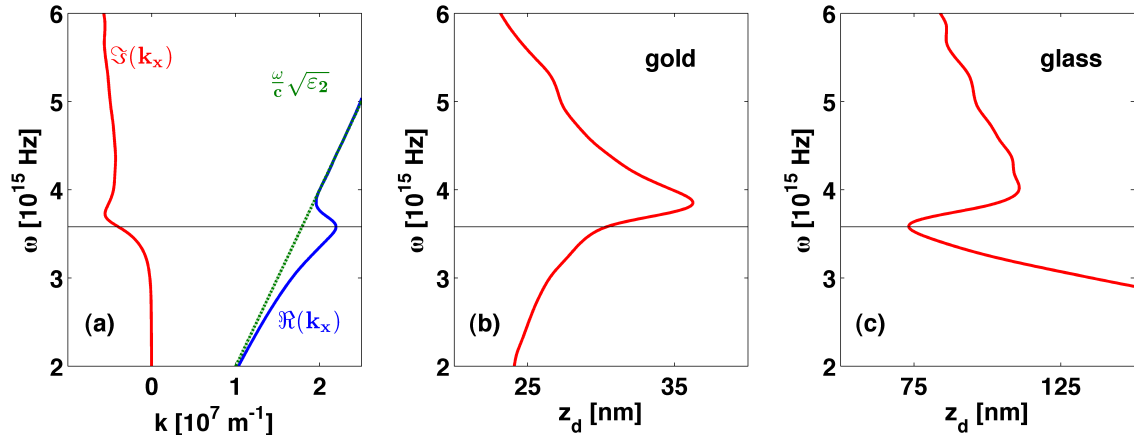


Fig. 2.4: (a) The SPP mode can have momentum  $\Re(k_x)$  above the light-line  $\omega/c\sqrt{\varepsilon_2}$ . This suggests that the mode is a hybrid mode of light and plasma; The decay distance of the field, defined as the distance where the field intensity drops to  $1/e^2$  of its value at the interface, plotted for (b) gold and (c) glass half-space. The value of permittivity of gold was taken from Ref. [46].

$k_x$  can become larger than the light line in glass, given by  $(\omega/c)\sqrt{\varepsilon_2}$ , for certain frequencies. The momentum of the mode beyond the light-line threshold suggests that the mode is not a pure light mode. Another process has to be involved to deliver the additional momentum. This additional process, in fact, is the oscillation of surface charge electrons in a metal. The resulting mode is thus a hybrid light-plasma mode and this justifies its name - the Surface Plasmon Polariton (SPP).

The above light-line momentum in the  $x$ -direction also suggests that some evanescent waves have to be present in the system. This is indeed the case. The field of the mode is evanescent in both half-spaces. Fig. 2.4b,c shows the decay distances,  $z_d^{gold}$

and  $z_d^{glass}$ , of the field perpendicular to the gold-glass interface. The decay distance of the field can be calculated using

$$z_d^{gold} = 1/\Im(k_{1,z}) \quad z_d^{glass} = 1/\Im(k_{2,z}). \quad (2.34)$$

This shows an interesting behaviour of the SPP mode. The best confinement, in the glass half-space, appears for the same frequency as the peak in  $\Re(k_x)$ . This result is not surprising when we look back at the argumentation presented in Sec. 2.3. There we showed that the larger the imaginary component of the wavevector in one direction, the more stretched are the wavevectors in perpendicular directions. In the same section, we have also proved that in such a scenario, light can be confined to smaller volumes than the far-field optical elements permit. But does the SPP mode squeeze the light more than ordinary far-field modes?

The frequency, for which the peaks in  $z_d^{glass}$  and  $\Re(k_x)$  appear, is equivalent to a glass wavelength of  $\lambda = 520$  nm. At this wavelength, the light in glass, in the direction perpendicular to the interface, is confined within few tens of nanometers of the interface (Fig. 2.5). Furthermore, the above light-line momentum in the x-

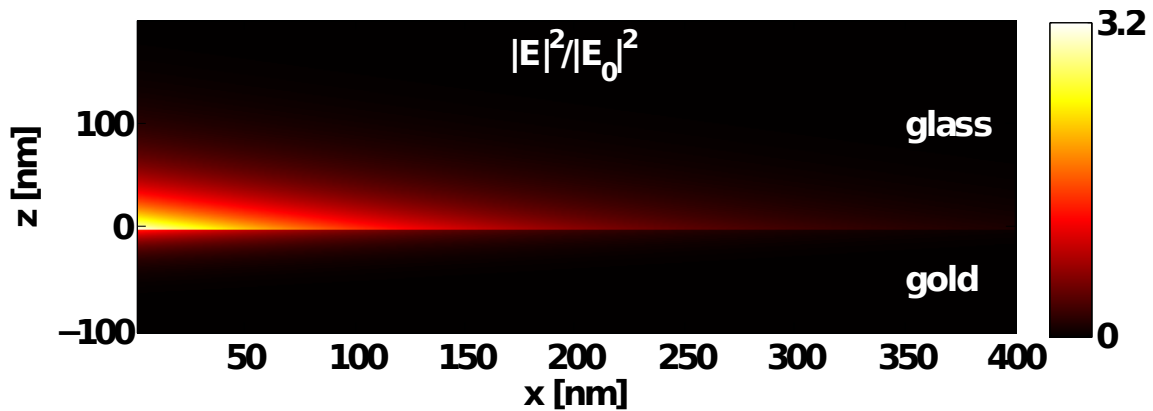


Fig. 2.5: Light can be confined to very small volumes by utilising the SPP mode. The depicted intensity distribution in gold and glass half-spaces was calculated for the glass wavelength of  $\lambda = 520$  nm.

direction ensures that interference of SPP modes can achieve better than far-field confinement of light in x-direction as well. Consequently, we can see that the light confinement utilising plasmon resonances is truly extreme.

One striking example of the intimate relationship between light and surface plasmons was the observation of extraordinary optical transmission through sub-wavelength hole arrays [47]. According to diffraction theory, holes with the diameter much smaller than the wavelength of light should transmit light very poorly. Furthermore, the portion of the light that squeezes through the hole is scattered in all directions. This is just another consequence of Heisenberg's uncertainty relation and a major limitation for all photonic devices. Why? Because the usual application of photonic devices is not only to squeeze the light to a very small volume, but also

to channel the same light out in a well-defined direction. Ebbesen et al. [47] made a very exciting observation that challenged this fundamental belief. They observed extraordinarily high far-field transmission of light when illuminating an array of holes of only 150 nm in diameter with light at  $\lambda = 1500$  nm. John Pendry coined this phenomenon "a Houdini trick" [48], because the light essentially managed to escape to the other side of the array of holes by fitting itself into holes that were far too small for it. The essence of the trick is in the light's ability to disguise itself in a "schizophrenic" state of a SPP. In the proximity of the hole, part of the incident light is transformed into surface plasmon and the other part keeps the identity of a photon in a dielectric medium. Crucially, the two are bound together. This new "schizophrenic" state finds it much easier to travel through the small hole as the energy is partially carried by plasmon inside the metal which is outside of the hole. The SPP travels along the hole's metal interface and once it gets to the other side of the hole, the bound SPP transforms back into propagating light.

We can see this kind of transition between polariton and plasmon portions of the mode in Figs. 2.4a,b,c. Initially, the mode is more polariton in nature. However, as we increase the frequency  $\omega$ , light finds it increasingly easier to penetrate into metal (Fig. 2.4b). In fact, most of the energy of the mode becomes confined inside the metal. The transition of the mode into metal is also supported by the shape of the  $\Im(k_x)$  curve in Fig. 2.4a, which shows that the losses and the maximum penetration depth into the metal are maximised for approximately the same frequency.

In conclusion, we can see, that this "schizophrenic" or hybridised excitation of photon and surface plasmon is a key tool for extremely small scale light confinement. The moment we bind the light with plasmon, we gain much better control over it.

There are, however, some drawbacks of the SPP. First, the simple geometry of two half-spaces does not allow for simple tunability of resonance condition. Furthermore, the above light-line momentum of the mode, given by  $\Re(k_x)$ , does not allow for simple excitation of this modes by light. Fortunately, both drawbacks can be easily resolved by considering light-plasma modes supported by metallic nanoparticles - localised surface plasmon polaritons (LSPPs). These localised modes also support evanescent fields and this allows, through analogy with SPP, an exceptional light confinement near the surface of the nanoparticles. In this case, however, confinement can be achieved in all three dimensions which is of much higher interest for the field of optical trapping. Why? In the case of a SPP, the excitation beam would couple with SPP in diffraction limited area. The nanoparticle would thus be confined very well only in the direction perpendicular to the interface but its in-plane motion will be relatively unrestricted. On the other hand, the LSPP mode provides extreme confinement in all three dimensions, which is extremely important for optical trapping purposes. For these reasons let us now have a closer look at the physics of the LSPP modes.

### 2.4.2 LSPP mode

The easiest way to find the localised plasmon polariton modes for metallic nanoparticles is to solve Maxwell's equations in quasi-static approximation. In this approximation, all the electrons in the particle respond simultaneously to the external field<sup>8</sup> and the electric field  $\mathbf{E}$  can be simply described by the electrostatic potential  $\Phi$  using

$$\mathbf{E} = -\nabla\Phi. \quad (2.35)$$

Inserting this equation into Eq. (2.28) results in the Laplace equation for the electrostatic potential

$$\nabla^2\Phi = 0. \quad (2.36)$$

Solving this equation for a spherical particle of radius  $a$  and permittivity  $\varepsilon_1$  in a medium of permittivity  $\varepsilon_2$  in an external field  $\mathbf{E}_0 = E_0\hat{z}$  results in the following electrostatic potential inside and outside of the sphere (full derivation in Appendix B):

$$\Phi_1 = -\frac{3\varepsilon_2}{\varepsilon_1 + 2\varepsilon_2}E_0z, \quad (2.37)$$

$$\Phi_2 = -E_0z + \frac{\varepsilon_1 - \varepsilon_2}{\varepsilon_1 + 2\varepsilon_2}E_0a^3\frac{z}{r^3}. \quad (2.38)$$

Finally, using  $\mathbf{E} = -\nabla\Phi$ , we obtain for the electric field inside and outside of the sphere

$$\mathbf{E}_1 = (0, 0, E_0) - \left(0, 0, \frac{\varepsilon_1 - \varepsilon_2}{\varepsilon_1 + 2\varepsilon_2}E_0\right) \quad (2.39)$$

$$\mathbf{E}_2 = (0, 0, E_0) + E_0\frac{\alpha}{4\pi} \left(\frac{3xz}{r^5}, \frac{3yz}{r^5}, \frac{3z^2}{r^5} - \frac{1}{r^3}\right), \quad (2.40)$$

where  $\alpha$  is the polarizability of the sphere given by

$$\alpha = 4\pi a^3 \frac{\varepsilon_1 - \varepsilon_2}{\varepsilon_1 + 2\varepsilon_2}. \quad (2.41)$$

We can see that the electric field outside of the gold sphere is composed of two parts. First part represents the initial field  $\mathbf{E}_0$ . The second part is a field of point dipole located at the centre of the sphere. The magnitude of this dipole field naturally scales with magnitude of the initial field  $\mathbf{E}_0$ . However, it also scales with polarizability  $\alpha$ .

If we now begin to slowly vary the field, by introducing the term  $e^{i\omega t}$ , the intensity of the dipole at any moment will strongly depend on the permittivity of respective materials. Since the permittivity of gold depends on  $\omega$ , we can write the intensity factor of the dipole as

$$|\alpha(\omega)|^2 = 16\pi^2 a^6 \left| \frac{\varepsilon_1(\omega) - \varepsilon_2}{\varepsilon_1(\omega) + 2\varepsilon_2} \right|^2. \quad (2.42)$$

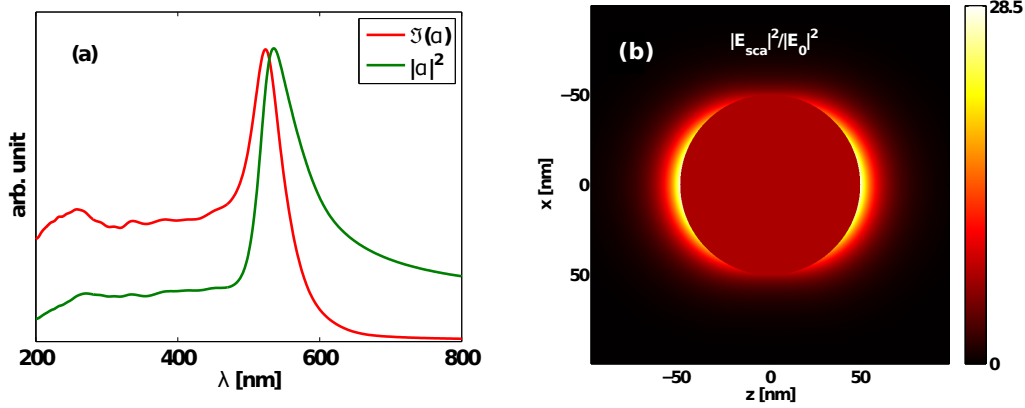


Fig. 2.6: (a) The peak in scattered intensity determined from  $|\alpha(\omega)|^2$  appears for similar wavelength as the maximum heating in the system given by  $\Im(\alpha(\omega))$ ; (b) The scattered intensity profile near gold nanoparticle, with radius of  $a = 50$  nm, at its respective resonant wavelength. The intensity is strongly confined to the surface of the particle.

Fig. 2.6a reveals that the dipole intensity factor has resonant character with a peak in dipole intensity appearing near  $\lambda = 532$  nm. This peak in dipole intensity is due to strong coupling of the light and the electrons in the metallic nanoparticle - the LSPP mode.

Fig. 2.6b further shows the intensity of the field for a gold nanoparticle with  $a = 50$  nm for the resonant wavelength of  $\lambda = 532$  nm. You can clearly see that the field is very strongly confined near the surface of the particle. This strong light confinement is the reason why the plasmon resonant structures induce such strong optical traps. It is because the LSPPs can pinch the light into nanoscale volumes and as a consequence the gradient of the intensity becomes very steep.

The sphere is of course not the only metallic nanostructure supporting the LSPP mode. Virtually any shape can support localised plasmon modes. Fig. 2.7 shows, as an example, field profile in the proximity of two other structures - namely split ring resonators and optical nanoantennas - that also support LSPP modes. In both of these examples, electromagnetic field is confined very strongly in the gaps. In fact, the smaller we make the gap, the better the field confinement becomes.<sup>9</sup>

There is, however, a price to be paid for this exceptionally strong light confinement and this is the heating of the metal. The power dissipated in the metal, for

<sup>8</sup>This is only true for particles with characteristic size much smaller than the wavelength of light. As a result, the phase of the light is also usually constant within the volume of the particle (see Fig. 1.4 in Chapter 1). For this reason the point-dipole and the quasi-static approximations look equivalent in many scenarios. However, the quasi-static approximation is more general as it can account not just for dipole mode but also for higher order modes.

<sup>9</sup>This behaviour breaks for extremely small gap sizes when the macroscopic Maxwell's equations fail to capture the quantum effects of the electrons near the gap.

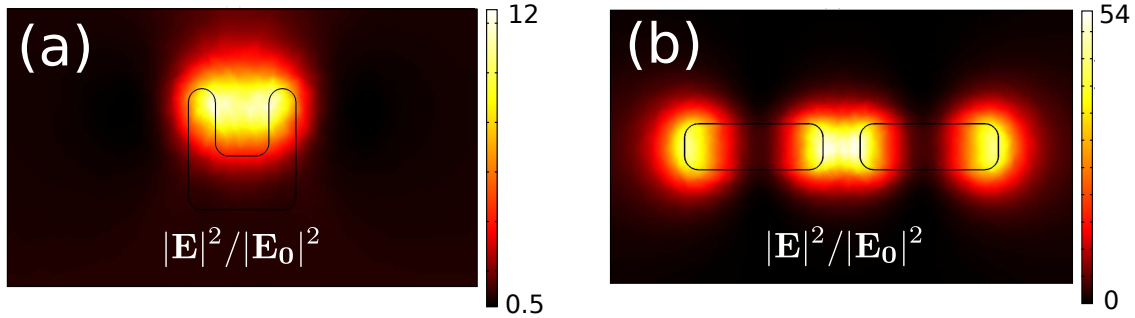


Fig. 2.7: The LSPP modes are supported by various shapes of metallic structures. Here the field  $|E|^2$  is presented for (a) split-ring resonator and (b) dipole nanoantenna. The field is plotted for a plane 20 nm above the structures.

the case of small particles, can be described by

$$P_{\text{dissipated}} \propto \Im(\alpha(\omega)) \quad (2.43)$$

which peaks for approximately the same wavelength as the  $|\alpha(\omega)|^2$  (Fig. 2.6a), which means that heating and strong field confinement are very difficult to separate.

The dilemma between the heating and the strong light confinement was an essential problem in the field of optical manipulation when I started my PhD. The first experimental demonstrations realising trapping with plasmonic structures [4, 34, 41, 42] mentioned heating only marginally. Based on these observations, we felt that a detailed study of the optical forces and the related heating near a metallic structure is missing. The results of this study are presented in the following chapter and were published in Ref. [5].

## 2.5 Utilisation of LSPP mode for particle sorting

For small particles, the scattering and absorption cross-sections are closely related to particle's polarizability [3]

$$C_{\text{sca}} \propto |\alpha(\omega)|^2, \quad (2.44)$$

$$C_{\text{abs}} \propto \Im(\alpha(\omega)), \quad (2.45)$$

and a closer look at Fig. 2.6a thus suggests that the 'push' force acting on a particle will be significantly increased for its respective resonant frequency. However, the position of the resonance peak seems to be independent of particle size since the frequency dependent polarizability depends only on the material of the particle and the surrounding medium. This contradicts our claims that the plasmon resonance peak red-shifts for increasing particle size.

This apparent controversy stems from the quasi-static approximation used so far in our discussion. The quasi-static approximation is very useful for physical insight in many situations but, unfortunately, the approximation is only valid if the whole particle can be assumed to respond simultaneously to the applied external field. As a result, the quasi-static approximation is accurate only for particles

with the characteristic size much smaller than the wavelength of external field. As the characteristic size of the particles used in our sorting application, presented in Chapter 4, is comparable (particle diameter equal  $\approx \lambda/5$ ) to the wavelength used for particle sorting, we have to remove the quasi-static restriction and solve the full electrodynamic scattering problem to reveal the shift of resonance peak. The full electrodynamic problem of a sphere in external field, which includes the retardation effects as well as the effect of multipoles, can be either solved analytically (Mie solution [49]) or numerically. Unfortunately, due to complex nature of both methods, we cannot provide a quantitative explanation of the resonance red-shift in this chapter. Both methods are introduced in the next chapter and the subsequent study of the role of retardation effects on the red-shift of the plasmon resonance for increasing particle size is then discussed in Chapter 4.

## **2.6 Conclusion**

In conclusion, we have seen that the plasmon resonances can be used to significantly enhance the optical forces acting on nanoscale objects. The 'push' force acting on small spheres can be significantly enhanced for resonance condition due to improved coupling of light and plasmon. This enhancement of 'push' force for resonant condition can be subsequently utilised for particle sorting. This is presented in Chapter 4. Furthermore, nanostructures supporting plasmon resonances can be used as near-field lenses to produce extreme light confinement which enhances crucial element of optical trapping - the gradient forces. Unfortunately, the field confinement is accompanied by significant heating and the interplay between the two competing phenomena - heating and confinement - is often overlooked in the literature. For this reason, we study this intriguing interplay of heating and confinement in the following chapter.

## Chapter 3

# Enhanced optical forces and heating near plasmon resonant nanoantenna

In the previous chapter we have seen that light can be confined to very small volumes by exploiting the effect of the plasmon resonance. This creates very strong field gradients which in turn produce very large gradient forces. The popularity of plasmonic nanostructures in the field of optical trapping stems from the fact that plasmonic structures can offer superior field confinement compared to other near-field methods [8]. However, the exceptional field confinement is accompanied by significant heating in the metallic structure supporting the plasmon resonance (see Sec. 2.4.2 and Ref. [6]). This trade-off between the field confinement and heating actually makes plasmonic structures less appealing for optical trapping purposes, especially in situations when biological specimen has to be trapped. In such situations, other than plasmon based near-field methods, such as dielectric surface resonators [50] or slot waveguides [51], might provide acceptable gradient forces with negligible concomitant heating.

Also, when compared to conventional far-field tweezers, the near-field methods, plasmonic tweezers included, suffer from the inability to move the trapped specimen around and deliver it efficiently into place of interest. And although some methods to manipulate the trapped specimen near plasmonic nanostructures exist [6, 44] the scope of this manipulation is currently restricted to one dimension only (manipulation on a one dimensional curve).

Furthermore, the intensity in the proximity of plasmonic structures peaks at the metal interface which implies that the trapping is intrinsically contact in nature. This is in stark contrast to conventional tweezers where the trapped specimen resides in free space. The contact nature of the trapping near plasmonic nanostructures brings possible complications to the interpretation of observed immobilisation of particles. Particles in close proximity to nanostructure can, for example, simply adhere to the nanostructure through chemical binding and other surface induced forces. This non-optical induced trapping can be usually factored out by switching

on and off the laser exciting the plasmon resonance and observing the response of the particle. The test is based on the fact that upon switching off the laser the optical forces in the system almost instantly disappear whereas other forces will remain. Consequently, the particles trapped by optical forces should quickly diffuse away from the trapping site, while the particles trapped by other means should stay in place. Unfortunately, this simple test is often twisted in plasmonic trapping research. For example, the study in Ref. [45] claims optical trapping of 10 nm gold nanoparticles in the gap of nanoantenna. Their argumentation that the trapping is induced by optical forces is based on their observation that upon switching off the laser the particle escapes from the trap after 1.5 min!

Another example of the misleading interpretation in plasmonic trapping applications is often related to the way the trapping efficiency is defined. In conventional tweezers, the incident intensity correlates fairly well with the intensity experienced by the trapped specimen. This means that a simple ratio of force and incident intensity closely corresponds to the trapping efficiency. An analogous approach is very misleading in the case of plasmonic trapping. First of all, the nanostructures are usually excited with beams incident at the critical angle to the interface upon which the nanostructures reside. In such a case, the intensity at the interface is usually several times larger than the actual incident intensity [52]. This increased intensity is further enhanced by the plasmon resonance. As a consequence, the actual intensity near the plasmonic structure can be orders of magnitude higher than the stated incident intensity (Fig. 3.1). This clearly shows that the local intensity experienced

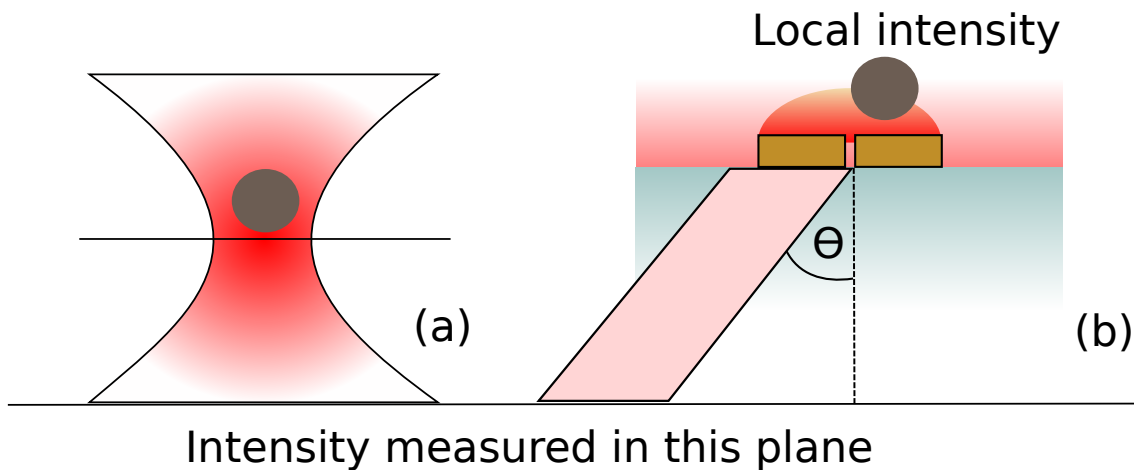


Fig. 3.1: (a) In the case of trapping with Gaussian beam the incident intensity closely corresponds to the local intensity experienced by the particle; (b) In the case of trapping with plasmonic nanostructures the value of incident intensity is not equivalent to the local field intensity as experienced by the particle. The incident intensity is enhanced in two steps - first at the interface due to critical angle incidence and secondly by the plasmon resonant nanoantenna. The final local intensity can thus be orders of magnitude higher than the stated incident intensity.

by the particle, rather than the incident intensity, should be used as a figure of merit in the optical trapping applications when comparing the efficiency to conventional optical tweezers. This would reveal the true contribution of increased gradient forces as opposed to the rather indirect enhancement of local intensity [4, 53]. Some of the experimental realisations, particularly trapping with nanopillars [34] also operate at powers that in similar scenarios [54] increase temperature close to the boiling point of water. This is particularly worrying because it was shown that, at a given power, the heating of water is roughly 20 times smaller than the heating of the underlying metal [54]. The fundamental question then is whether the higher gradient forces and lower incident intensity offsets the heating in trapping applications with plasmonic structures.

Unfortunately, the above described unfair interpretations of experiments were quite common in plasmonic trapping community at the very beginning which, to some extent, undermined the credence of this field and raised expectations that might not be fully justified.

The lack of rigour and vague interpretations, particularly with respect to heating and local field intensities [4, 53], motivated our research presented in this chapter and published in Ref. [5]. What was especially missing in the literature at the time was a detailed theoretical description of optical forces and the underlying effect of heating in the proximity of plasmon resonant structures. The study was performed for a special case of nanoantenna, which was a popular choice for optical trapping due to ease of tunability of their plasmon resonance peak [55] and also due to relatively simple fabrication protocol.

In this chapter, we will explore in detail the nanoantenna structure used for trapping of dielectric nanospheres for the cases of both, normal and total internal reflection incidence, the latter which was recently reported in Ref. [4]. The first part of the chapter describes the theoretical framework for calculation of optical forces based on Maxwell's stress tensor approach [56]. This approach is more general than the gradient and scattering force approach presented in the previous chapter. It provides the net force generated by the electromagnetic field in any situation without any approximations. The second part of the chapter then contains the results of the simulations and the comparison of several experimental situations.

## **3.1 The theory of the optical forces**

### **3.1.1 The Maxwell stress tensor method**

The force exerted on an object positioned in a time-harmonic electromagnetic field of frequency  $\omega$  can be obtained by using the law of conservation of linear momentum. The linear momentum can be present in the system as either electromagnetic field momentum or mechanical momentum of the object. The sum of these two, which is the total momentum of the system, is conserved. In an optical interaction of object with electromagnetic field the momentum is transferred from one form to another. This change of momentum, from field to mechanical, exhibits itself as a mechanical force acting on the object. Indeed, the force  $\mathbf{F}$  acting on the object corresponds to

the variation of the mechanical momentum  $\mathbf{p}$  leading to  $\mathbf{F} = d\mathbf{p}/dt$ .

The electromagnetic field momentum flux in the linear medium of relative permittivity  $\epsilon_m$  and permeability  $\mu_m$  is represented mathematically by the Maxwell stress tensor [56]

$$\sigma_{ij} = \epsilon_0 \epsilon_m E_i E_j + \mu_0 \mu_m H_i H_j - \frac{1}{2} \delta_{ij} (\epsilon_m \epsilon_0 E_k E_k + \mu_m \mu_0 H_k H_k), \quad (3.1)$$

where we used implicit summation on repeating indices and  $E_i$  and  $H_i$  correspond to the electric and magnetic fields. This form of the Maxwell stress tensor can be cast into a simpler form in harmonic fields, where the following equation holds

$$E_i(\mathbf{r}, t) = \Re [E_i(\mathbf{r})e^{i\omega t}] = \frac{1}{2} (E_i(\mathbf{r})e^{i\omega t} + E_i^*(\mathbf{r})e^{-i\omega t}). \quad (3.2)$$

Using the above equation, we can write the product of any two field components as

$$\begin{aligned} E_i H_j &= \frac{1}{4} (E_i(\mathbf{r})e^{i\omega t} + E_i^*(\mathbf{r})e^{-i\omega t}) (H_j(\mathbf{r})e^{i\omega t} + H_j^*(\mathbf{r})e^{-i\omega t}) \\ &= \frac{1}{2} \Re (E_i H_j^* + E_i H_j e^{2i\omega t}). \end{aligned} \quad (3.3)$$

As we are only interested in quantities averaged over one optical cycle, we can write the cycle averaged Maxwell stress tensor in the following form

$$\langle \sigma_{ij} \rangle = \frac{1}{2} \Re \left[ \epsilon_0 \epsilon_m E_i E_j^* + \mu_0 \mu_m H_i H_j^* - \frac{1}{2} \delta_{ij} (\epsilon_m \epsilon_0 E_k E_k^* + \mu_m \mu_0 H_k H_k^*) \right], \quad (3.4)$$

where  $\langle \dots \rangle$  corresponds to  $\frac{1}{T} \int_0^T \dots dt$  with  $T = 2\pi/\omega$ .

Now imagine an object inserted into space of volume  $V$  with boundary given by a closed surface  $S$ . If we integrate the flux flow of electromagnetic momentum across the surface  $S$  and observe non-zero electromagnetic momentum flux flow then a sink or a source of electromagnetic momentum exists in volume  $V$ . This can only be explained by transformation of momentum from electromagnetic to mechanical. The electromagnetic force acting on an object can thus be written as

$$\langle F_i \rangle = \int_S \langle \sigma_{ij} \rangle n_j dS, \quad (3.5)$$

where  $n_j$  is the outward unit normal to the closed surface  $S$ . The problem of finding the optical force acting on an object thus reduces to finding the solution of the  $E_i$  and  $H_i$  fields.

### 3.1.2 Model for solving $E_i$ and $H_i$

In order to determine the optical forces we need to find the form of the fields  $E_i$  and  $H_i$ . This can be done analytically for certain simple geometries. For example, an analytical solution of the scattering problem for a sphere exists (Mie solution [49]).

The extension of Mie theory, the T-matrix approach [57], also exists and is suited for more general geometries. Unfortunately, the above mentioned purely analytical methods cannot be used for structures positioned at the interface between two media, which is often the case in optical trapping applications. In such a situation one of the semi-analytical methods such as multiple multipole method or volume integral method is available [14]. However, due to rapid increase of computational power of computers, pure numerical methods, such as the finite element method (FEM) or the finite-difference time-domain method (FDTD), are becoming increasingly popular and analytical and semi-analytical methods are only used as a way to validate the output from purely numerical methods. In the following studies we will adopt a pure numerical approach based on the FEM method in the implementation from COMSOL Multiphysics. The validity of the FEM model will be always benchmarked with respect to Mie theory. The process of benchmarking is described in Sec. 3.1.3.

Any time-harmonic scattering problem can be efficiently solved using the scattered field formulation of the RF Module supplied with COMSOL Multiphysics. The equation solved by FEM solver can be easily derived from Maxwell's equations (this time with sources included for more generality)

$$\nabla \times \mathbf{E} = -\frac{\partial \mathbf{B}}{\partial t}, \quad (3.6)$$

$$\nabla \times \mathbf{H} = \mathbf{j} + \frac{\partial \mathbf{D}}{\partial t}, \quad (3.7)$$

$$\nabla \cdot \mathbf{D} = \rho, \quad (3.8)$$

$$\nabla \cdot \mathbf{B} = 0. \quad (3.9)$$

In all the subsequent discussions, we will assume that the materials involved are homogeneous and isotropic, which means that no tensorial description for optical properties is needed. Further, linear constitutive relations

$$\mathbf{j} = \sigma(\omega)\mathbf{E}, \quad \mathbf{D} = \varepsilon(\omega)\mathbf{E}, \quad \mathbf{B} = \mu(\omega)\mathbf{H} \quad (3.10)$$

are assumed, which is a reasonable assumption for incident intensities used in this thesis. This form of linear constitutive relations also allows us to treat the calculations as the time-harmonic problem and furthermore, the optical forces resulting from different spectral components can be simply added together. Using the material equations, we can re-write first two Maxwell's equations as

$$\nabla \times \mathbf{E} = -\mu \frac{\partial \mathbf{H}}{\partial t}, \quad (3.11)$$

$$\nabla \times \mathbf{H} = \sigma \mathbf{E} + \varepsilon \frac{\partial \mathbf{E}}{\partial t}. \quad (3.12)$$

Further, as our problem is time-harmonic and our excitation field is going to be composed of monochromatic plane-waves with angular frequency  $\omega$ , we can assume that all variables have time dependence of  $e^{i\omega t}$ . This gives us Maxwell's equations in time-harmonic form

$$\nabla \times \mathbf{E} = -i\omega\mu\mathbf{H}, \quad (3.13)$$

$$\nabla \times \mathbf{H} = (\sigma + i\omega\varepsilon) \mathbf{E}. \quad (3.14)$$

Substitution of the first equation into the second gives

$$\frac{1}{\mu} (\nabla \times \nabla \times \mathbf{E}) - (\omega^2\varepsilon - i\omega\sigma) \mathbf{E} = 0. \quad (3.15)$$

Using  $\mu = \mu_0\mu_r$ ,  $\varepsilon = \varepsilon_0\varepsilon_r$ ,  $\omega = k_0c_0$  and  $c_0 = 1/\sqrt{\varepsilon_0\mu_0}$ , we can finally write

$$\frac{1}{\mu_r} \nabla \times \nabla \times \mathbf{E} - k_0^2 \left( \varepsilon_r - i \frac{\sigma}{\omega\varepsilon_0} \right) \mathbf{E} = 0, \quad (3.16)$$

where  $\varepsilon_r - i(\sigma/\omega\varepsilon_0) = \hat{\varepsilon}$  is the complex permittivity.<sup>1</sup> For non-magnetic case we further assume  $\mu_r = 1$ . So, at last, we can write the equation in a more compact form as

$$\nabla \times \nabla \times \mathbf{E} - k_0^2 \hat{\varepsilon} \mathbf{E} = 0. \quad (3.17)$$

This is the partial differential equation solved by FEM solver. The solution for  $\mathbf{H}$  can then be found using Eq. (3.13).

In scattered field formulation of the problem, the solver solves only for scattered electric field  $\mathbf{E}_{sca}$ . This means that the initial field  $\mathbf{E}_i$  has to be given to the solver as input. If we write the total electric field as  $\mathbf{E} = \mathbf{E}_i + \mathbf{E}_{sca}$  the above equation can be written in the following form

$$\nabla \times \nabla \times \mathbf{E}_{sca} - k_0^2 \hat{\varepsilon} \mathbf{E}_{sca} = - (\nabla \times \nabla \times \mathbf{E}_i - k_0^2 \hat{\varepsilon} \mathbf{E}_i). \quad (3.18)$$

Any incident field can be written as the linear superposition of plane-waves. This implies that the only incident solution we are interested in is either s- or p-polarised plane-wave incident at a certain angle  $\theta_i$ . In the following, we will also deal only with one interface (glass-water) in the computational domain. This reduces the problem to finding Fresnel transmission and reflection coefficients of the given interface.

The incident field can be expressed in the glass domain for p-polarised plane-wave (assuming  $\mathbf{k}$ -vector in  $yz$ -plane (Fig. 3.2)) as

$$E_{y,p}^g(x, y, z) = A \left[ -e^{-ik_g(\cos\theta_i z + \sin\theta_i y)} + R_p e^{-ik_g(-\cos\theta_i z + \sin\theta_i y)} \right] e^{i\phi} \cos\theta_i, \quad (3.19)$$

$$E_{z,p}^g(x, y, z) = A \left[ e^{-ik_g(\cos\theta_i z + \sin\theta_i y)} + R_p e^{-ik_g(-\cos\theta_i z + \sin\theta_i y)} \right] e^{i\phi} \sin\theta_i, \quad (3.20)$$

where  $A$  is the amplitude of plane-wave,  $k_g$  is the wave-number in glass and  $R_p$  is the Fresnel coefficient of reflection<sup>2</sup>

$$R_p = \left( \frac{n_w \cos\theta_i - n_g \cos\theta_t}{n_w \cos\theta_i + n_g \cos\theta_t} \right)^*, \quad (3.21)$$

where  $n_g = 1.518$  and  $n_w = 1.33$  are the refractive indices of glass and water respectively and  $\theta_t$  is the angle of transmitted wave [49].

<sup>1</sup>For the other possible choice of time dependency, namely  $e^{-i\omega t}$ , the complex permittivity is of the form  $\hat{\varepsilon} = \varepsilon_r + i(\sigma/\omega\varepsilon_0)$ . The sign is important for correct interpretation of tabulated data of optical constants of noble metals.

<sup>2</sup>The conjugation is necessary for incident angles above the critical angle.

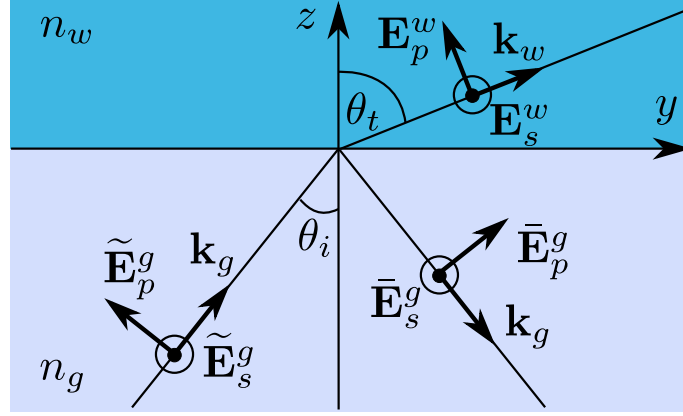


Fig. 3.2: Reflection ( $\bar{\mathbf{E}}$ ) and refraction ( $\mathbf{E}$ ) of an incident plane-wave ( $\tilde{\mathbf{E}}$ ) with wavevector in  $yz$ -plane.

In water domain, the equations have the following form

$$E_{y,p}^w(x, y, z) = A [-T_p e^{-ik_w((\cos \theta_t)^* z + \sin \theta_t y)}] e^{i\phi} (\cos \theta_t)^*, \quad (3.22)$$

$$E_{z,p}^w(x, y, z) = A [T_p e^{-ik_w((\cos \theta_t)^* z + \sin \theta_t y)}] e^{i\phi} \sin \theta_t, \quad (3.23)$$

where the  $T_p$  is the Fresnel transmission coefficient given by

$$T_p = \left( \frac{2n_g \cos \theta_i}{n_w \cos \theta_i + n_g \cos \theta_t} \right)^*. \quad (3.24)$$

The incident field in the glass domain, for s-polarised plane-wave, can be expressed as

$$E_{x,s}^g(x, y, z) = A [e^{-ik_g(\cos \theta_i z + \sin \theta_i y)} + R_s e^{-ik_g(-\cos \theta_i z + \sin \theta_i y)}] e^{i\phi}, \quad (3.25)$$

where the Fresnel reflection coefficient for s-polarisation  $R_s$  is

$$R_s = \left( \frac{n_g \cos \theta_i - n_w \cos \theta_t}{n_g \cos \theta_i + n_w \cos \theta_t} \right)^*. \quad (3.26)$$

In the water domain, the equation for s-polarised incident plane-wave is

$$E_{x,s}^w(x, y, z) = A [T_s e^{-ik_w((\cos \theta_t)^* z + \sin \theta_t y)}] e^{i\phi}, \quad (3.27)$$

where the Fresnel coefficient of transmission for s-polarisation  $T_s$  is given by

$$T_s = \left( \frac{2n_g \cos \theta_i}{n_g \cos \theta_i + n_w \cos \theta_t} \right)^*. \quad (3.28)$$

In order to solve Eq. (3.18), we further need to specify permittivity of all the computational domains. This is easily done for glass and water as  $n = \sqrt{\epsilon}$ . As the

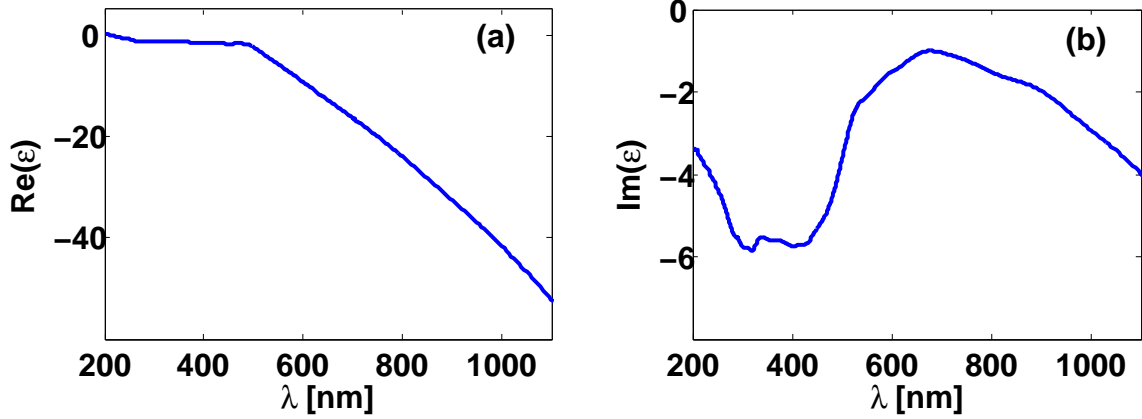


Fig. 3.3: The (a) real and (b) imaginary part of the permittivity of gold [46]. The imaginary part is negative due to the selected time-harmonic convention of  $e^{i\omega t}$ .

rest of the thesis considers only gold nanostructures that are sufficiently large, we can use the bulk value of the permittivity as presented in Ref. [46] (Fig. 3.3).

Equipped with the incident field  $E_i$  and the permittivity of materials, we can solve Eq. (3.18) in any time-harmonic situation with the only restriction being on the maximum velocity of the particle upon which the optical forces are being exerted. The particle's velocity must be assumed sufficiently small so that Doppler shift effects and Lorentz forces are negligible. In nanoparticle optical tweezers applications, those assumptions are easily satisfied.

The last input for the solver are the boundary conditions. We do not have to use all the boundary equations to fully determine the problem. In fact, the continuity of tangential field components is satisfactory and proves more useful for the solver based on Eq. (3.18). The boundary equations used by the solver, for no sources at the boundary, are given by

$$\mathbf{n} \times (\mathbf{E}^w - \mathbf{E}^g) = 0, \quad \mathbf{n} \times (\mathbf{H}^w - \mathbf{H}^g) = 0, \quad (3.29)$$

where  $\mathbf{n}$  is the normal to the interface of the two domains. However, the solver does not have a direct access to magnetic field during solving, so that in reality the second equation, actually used by the solver, is

$$\begin{aligned} \mathbf{n} \times (\mathbf{H}^w - \mathbf{H}^g) &\rightarrow -\mathbf{n} \times i\omega\mu_0(\mathbf{H}^w - \mathbf{H}^g) = \\ &= \mathbf{n} \times ((\nabla \times \mathbf{E})^w - (\nabla \times \mathbf{E})^g) = 0. \end{aligned} \quad (3.30)$$

Armed with all these assumptions and limitations of our model we are now fully prepared to proceed to the solution of the scattering problem and find fields  $E_i$  and  $H_i$ .

### 3.1.3 Validation of the model

The output of the numerical model should be always validated by at least two independent methods, even in the case of the commercial solvers. In fact, the

validation of the model is usually the most time intensive task of the modelling process. In this section, we will briefly discuss some of the common strategies for validation of the scattering model.

The first step when setting up a model based on the scattering formulation, given by Eq. (3.18), is to verify that in the absence of the scatterer, the input field  $\mathbf{E}_{\text{inc}}$  gives zero scattered field  $\mathbf{E}_{\text{sca}}$ . This step seems to be trivial but it can reveal serious problems in the model setup. For example, one of the early versions of COMSOL Multiphysics contained an error in the formulation of the Perfectly Matched Layer (PML). The PML is a layer that has to be included to simulate unbounded scattering problems. Since any real computation domain has to be finite, the question arises what boundary conditions to use in the truncated model to mimic the infinite character of the problem. The solution to this problem was suggested by Berenger [58], who was the first to introduce the PML. The PML is in fact not a boundary, but rather an additional domain with specific material properties that absorbs the incoming electromagnetic field and does not reflect any field back into computational domain. It can be shown [59] that the ideal absorbing material is anisotropic with permittivity and permeability of the material defined as

$$\epsilon = \epsilon_0 \epsilon_r \begin{pmatrix} \frac{s_y s_z}{s_x} & 0 & 0 \\ 0 & \frac{s_x s_z}{s_y} & 0 \\ 0 & 0 & \frac{s_x s_y}{s_z} \end{pmatrix}, \quad \mu = \mu_0 \mu_r \begin{pmatrix} \frac{s_y s_z}{s_x} & 0 & 0 \\ 0 & \frac{s_x s_z}{s_y} & 0 \\ 0 & 0 & \frac{s_x s_y}{s_z} \end{pmatrix}, \quad (3.31)$$

where

$$s_x = a_x - ib_x, \quad s_y = a_y - ib_y, \quad s_z = a_z - ib_z, \quad (3.32)$$

where the parameters are set according to the problem. When, for example, we want the material to be absorbing in the  $x$ -direction, then we have to choose the parameters  $a$ ,  $b$  in such a way to get  $s_x = 1 - i$ ,  $s_y = 1$ ,  $s_z = 1$ . This kind of artificial medium basically acts as an efficient absorber for a wide interval of angles and frequencies. The incident wave enters the medium, almost without any reflection, and is attenuated very quickly in the PML subdomain. This means that by the time the wave arrives to the outer boundary of the PML, it is very weak. However, we still have to apply some boundary condition at the open boundary of the PML. Fortunately, the wave is already very weak at the outer boundary which means that we do not have to be concerned so much with reflections. In any case, the numerical accuracy can be increased by using scattering boundary condition at the open boundaries of PML.

Several implementations of PMLs exist. COMSOL was using the anisotropic medium PML formulation mentioned above in the previous versions, but newer versions of COMSOL are using the Stretched coordinate formulation. Unfortunately, due to very different implementation of these methods, an error occurred in the newer version of COMSOL program in scattering mode, giving unwanted reflections from the PML layer. This error, first reported to COMSOL team by myself, was easily revealed during the first validation step of the model, because the scattered field  $\mathbf{E}_{\text{sca}}$  was non-zero even in the absence of the scatterer. The comparison of the reflectivity of the bugged and corrected PML is shown in Fig. 3.4 for incident angles ranging

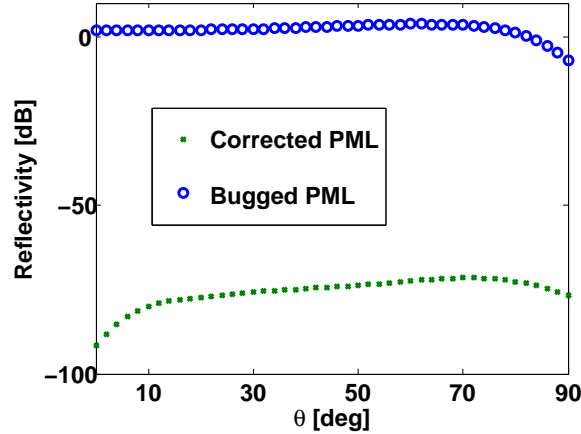


Fig. 3.4: Reflectivity of PMLs for bugged and corrected software implementation.

from 0 to 90 degrees. As you can see, the reflectivity of the bugged implementation of PMLs was actually more than 100 % over a large interval of incident angles, which basically means that the PMLs acted like a field source and enhanced the reflected field.<sup>3</sup> Sadly, the version of the software containing the error was on the market for several months despite the software’s popularity. This reveals a burgeoning need for the repeated validation of the model, especially for high level software like COMSOL, which develops very quickly and each software update might cause problems.

The next step of validation comprises in comparing the results of the numerical model with analytical solution. This can be usually done only for simplified geometries. In scattering problems, the analytical solution of Mie [49] for spherical particles is invaluable for such testing. In scattering problems, the scattering ( $C_{sca}$ ) and extinction cross-sections ( $C_{ext}$ ) are often used to describe the object response to incident electromagnetic field. The extinction cross-section is a parameter that is related to the amount of energy taken from the incident radiation by the object. We can decompose it into the energy dissipated in the object, which will refer to the absorption cross-section ( $C_{abs}$ ), and the energy scattered by the object, which will refer to the scattering cross-section  $C_{sca}$ . This allows us to write

$$C_{ext} = C_{sca} + C_{abs}. \quad (3.33)$$

The scattering and absorption cross-section can be easily obtained from the numerical model. The scattering cross-section is related to the time-averaged power outflow from the computational domain. The absorption cross-section is then related to the time-averaged resistive heating. It is also convenient to define scattering, absorption and extinction efficiencies. Those are basically just corresponding cross-sections

---

<sup>3</sup>It is quite entertaining to see the official statement in hotfix release by COMSOL team which says, literally: "When using the scattered field formulation, the performance of perfectly matched layers (PMLs) has been improved."

divided by the geometrical cross-section of the particle

$$Q_{\text{ext}} = \frac{C_{\text{ext}}}{\pi r^2}, \quad Q_{\text{sca}} = \frac{C_{\text{sca}}}{\pi r^2}, \quad Q_{\text{abs}} = \frac{C_{\text{abs}}}{\pi r^2}. \quad (3.34)$$

The theoretical values for the scattering and the extinction efficiencies are given by [13]

$$Q_{\text{sca}} = \frac{2}{q^2} \sum_{l=1}^{\infty} (2l+1) (|a_l|^2 + |b_l|^2), \quad Q_{\text{ext}} = \frac{2}{q^2} \sum_{l=1}^{\infty} (2l+1) \Re(a_l + b_l), \quad (3.35)$$

where  $q = 2\pi r/\lambda$  ( $\lambda$  is the wavelength in the medium surrounding the particle) and  $a_l, b_l$  are Lorentz-Mie coefficients, which can be derived after lengthy calculations [49]

$$a_l = \frac{\psi_l(q)\psi'_l(mq) - m\psi_l(mq)\psi'_l(q)}{\zeta_l(q)\psi'_l(mq) - m\psi_l(mq)\zeta'_l(q)} \quad (3.36)$$

$$b_l = \frac{m\psi_l(q)\psi'_l(mq) - \psi_l(mq)\psi'_l(q)}{m\zeta_l(q)\psi'_l(mq) - \psi_l(mq)\zeta'_l(q)}, \quad (3.37)$$

where  $m$  is the effective refractive index as defined in Chapter 2 and  $\psi_l(x), \zeta_l(x)$  are Bessel and Hankel functions given by

$$\psi_l(x) = \sqrt{\frac{\pi x}{2}} J_{l+\frac{1}{2}}(x) \quad (3.38)$$

$$\zeta_l(x) = \sqrt{\frac{\pi x}{2}} H_{l+\frac{1}{2}}^{(2)}(x). \quad (3.39)$$

A MatLab script was written to calculate the scattering and extinction efficiencies using this method. The script was tested by comparison with some of the well established results for dielectric [60] and metallic [61] particles over a wide range of values of parameter  $q$ . For example, the scattering efficiency  $Q_{\text{sca}}$  of water particles in air medium for various parameters of  $q$  in Fig. 3.5a is completely identical to that given in [49]. One can also see that the scattering cross-section converges to twice the geometrical cross-section for a very large particles, which is a well known, although somewhat paradoxical, result [49].

The question remains how to compare the results from Mie with those obtained in COMSOL Multiphysics. The parameters that can be calculated quite easily in COMSOL are the scattering and absorption efficiency. The extinction efficiency can be then evaluated using Eq. (3.33). The absorption efficiency is clearly proportional to the resistive heating  $\mathcal{Q}_{\text{res}}$  in the metal and can be found to be [62]

$$Q_{\text{abs}} = \frac{1}{\pi r^2} \frac{2}{\sqrt{\epsilon_0/\mu_0} E_{\text{inc}}^2} \int \mathcal{Q}_{\text{res}} dV, \quad (3.40)$$

where  $E_{\text{inc}}$  is the amplitude of the incident electric field. Similarly, the scattering efficiency can be calculated as [62]

$$Q_{\text{sca}} = \frac{1}{\pi r^2} \frac{1}{E_{\text{inc}}^2 R_{\text{f}}^2} \int |\mathbf{E}_{\text{far}}|^2 R_{\text{f}}^2 d\Omega, \quad (3.41)$$

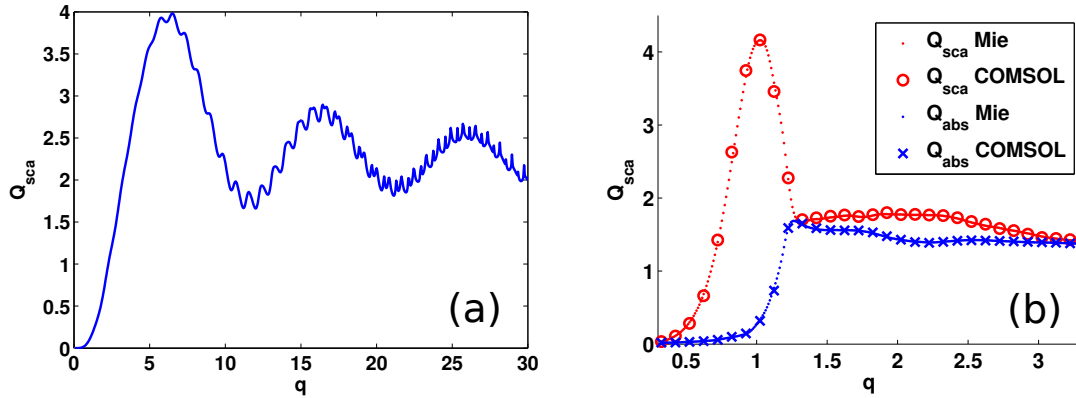


Fig. 3.5: (a) Scattering efficiency  $Q_{sca}$  of water sphere ( $n = 1.33$ ) in air; (b) Comparison of the scattering  $Q_{sca}$  and absorption  $Q_{abs}$  efficiencies for a gold sphere (radius of  $r = 100$  nm) in air calculated using Mie theory and COMSOL Multiphysics software.

where  $R_f$  is the radius of the boundary (spherical), which is used by COMSOL to calculate the far-field  $\mathbf{E}_{far}$  from the known near-field  $\mathbf{E}$  at this boundary.<sup>4</sup>

Fig. 3.5b shows the comparison of the scattering and absorption efficiencies of the gold particle with radius  $r = 100$  nm surrounded by air calculated from Mie theory and using the COMSOL Multiphysics. You can see a very good agreement between the two independent approaches. However, to achieve this level of agreement, two things have to be considered:

- mesh - things to consider include mesh symmetry at the sphere boundary, the type and minimum size of the mesh elements and the number of mesh points across the PML domain.
- the distance of the scatterer from the PML - the PML is able to absorb only the propagating field components but fails to absorb the evanescent field components. Fortunately, the evanescent fields in the proximity of the particle quickly decay. In any case, the appropriate distance for which the PML works correctly needs to be benchmarked for each particular situation.

The described validation of the model based on the comparison of the scattering and absorption efficiencies ensures the validity of the solution  $E_i$  and  $H_i$ . The fields  $E_i$  and  $H_i$  are consequently used as an input for force calculation using Eq. (3.5). The force results obtained in this way were further compared with Mie theory based results. For this, we have used a modified script based on Ref. [63] which calculates forces from Mie coefficients. The validity of both approaches was further checked

<sup>4</sup>COMSOL uses Stratton-Chu formulas to calculate the far-fields. Unfortunately, the implementation of these formulas are correct only for air ( $n = 1$ ) medium surrounding the particle (corrected in COMSOL v 4.2). Since the module responsible for calculation is not editable, one can only get the correct results in different media by utilising the self-similarity of the problem which involves simultaneous scaling of the wavelength and material constants.

in the limiting cases of very small particles (Rayleigh regime) and for very large particles (ray optics regime).

The above mentioned series of model validity checks give us a high level of confidence in the developed model. We have used this model in all subsequent simulations included in this thesis. Let us now begin with the study of optical forces near a nanoantenna.

## 3.2 Optical forces near a nanoantenna

(Part of the section reprinted from [5]. Copyright 2010 SPIE.)

We analysed a special case of a dielectric sphere of refractive index  $n = 1.5$  (glass) with a diameter of 100 nm in the proximity of the nanoantenna. This represents a typical problem in the plasmonic trapping applications. In order to get a complete information about the force field in such a case, we have to repeatedly solve the scattering problem for a series of sphere's positions. Each solution step consists of positioning the sphere at a certain point  $(x, y, z)$  in a computational domain, the scattering problem is subsequently solved and the Maxwell stress tensor method is used to calculate the forces acting on the sphere at this point.

The model was verified by comparing the FEM solution with the Mie theory in the simple case of the sphere inserted into homogeneous medium (no interface in the computational domain at this stage). The FEM model and Mie forces were compared for positions of the sphere covering the whole computational window and the maximum observed deviation from exact Mie solution was 3%. The mesh used for this comparison was the same as that used for the final solution of our nanoantenna-sphere scattering problem, however, the optical properties of nanoantenna and substrate were set to optical properties of the medium at this stage. The maximum element size of 8 nm for the Maxwell stress tensor integration boundary and 14 nm for nanoantenna boundary were found to be optimal to provide sufficient accuracy. The comparison of FEM and Mie solution revealed the necessity to move the PMLs at least  $\lambda_0/2$  from the nearest scattering object.

For reasons of numerical stability and reliability, we have also decided to limit the grid for the sphere in such a way, that the minimum distance between nanoantenna and the lowest point of the sphere is 10 nm. The resolution of a narrower region would require a very fine mesh and this, in combination with the necessity to move the PML in sufficient distance and fine coordinate grid for the positions of the sphere, would result in a computationally time and memory intensive problem, which was not possible to perform on our computer. We are aware of the fact that this is very inconvenient in terms of force field calculations as the magnitude of the force is exponentially increasing as we approach closer to nanostructure, but in terms of incident wavelength and the size of structures involved, 10 nm is just a fraction of these values and basically corresponds to the case of sphere touching the nanostructure. Further, simple extrapolation procedure seems to give very accurate predictions for the magnitude of the forces for smaller separations than 10 nm, which was tested in a special case of a sphere in a central trap. An order of magnitude

estimate of the optical forces for smaller separations can thus be obtained in this way. This type of extrapolation, however, cannot be used for a gap between sphere and nanoantenna smaller than  $\approx 1$  nm, because, at this scale, the macroscopic Maxwell's equations fail to capture the quantum mechanical behaviour of the system [64].

### 3.2.1 Case 1: normal incidence

The geometry considered is depicted on Fig. 3.6. The depicted geometry exhibits a resonant behaviour at  $\lambda_0 = 1064$  nm (Fig. 3.7). Each nanoantenna arm supports

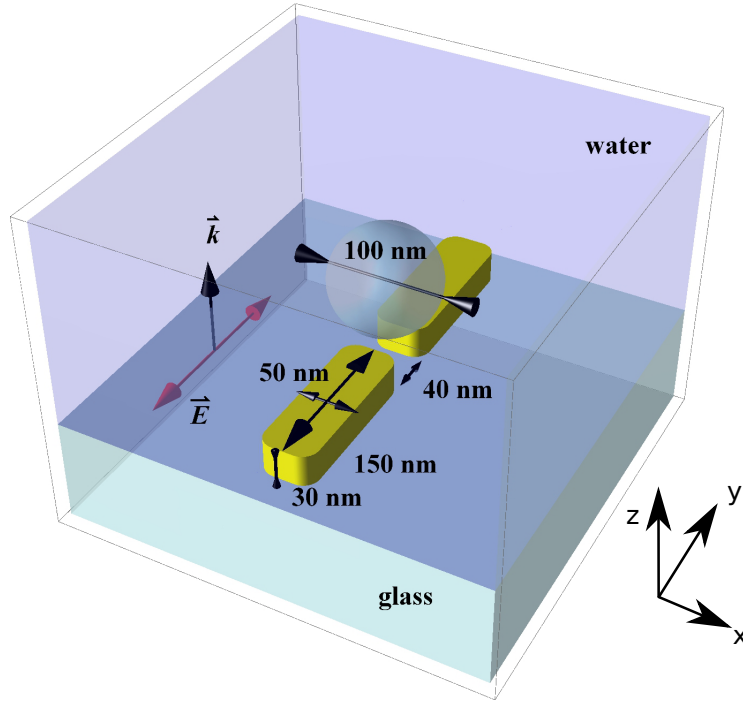


Fig. 3.6: The sketch of the geometry considered. The two yellow blocks represent the gold nanoantenna on top of the glass and submerged in water. The incident field wavevector is normal to the interface and the polarisation is parallel to the longer axis of antenna. The radius of curvature of the rounding of nanoantenna edges is 15 nm.

$\lambda_{\text{eff}}/2$  mode with  $\lambda_{\text{eff}} = 300$  nm. The effective mode wavelength is an important parameter for the efficient coupling between two antenna arms and is closely related to the field enhancement inside the gap [55]. In a nutshell, the shorter the effective wavelength of the supported mode, the larger the apparent size of the gap appears and vice versa. The apparent smaller size of the gap for large effective mode wavelengths thus improves the coupling efficiency in between the two arms of the nanoantenna, which results in better field enhancement.

One might incorrectly conclude from this, that the optimal nanoantenna design for trapping consists of very small gap and very long effective mode wavelength. This

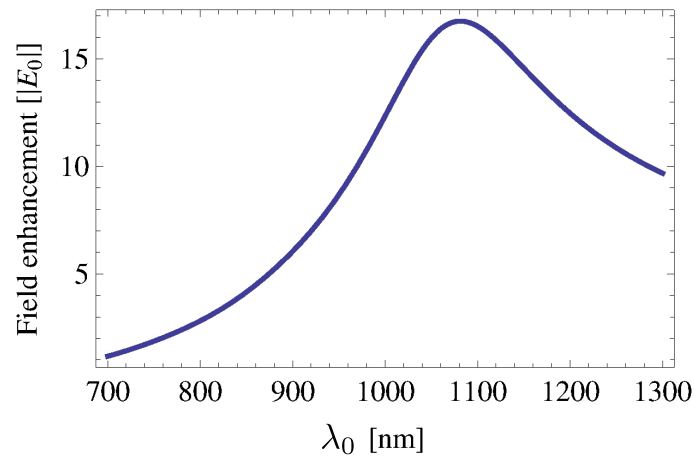


Fig. 3.7: The field enhancement factor in the middle point of the nanoantenna gap shows resonance at about  $\lambda_0 = 1064$  nm. The nanoantenna is surrounded by water with refractive index of  $n = 1.33$ .

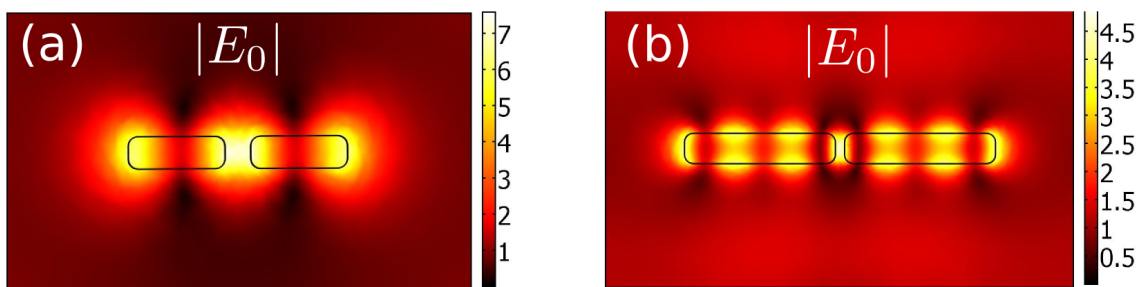


Fig. 3.8: (a) Comparison of the field enhancement profile 20 nm above (a) our nanoantenna geometry; (b) geometry presented in Ref. [4] for their respective resonant wavelengths of (a) 1064 nm and (b) 800 nm. Both nanoantennas are considered placed in a water medium lying on top of a glass substrate.

would indeed provide maximum enhancement inside the gap but a gradient of such a strongly enhanced field might not be fully accessible to the particle. For trapping purposes, we rather need to take into account the overlap of the enhanced gradient field with the volume of the particle. For example, even though the effective mode wavelength of our geometry is 150 nm with a gap size of 40 nm, the field profile 20 nm above the structure (Fig. 3.8) shows a favourable field enhancement when compared to geometry presented in Ref. [4] with effective mode wavelength of 166 nm and gap size of 30 nm. In fact, we will later see that the forces attracting the particle towards the gap are larger in our case too. This might be confusing because we said in Chapter 2 that the larger the gradient, the larger the gradient force and the second structure has slightly larger gradients in intensity. However, the treatment of the problem in Chapter 2 assumed real dipole that can "feel" the complete gradient of the intensity in a given position. In this case, however, only a small portion of the particle interacts with the strong field gradient close to the gap. The majority of the volume of the particle has insignificant contribution to light-matter interaction inducing the forces. As a result, the average field gradient that is "felt" by the whole particle can be much smaller than the maximum gradient of intensity derived from the scattering problem.<sup>5</sup>

For the very same reason, the side traps that are more accessible to the particle might, quite generally, lead to similar trapping properties when compared to gap induced traps of the nanoantenna structure. The antenna geometry presented in Ref. [4] also supports a higher order mode, which results in many hot spots in the proximity of nanoantenna. The separation of the hot spots is also not as clear as in our case, which might lead to jumps in between the neighbouring traps. For these reasons, we have decided to analyse in detail our geometry (Fig. 3.6) and provide a fair comparison with geometry presented in Ref. [4].

The field used for excitation of localised plasmon in nanoantenna is a plane wave normal incident to the antenna with polarisation parallel to the longer axis of antenna. The incident intensity in the computational domain was set to  $17 \text{ mW}/\mu\text{m}^2$ , which corresponds to the plane wave field amplitude of  $E_0 = 2.9141 \times 10^6 \text{ Vm}^{-1}$ .

The resulting force field is shown on Fig. 3.9, 3.10a and 3.10b. There are three traps, one in the center and one at each end of the nanoantenna. The magnitude of optical forces in the central and side traps is very similar and each is sufficient for optical trapping since the depth of all three traps is several  $kT$ 's (see Fig. 3.11a).

The extraction energy profile, for a dielectric sphere, along the line parallel to the longer axis of nanoantenna 10 nm above the structure also confirms the similarity of the central and side traps. This behaviour is further supported when directly comparing the trapping forces for small displacements from the stable trap position (see Fig. 3.11b, 3.12a and 3.12b). This multiple trap site feature might be very inconvenient in terms of trapping, since it seems, that there is no favourable position for trapping. This loss of control over particle position could have serious implications for applications, where immobilisation needs to be combined with specific position

---

<sup>5</sup>The effect is somehow similar to having a single toe or the whole body submerged in fast flowing river.

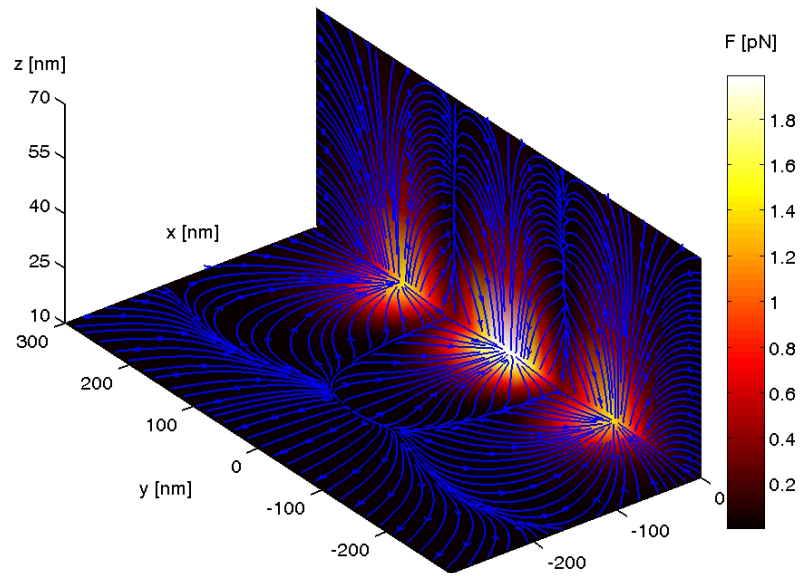


Fig. 3.9: Streamlines and magnitude of forces acting on the dielectric particle with its lowest point at distance  $z$  from the nanoantenna. Three bright spots correspond to the locations of the traps.

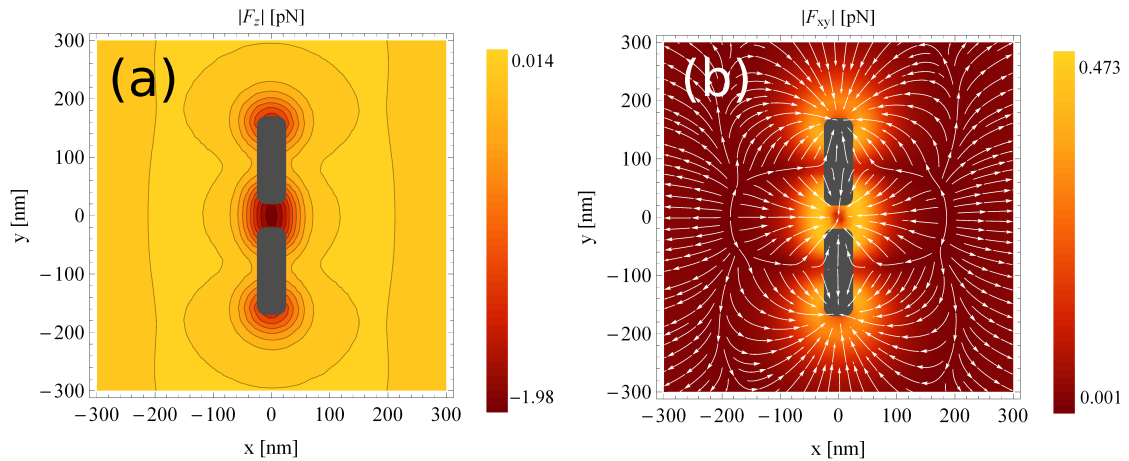


Fig. 3.10: (a) The magnitude of  $|F_z|$  and (b)  $|F_{xy}|$  with streamlines for the lowest point of sphere 10 nm from the nanostructure.

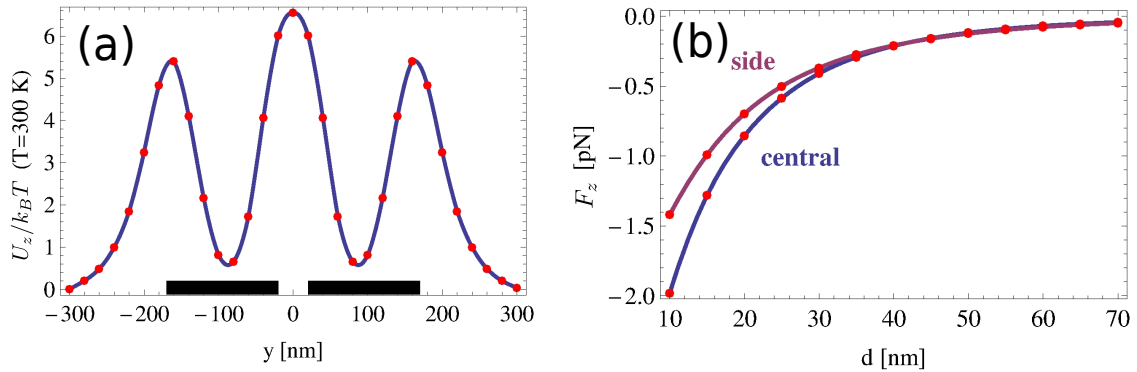


Fig. 3.11: (a) The extraction energy needed for a dielectric particle with its lowest point 10 nm above nanoantenna to be moved by 60 nm in the  $z$ -direction, where the antenna induced forces become negligible. Traps are in the positions of the maxima of the extraction energy profile. (b) Vertical force acting on the sphere in central trap and side traps as a function of the distance of the sphere's lowest point from nanoantenna. The negative sign of the force corresponds to the force pointing down towards the nanoantenna. The bars on the axis denote the extent of the nanoantenna.

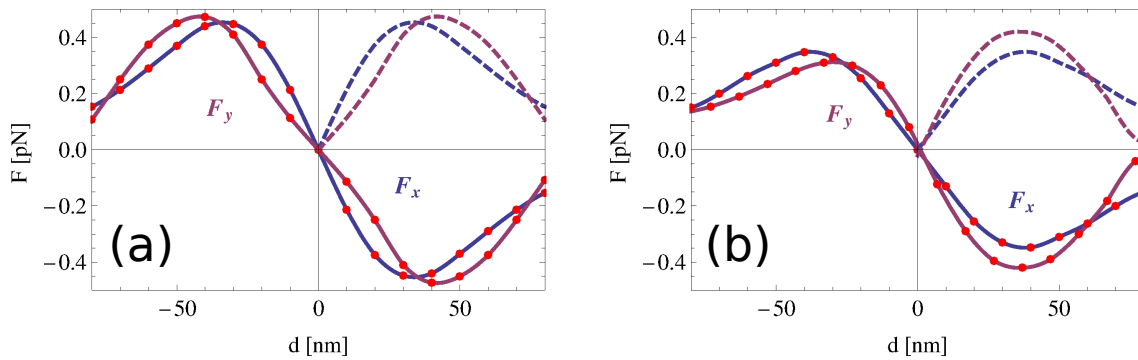


Fig. 3.12: Lateral forces acting on a dielectric sphere with its lowest point 10 nm above the structure in (a) central and (b) side traps, where  $d$  is the displacement from the center of the trap. The dashed line is the reflection of the graph around horizontal axis for  $d > 0$ , which allows easier assessment of the symmetry or asymmetry of the lateral forces.

in the enhanced field around nanostructures as is the case for Surface Enhanced Raman Spectroscopy. We would argue that this multiple trap character, given by underlying mode profile, is one of the major drawbacks of plasmonic trapping. On one hand, we can localise the particles in a very small volume. On the other hand, we do not know in which of the traps the particle actually resides.

### 3.2.2 Case 2: total internal reflection incidence

We have seen in the previous section, that the central and side traps are very similar. In this section we want to determine the effect of varying the angle of the incident plane wave upon the nanoantenna on the trapping sites. One case that we study in detail is the total internal reflection at critical angle shown in Fig. 3.13. This

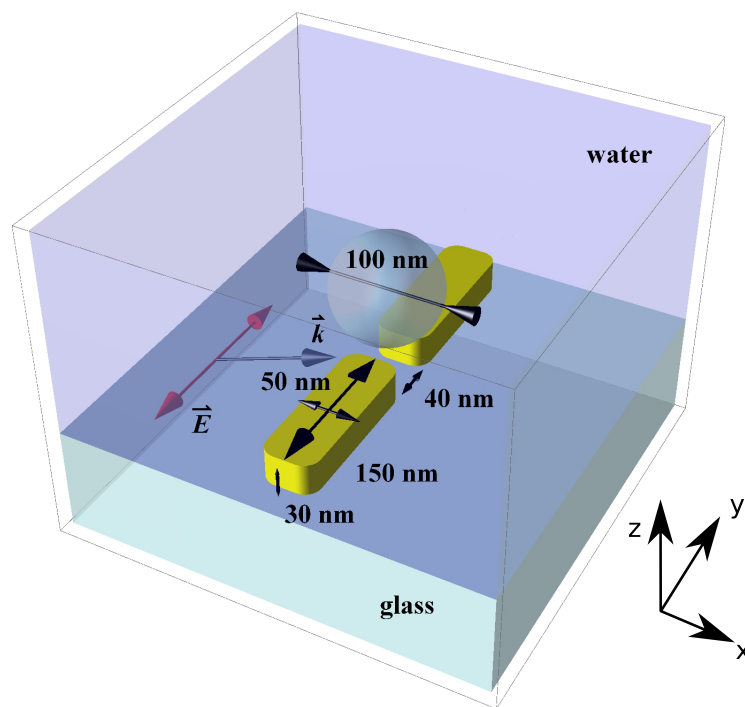


Fig. 3.13: Total internal reflection incidence, polarisation parallel to the longer axis of antenna.

also corresponds to the experimental realisation presented in Ref. [4]. However, the TIR configuration can be quite cumbersome and complex because specialist optical elements need to be used and it is therefore reasonable to ask whether this approach brings some significant advantages over the case of normal incidence.

We first modelled the  $z$ -forces acting on the particle in central and side traps for the lowest point of sphere 10 nm above the nanoantenna as a function of incident angle of the plane wave (Fig. 3.14a). The results clearly show that the optimal angle maximising the force is the critical angle. The angle dependence of force is closely resembling the intensity dependence on angle at the interface of two semi-

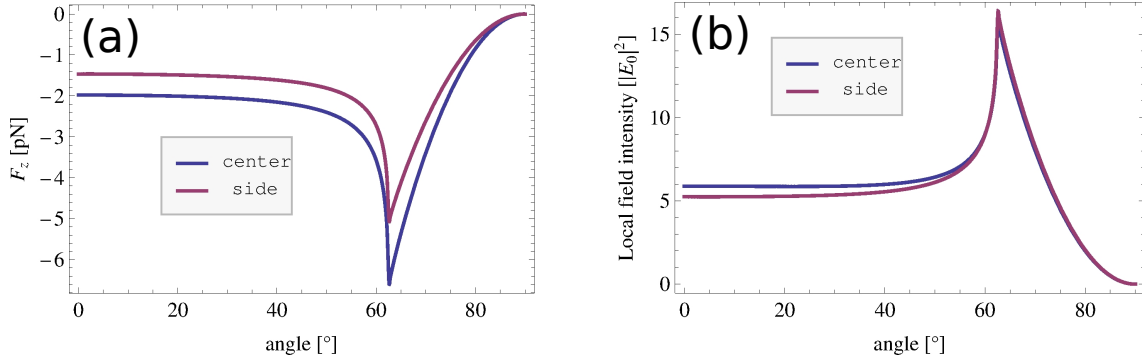


Fig. 3.14: (a) The  $F_z$  force as a function of incident angle in the central and side traps for a lowest point of sphere 10 nm above the nanoantenna. (b) The local field intensity inside the particle normalised to  $E_0 = 2.9141 \times 10^6 \text{ Vm}^{-1}$  averaged over the volume of the particle positioned in central and side traps.

infinite media (derivation of this effect can be found in Ref. [52] on page 9). As the intensity at the interface is proportional to the effective intensity driving the localised plasmons, the net result is also a much higher local field (Fig. 3.14b) in the proximity of the nanoantenna. This local field reaches its maximum for critical angle. The increase in the intensity of local fields is then further projected into increased forces acting on the particle reaching the maximum for the critical angle.

However, the common goal of all optical trapping experiments is to maximise the trapping force and, at the same time, minimise the local fields interacting with the particle. Since the damage threshold of the trapped particles or living cells is not affected by global field intensity, but rather by local field intensity, the question arises whether the increase in optical force for TIR incidence is not just equivalent to increase of local field intensity, which can be easily achieved in normal incidence by simply increasing the global intensity of the laser. Fig. 3.14b actually shows that the force  $F_z$  and the local field intensity (normalised to  $E_0 = 2.9141 \times 10^6 \text{ Vm}^{-1}$ ) averaged over the volume of the particle are increased by roughly the same factor. Thus, although the forces might seem to be optimised for the critical angle, the same angle gives highest optical fields inside the particle.

The more appropriate description of the efficiency of the trap is to directly relate local field intensity inside the particle, which drives the strength of light-matter interaction, to forces acting on the particle. We therefore looked at the dependence of force as a function of local field intensity averaged over the volume of the particle for the cases of normal incidence and TIR incidence at the critical angle (Fig. 3.15). The improvement in trapping efficiency by using TIR incidence as opposed to the normal incidence, determined from the ratio of the slopes in Fig. 3.15a, is 23%. On the other hand, the heat generation rate in nanoantenna, calculated from volume integral of time-averaged resistive heating in our model, is 28% higher for a given local field intensity in the particle for TIR illumination compared to the normal incidence case (Fig. 3.15b). This could completely cancel the 23% gain in magnitude

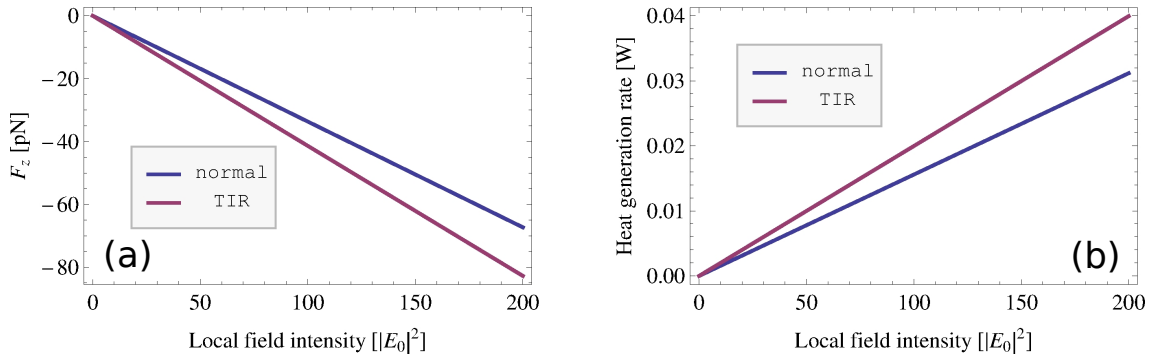


Fig. 3.15: (a) The  $F_z$  force as a function of local field intensity averaged over the volume of the particle shows slight improvement (23 %) in trapping efficiency for the TIR illumination. (b) The heat generation rate in nanoantenna negatively affecting the thermal dynamics in the proximity of nanoantenna is slightly worse (28 % higher) for the case of TIR illumination.

of forces because the heat is dissipated not only by conduction but by convection as well. The issue of convective heating is discussed in more detail in the following section.

The TIR incidence thus does not provide any particular advantage over normal incidence case from the point of view of forces normalised in a way to reflect the efficiency of trapping. To achieve the same magnitude of force, roughly the same local field intensity inside the particle is observed for both illumination cases. In addition, the TIR critical angle incidence further introduces asymmetries to the trapping sites (Fig. 3.16 and Fig. 3.17), which might further decrease the performance of the nanoantenna structure. As can be seen on Fig. 3.17, the TIR case significantly breaks the symmetry of lateral forces in central trap, but on the other hand, the symmetry of the side traps is surprisingly improved compared to the case of normal incidence.

The extraction energy profile and the  $z$ -force dependence (Fig. 3.18) for central and side traps clearly shows the equivalence of central and side traps even for TIR illumination, which further supports our conclusion that no preferred trap position exists near a nanoantenna and that, with this geometry, nanoparticles will be basically randomly trapped in either one of the three similar traps.

We can conclude, that TIR does not offer any significant advantages over the normal incidence case and the beam delivery system could thus be simplified by adopting normal incidence excitation in experiments.

### 3.2.3 Comparison of the two nanoantenna geometries

For a comparison of the trapping performance of our nanostructure with respect to the nanostructure presented in Ref. [4], we performed numerical simulation of the extraction energy profile for an experimental situation described in Ref. [4], which

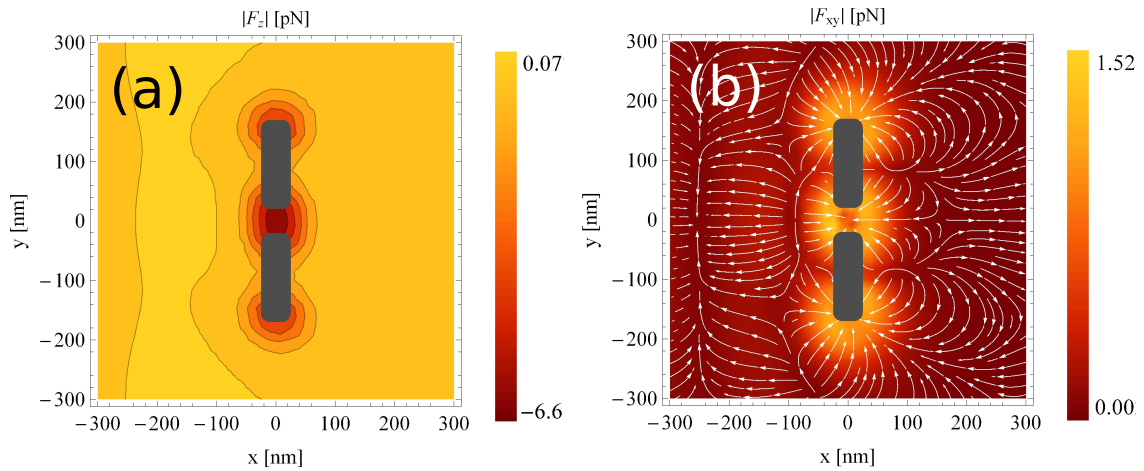


Fig. 3.16: (a) The magnitude of  $|F_z|$  and (b)  $|F_{xy}|$  with streamlines for the lowest point of sphere 10 nm from the nanostructure. Notice, that the symmetry of the problem is broken. The incident plane wave is incident at critical angle from the left.

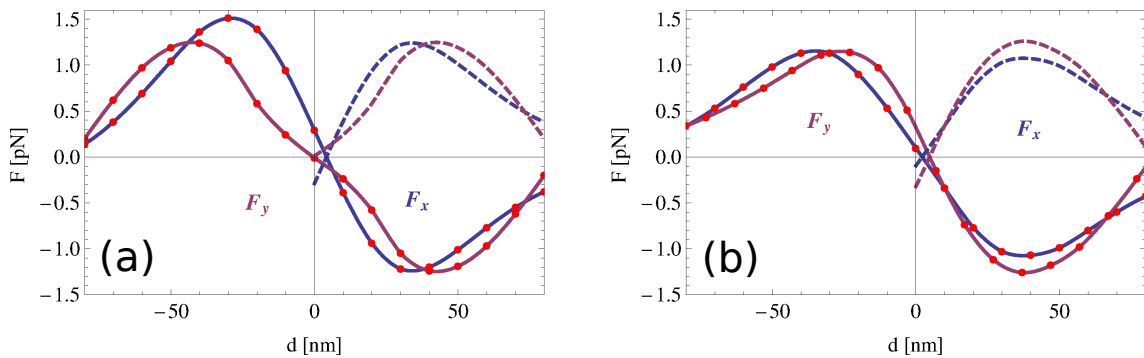


Fig. 3.17: The lateral forces, for critical angle incidence, acting on a dielectric sphere with its lowest point 10 nm above the structure in (a) central and (b) side traps, where  $d$  is the displacement from the center of the trap in normal incidence case. The dashed line is again the reflection of the graph around horizontal axis for  $d > 0$ , which allows easier assessment of the symmetry or asymmetry of the lateral forces.

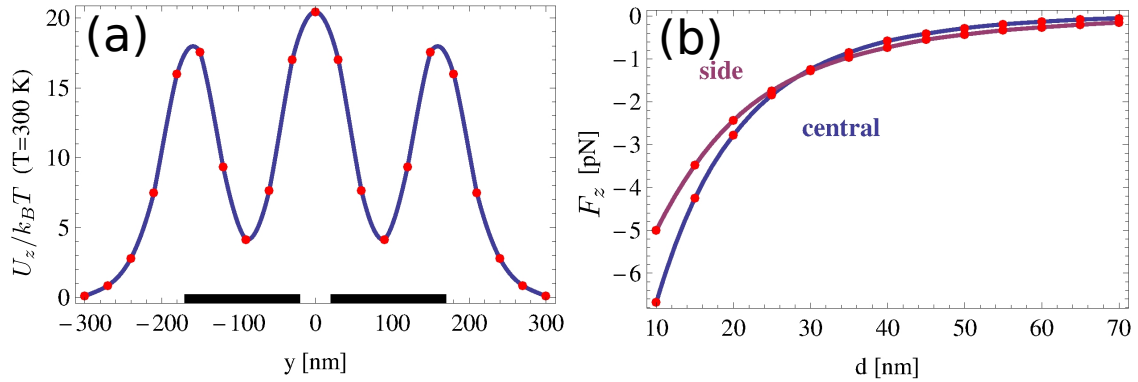


Fig. 3.18: (a) The extraction energy needed for a dielectric particle with its lowest point 10 nm above nanoantenna to be moved by 60 nm in the  $z$ -direction for critical angle incidence. Antenna induced forces became negligible at this point. (b) Vertical force acting on the sphere in central trap and side traps as a function of the distance of the sphere's lowest point from nanoantenna for critical angle incidence. The bars on the axis denote the extent of the nanoantenna.

means trapping of 200 nm polystyrene beads at TIR incidence (we assumed critical angle incidence as the angle of incidence was not specified in the paper). To be able to compare the trapping performance, the incident intensity used for simulations was set again to  $17 \text{ mW}/\mu\text{m}^2$ . Since the attractive forces induced by this type of antenna are reversed to repulsive quite close to the antenna structure, we took as a measure of extraction energy the energy needed to move the bead from its initial position to the position, where the force was zero.

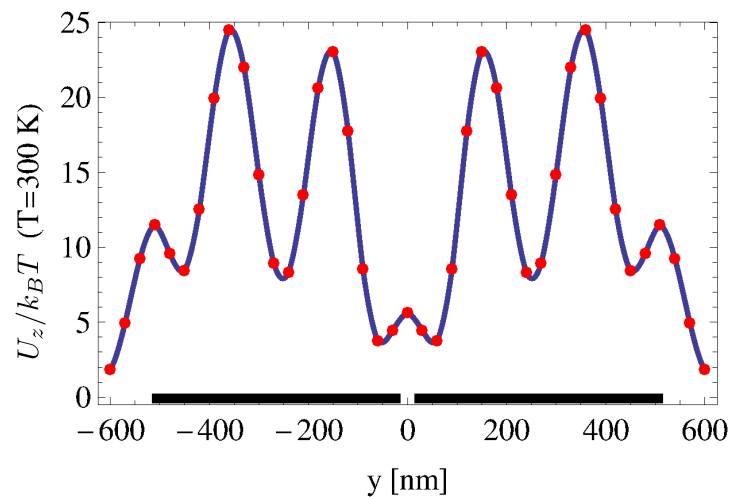


Fig. 3.19: The extraction energy profile for the geometry presented in Ref. [4] in the case of 200 nm polystyrene bead. The bars on the axis denote the extent of the nanoantenna.

The extraction energy profile (Fig. 3.19) clearly shows that the trapping properties in terms of the absolute depth of the potential well are almost the same for both types of antennas. However, the structure supports even more trapping sites (consequence of the higher order mode supported by the nanoantenna), with not as clear boundaries as in the case of our structure. The most efficient trapping appears to be in the second hot spot away from the centre of the gap, which is in good agreement with the simulations presented in Ref. [4]. Also notice that the centre trap is quite weak, which is a demonstration of the lack of overlap between the enhanced field in the gap and the geometry of the particle. When we further realise that the reference particles are twice as big in Ref. [4] case than in our case and that the gradient forces attracting the particles to the hot spots scale down with the volume of the particles, we can conclude that our structure has similar or even slightly better trapping properties than the structure presented in Ref. [4].

### 3.2.4 Heating issues

The heating effect in metallic nanostructures is intrinsically related to the amount of incident intensity. As we wish to compare the plasmonic tweezers to conventional optical tweezers, we used  $17 \text{ mW}/\mu\text{m}^2$  as incident intensity corresponding to a realistic value for conventional tweezing. This incident intensity is also of the same order of magnitude as the one used in [34] demonstrating plasmonic trapping. Neglecting the thermal effects, the optical force scales linearly with the incident power and as such it is easy to deduce these forces for any illumination power.

From the thermal point of view, an incident power of  $17 \text{ mW}/\mu\text{m}^2$  corresponds to a heat generation rate of about  $1.5 \text{ mW}$  in one antenna arm (at critical angle incidence). This value was calculated from the resistive losses integrated over the volume of the antenna arm using the Comsol Multiphysics model and verified by comparing the power outflow from the computational domain with and without the scatterer included. Taking into account the size of the antenna and the thermal conductivity of the surrounding media, this would roughly imply, according to Ref. [65], a local temperature increase above the boiling point of water. This could lead to bubble formation and very strong hydrodynamic effects disrupting the trapped particle.

The thermally induced effect was also discussed in Ref. [4] where they estimated a temperature change of  $1 \text{ K}$  on the surface of the metal for their antenna geometry. To achieve such a small temperature change they decreased the incident intensity to about  $40 \mu\text{W}/\mu\text{m}^2$  in their experiment. However, according to our calculations such a low incident intensity makes the absolute trap depth about three orders of magnitude smaller than the one presented in this chapter. This renders the optical trap so weak (fraction of  $k_B T$ ) that no optical trapping should be observed. Since large scale aggregation of colloid on a surface has also been reported due to the effects of thermophoresis and convection [36] and the same non-optical mechanisms were even used for trapping of  $200 \text{ nm}$  polystyrene beads [66], we believe that the observed localisation of particles may have been due to means other than the optical forces.

The limitation of the gap size, between particle and nanoantenna, to 10 nm could not be responsible for the bulk of the change. Using extrapolation, we might estimate that accounting for points closer to nanoantenna, we would increase the extraction energy by about 20%. This still leaves extraction energy values at a fraction of  $k_B T$ .

Another possible explanation might be due to surface roughness of the fabricated structure. This can possibly increase the local gradients of intensity by a significant amount and allow for values of  $k_B T$  that are sufficient for stable trapping. Furthermore, some form of chemical binding or other form of surface forces should be also considered as a potential source of the observed trapping effect.

### 3.3 Attempts to differentiate heating and optical effects

In the course of my PhD, I have used the design of antennas (Fig. 3.20) analysed in

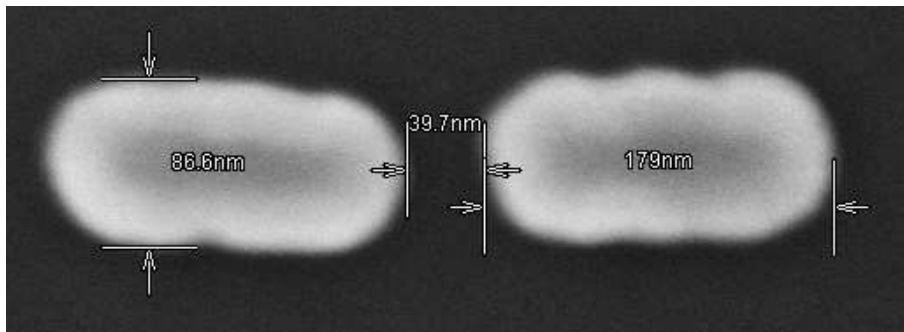


Fig. 3.20: The scanning electron microscope (SEM) image of the antenna design used for our experimental trapping configuration. (Special thanks to Andrea Di Falco who fabricated the nanoantennas and took the SEM images.)

this chapter and never observed any trapping event for low intensities. Increasing the intensity above few  $\text{mW}/\mu\text{m}^2$  always resulted in strong thermal dynamics and bubble formation. Sporadically, I have observed some localisation of particles, but the localisation effect was maintained after switching off the laser, which excludes the possibility of optically induced trap. Similar behaviour was observed by Wang et. al. [6] in the case of gold nanopillars. They solved the problem of heating by fabricating the nanopillar on top of a gold and copper layer, which served as a heat-sink. In this way, they were able to increase the incident intensity sufficiently high to observe trapping and even rotation of particles as small as 110 nm in diameter. We believe that the research presented in Ref. [6] represents one of the most significant steps in plasmonic trapping so far and provides a working nanotweezer based on the plasmon resonance.

Except for the research of Wang et. al [6], the performance of all other plasmonic trapping designs such as, for example, trapping in nanoholes [35, 37, 39, 40] is still hindered by heating. Before the research of Wang et. al. [6] was presented, we have attempted to experimentally differentiate the effects of optical forces and heating around plasmonic nanoantennas. The prime candidate, at the time, for the observed

trapping were the heating induced convective currents. But it was often claimed, without any evidence, that the heating cannot be responsible for trapping because the heating "hot-spots" appear at different locations than the field intensity "hot-spots". This is indeed correct (Fig. 3.21), however the heat distribution inside the

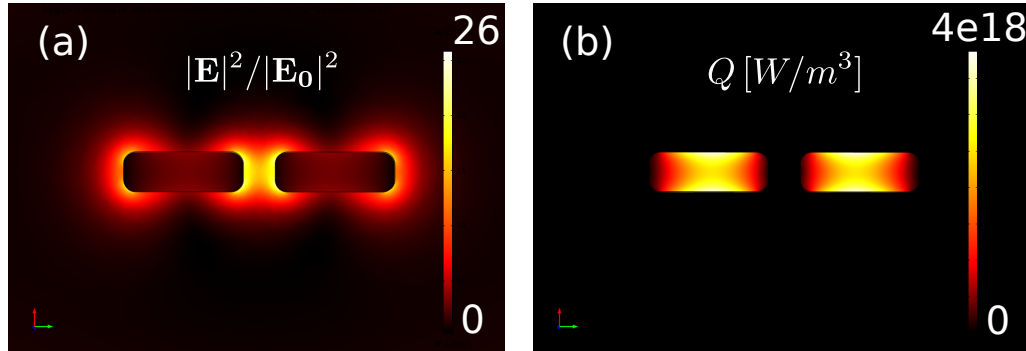


Fig. 3.21: The top view of a nanoantenna for (a) field intensity and (b) heating (heating obtained from resistive losses due to current density calculated in COMSOL model). The "hot-spots" appear in intrinsically different places.

metal actually supports the idea that the convection currents might be responsible for trapping (Fig. 3.22). Based on this qualitative evidence, we have decided to

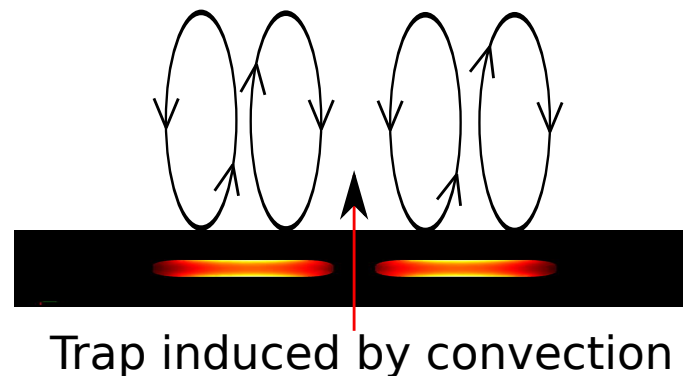


Fig. 3.22: The two antenna arms serve as the heating centres that induce a convection current. The flow of fluid points towards the central gap of antenna. This suggests that the heating induced convection might be responsible for optical trapping near nanoantenna.

experimentally separate the effects of heating and optical forces.

The idea was based on the fact that the heating and optical effects have different decay times in the system when the laser is switched off. While the optical effects disappear on the order of nanoseconds, the heating induced effects can exist as long as microseconds or even milliseconds. This means that the movement of the particle around nanoantenna, immediately after the laser is switched off, is dominated by

heating in the system. Repeatedly switching off the laser and tracking the position and velocity of the particle around nanoantenna, right after the laser is switched off, reveals the contribution of heating effects to the movement of the particle. Tracking the motion of the particle with laser switched on reveals, in a similar way, the net effect of both - the optical forces and heating effects in the system. This approach leads to two velocity maps of a particle around nanoantenna - first velocity map represents the velocity of the particle induced by heat; the second velocity map then represents the velocity of the particle induced by combined effects of optical forces and heating. Subtracting the second map from the first then leads to a velocity map representing the effects of optical forces alone.

To verify this concept, we have designed the tracking algorithm in LabView (interface depicted in Fig. 3.23) capable of tracking the particles in 3D with nanometre

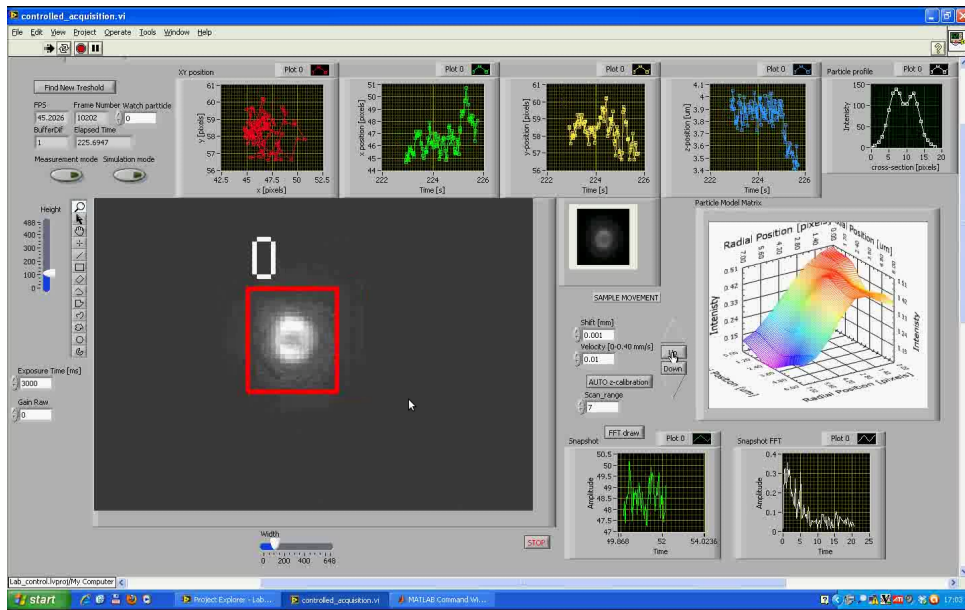


Fig. 3.23: The interface of the particle tracking algorithm developed in LabView. The algorithm is capable of tracking nanoparticles with resolution of 5 nm in xy-plane (based on minimum variance central thresholding [67]) and with resolution of 20 nm in z-plane (based on off-focus image calibration [68]). The particles were tracked in dark-field. The scattering from nanoantenna is progressively suppressed by the algorithm.

precision. However, the project encountered several problems. First of all, as already stated, the trapping of particles near a nanoantenna was never actually observed for our experimental configuration which precluded any sensible construction of the maps. Furthermore, we could not really suppress the background of the nanoantenna while tracking the particle. This was partially due to continuous drift of the setup but also due to interference of the particle and the nanoantenna images. This inability to suppress the nanoantenna background introduced significant and rather

random systematic errors to a position of the tracked nanoparticles. Due to the above complications we have decided to abandon the project even though we think that the resolution of the heating contribution to trapping is a very interesting area to study.

### 3.4 Conclusion

In this chapter, we have concluded that the total internal reflection does not provide any particular advantage over normal incidence excitation in terms of near-field enhancement and the corresponding near-field optical forces. However, we note that the normal incidence excitation might hinder the approach of particles to the near-field zone of the nanoantenna due to the presence of non-negligible scattering force. This would push the particles away from the nanoantenna. As such the critical angle incidence is a more practical approach. However, we would also like to note that the near-field forces of antenna geometry in Ref. [4] become repulsive quite close to antenna structure and this might also hinder the approach to near-field zone.

Our calculations also showed that the incident intensity used for excitation of nanoantennas in Ref. [4] is not sufficient for optical trapping. The presented incident intensity makes the absolute trap depth about three orders of magnitude smaller than the one presented in this chapter. This renders the optical trap so weak (fraction of  $k_B T$ ) that no optical trapping should be observed. Since large scale aggregation of colloid on a surface has also been reported due to the effects of thermophoresis and convection [36] and the same non-optical mechanisms were even used for trapping of 200 nm polystyrene beads [66], we believe that the observed localisation of particles may have been due to means other than the optical forces. We have attempted to differentiate the optical and the heating induced forces experimentally, however, our experiments met technical difficulties. We do believe, however, that this topic deserves further experimental attention.

To summarise, we anticipate that the exciting and complex interplay between electromagnetism, thermodynamics and mechanics in plasmonic tweezing applications will maintain a high level of research interest in this area for years to come.

Let us now turn our attention to another major application of plasmon resonance in the field of optical manipulation, that does not directly utilise the strong field confinement, but rather the dependence of resonant effect on the particle size.

## Chapter 4

# Plasmon resonances in optical sorting <sup>1</sup>

We have seen, in Chapter 1, a qualitative proof that the localised plasmon resonance of the spherical particle should red-shift with increasing particle size. However, the quasi-static calculations of the localised plasmon mode of a sphere in Chapter 2 did not exhibit any such shift of plasmon resonance peak for increasing particle size. This failure of the quasi-static approach to capture the red shift of the resonance suggests that retardation effects must play some role.

There are two possible effects when we relax the quasi-static approximation. Firstly, the phase of the electromagnetic field across the volume of the nanoparticle is not constant any more. Consequently, this leads to the onset of higher order modes supported by particle. Secondly, the average separation of the charges generated by dipole mode and higher order modes will increase with increasing particles size. Intuitively, one would think that the larger distance between charges implies smaller Coulomb interaction and related restoring force. In fact, we have used this simplified argument in Chapter 1 to point out to the existence of the resonance red-shift. Unfortunately, the situation is not as simple. For example, the applied external field, in fact, displaces more charges in larger spheres and as a result, we cannot use the simple argumentation based on restoring Coulomb force. However, we might consider the following situation. Imagine we generate a charge density change on one side of the particle. Due to retardation, the reaction on the opposite side of the particle, for dipole mode, will have a phase delay on the order of<sup>2</sup>

$$\varphi \propto \frac{2\pi}{\lambda}(2r), \quad (4.1)$$

from which we can easily see that the phase delay increases for larger particle sizes. As a result, it takes much longer for the changes to take effect in larger particles.

---

<sup>1</sup>A significant portion of this chapter was reprinted with permission from [M. Ploschner et. al., Nano Letters, 12(4):1923-7,2012] [69]. Copyright 2012 American Chemical Society. To access the final edited and published work see <http://pubs.acs.org/articlesonrequest/AOR-dn2q4qYvn8rHSYqrSn8K>

<sup>2</sup>The higher order modes will have the phase delay slightly lower because the average distance of the charges is smaller. [70]

This can be equivalently viewed as if the time runs effectively slower, which finally implies the lower frequency of the mode for increasing particle size.

All the above described effects can be easily accounted for by using the rigorous Mie solution. The position of the resonance peak can be calculated from the extinction efficiency  $C_{\text{ext}}$  which is given by Eq. (3.35). The resulting extinction efficiency profile for 100, 130 and 150 nm gold nanoparticles is depicted in Fig. 4.1 and

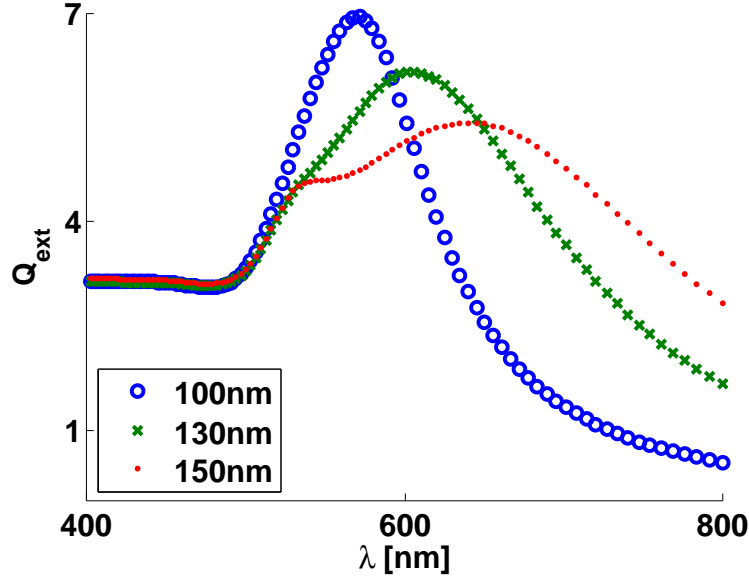


Fig. 4.1: The extinction efficiency of gold nanoparticles (in water) with diameter of 100, 130 and 150 nm shows a clear redshift of the resonance peak for increasing particle size. The figure also shows the onset of quadrupole mode for the particle with diameter of 150 nm.

shows a clear redshift of the dipole resonance peak for increasing particle size. As the extinction efficiency is proportional to the push force  $F_{\text{push}}$ , given by Eq. (2.4), we can expect that the push force exerted on gold nanoparticles will depend very strongly on the excitation wavelength. This opens up a new window for sorting gold nanoparticles by size.<sup>3</sup> The results, exploiting the red-shift of resonance for optical sorting, presented in this chapter were recently published in Ref. [69].

#### 4.1 Why does the size of a nanoparticle matter?

Gold nanoparticles have unique optical and chemical properties. We have just seen that their optical properties are strongly influenced by their plasmon resonances, associated with the collective excitation of conduction electrons, which in turn is dictated by the particle geometry. Further, their chemical properties allow for diverse functionalisation options. For these reasons, gold nanoparticles have emerged

<sup>3</sup>Similar approach is applicable to any particle (e.g. silver) that exhibits shift of plasmon resonance peak for changing particle size.

as ideal candidates for an exceptionally wide range of biomedical applications [71]. They are commonly employed for Surface Enhanced Raman Spectroscopy (SERS) and as fluorescence enhancers in various applications - e.g. intracellular biochemical composition imaging [72], DNA and RNA detection [73] and tumor targeting [74]. Additionally, they are used as mechanical carriers through cell membranes for DNA and drug delivery [75] and as localised heaters for photothermal therapy [76]. Crucially, gold nanoparticles show immense promise for multimodal biomedical applications [77] - e.g. mechanical delivery with subsequent biochemical sensing and imaging. In all these cases, the physical shape and size of the gold nanoparticles dictate their performance. For example, size is a crucial parameter for the cell uptake rate of gold nanoparticles as mechanical carriers [78, 79], the intensity of a SERS signal [80, 81], the biochemical [82], optical [83] and toxicity [84] properties of nanoparticles. It is thus necessary to tailor this parameter to a high degree of accuracy for each specific application. This results in a burgeoning need for size selective controlled separation and manipulation of gold nanoparticles in solution.

## 4.2 Methods for sorting nanoparticles by size

Various chemical synthesis methods [85–87] yield gold nanoparticles of different sizes, within a range from 2 nm to 200 nm and a typical polydispersity of at least 10%. The scaling of the synthesised volume can be complicated as vigorous stirring of reducing agent and homogeneous temperature is necessary for obtaining an acceptably low level of polydispersity and the optimal conditions for this change abruptly with volume. Various post-synthetic sorting methods such as sedimentation [88] or centrifugation [89] have been developed, however their dynamic range of sorting may be limited. On the other hand, purely optical based sorting or selection methods [90–95] have the potential to sort or fractionate nanoparticles over a wide range of particle sizes in a sterile manner with exceptional sensitivity and show excellent compatibility with microfluidic environments.

Two main optical sorting approaches exist – namely *active* and *passive*. Active sorting techniques use fluorescent signals [96], optical switches [97, 98] and real-time computation [99, 100] for particle recognition that then subsequently acts as a trigger for another part of the system where optical (or other) forces are used to separate particles of different properties into separate streams. However, the need to use a trigger may add complexity and be impractical in many instances. For this reason, the last decade has seen the emergence of passive sorting methods which rely entirely on the different physical response of various particles to an extended optical field, commonly referred to as an optical potential energy landscape. Such passive sorting offers exceptional size and refractive index sensitivity [91, 92] and has been demonstrated in a number of geometries both with and without the presence of microfluidic flow. In microfluidic type sorting, laminar fluid flow perpendicular to the optical forces is employed and the separation of particles is either realised solely by scattering force differences [95] in aperiodic optical patterns or by means of structured light fields [92, 93, 101–104] creating periodical optical potential energy

landscapes.

Optical sorting of dielectric particles in the absence of flow has been realised by means of translating near-field evanescent wave interference patterns [10, 105], with far-field interference patterns [106], Bessel modes [107] and proposed within an optical conveyor belt created with a dual beam photonic crystal fiber system [108]. However, metal nanoparticles, and particularly their resonant effects, have not been appropriately considered nor exploited for any form of experimental optical sorting. To date, optical sorting realisations have mainly focused on dielectric particles or cells, largely at the micron size scale with only a few theoretical studies [109, 110] exploring the possibility to extend the range of this powerful method to the case of plasmonic nanoparticles such as gold and silver. And since the optical forces acting on metallic nanoparticles vary significantly with particle properties such as size and composition, particularly when close to plasmon resonance conditions, there is an opportunity for optical sorting utilising this behaviour. Furthermore, such a method, based on resonant behaviour related strongly to particle size, has a promise to deliver better resolution of the sizes simply because of the utilisation of intrinsic resonant property. This might be a major advantage over methods such as sedimentation or centrifugation that rely solely on the differentiation of the actual geometrical size.

For a quantitative comparison of the sorting methods and their limitations please see Tab. 4.1.

Method	Material	Size	Resolution	Limitation
sieving	general	$> 2 \mu\text{m}$	determined by the sieve quality	metal rectangular sieves have large openings
sedimentation in microfluidic channel	general	$> 1 \mu\text{m}$	10% of the particle size	low throughput
periodic optical landscape [92]	dielectric/ metallic?	$\approx 1 \mu\text{m}$	$\approx 20 \text{ nm}$	low throughput
motional standing wave [10]	dielectric/ metallic?	$> 350 \text{ nm}$	$\approx 60 \text{ nm}$	shallow trap depth for smaller particles
our method	metallic	$\approx 100 \text{ nm}$	$\approx 30 \text{ nm}$ ; theoretical limit $< 5\%$ of the size	shallow trap depth; shape variation of particles

Tab. 4.1: The summary and the quantitative comparison of the particle sorting methods. The data for sieving method taken from state of the art manufacturer IndustrialNetting. The data for sedimentation based sorting are based on the state of the art commercial device SPLITT from PostNova.

### 4.3 Bidirectional sorting of gold nanoparticles

In this section, we present the experimental demonstration of size selective bidirectional optical sorting of gold nanoparticles using a dual wavelength counter-propagating evanescent wave geometry (Figure 4.2). Our technique is based on

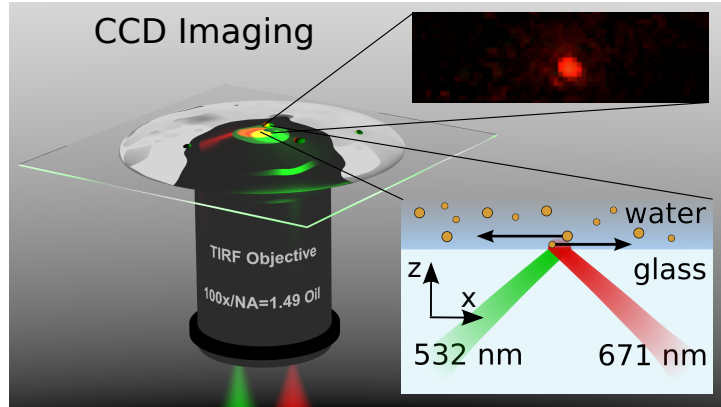


Fig. 4.2: Two Gaussian beams with wavelengths of  $\lambda = 532$  nm and  $\lambda = 671$  nm respectively are focused to the opposite edges of the back-focal plane of a total internal reflection fluorescence (TIRF) objective (Nikon NA=1.49, 100 $\times$ ). The beams propagate at the critical angle to the interface, where the counter-propagating evanescent field is generated. This both attracts the particles towards the substrate and guides them in the  $\pm x$ -direction. The balance of the forces from the two lasers is such that the particles of different diameter move in the opposite directions. The evanescent field scattered by particle into far-field is used for CCD imaging. The imaged particle appears red as part of the scattered field corresponding to  $\lambda = 532$  nm is filtered.

the above described redshift of the plasmon resonance with increasing particle size. As a result, smaller nanoparticles predominantly interact with shorter wavelengths whereas larger nanoparticles are mainly influenced by longer wavelengths (Figure 4.4a). Selecting the optimal wavelengths and power ratio between the counter-propagating beams we generate a force field within the illuminated region that guides nanoparticles of different sizes in opposite directions to one another, thus realising sorting. The presented configuration extends optical sorting methods to the distinct case of plasmonic nanoparticles and size scales typically one order of magnitude lower than previously realised with dielectric objects [10, 105–108]. We chose a near-field evanescent wave method for our experimental realisation as it offers both the ability to sort over extended area and enables particle confinement close to an interface [10, 111]. The near-field method also allows for simple particle detection and identification during sorting as the particles are basically confined in a single plane. This confinement removes problems with particle defocusing which would emerge in configuration of two loosely focused beams realising the sorting in the whole volume of the chamber. As the real-time detection and identification of the particles

constitutes a very useful feature of our method, especially when considering that the identified sorted particle may be utilised in situ, we believe, that the near-field configuration is more useful than the loosely focused beam configuration which requires an offline identification of the sorted ensemble using the scanning electron microscope (SEM). The bidirectional character of sorting is also a useful feature. Firstly, it allows for much clearer interpretation of sorting. Unidirectional sorting would push particles of different sizes at different speeds, but such an experimental realisation might be prone to preferred particle trajectories (certain heights in the evanescent field) which might have a similar effect on the particle velocity. This is not likely to happen in the bidirectional scheme given that the two beams overlap and their incident angle is the same. Secondly, the particle delivery in one direction has very limited range of applications as the sorted ensembles in the end arrive to the same position (with some time delay).

### 4.3.1 Selection of operating wavelengths

Due to the presence of the plasmon resonance, the force profile, as a function of particle size, will differ significantly for various wavelengths. In order to efficiently differentiate particles of two sizes in bidirectional scheme, we require a combination of both a flat and a steep gradient of the force profile since the subtraction of two flat or two step profiles never generates size regions strongly dominated by one wavelength. The selection of appropriate wavelengths is thus crucial.

Our experimental realisation uses two wavelengths ( $\lambda = 532$  nm and  $\lambda = 671$  nm) with very distinct gradient of optical force profile in selected interval of particle sizes. We have used the following steps to find the ideal operating wavelengths.

First, the average growth rate  $\alpha$  of the optical force  $F \sim d^\alpha$  was estimated in the interval of interest ( $d = 80$  nm to  $d = 160$  nm) for different wavelengths. This was performed using the ratio of forces at the respective limits of the interval ( $d_1 = 160$  nm and  $d_2 = 80$  nm):

$$\frac{F_{d_1}}{F_{d_2}} \sim \left(\frac{d_1}{d_2}\right)^\alpha = 2^\alpha \quad \rightarrow \quad \alpha \sim \log_2 \left(\frac{F_{d_1}}{F_{d_2}}\right). \quad (4.2)$$

Fig. 4.3a shows that  $\alpha$  exhibits large variation with wavelength. The minimum of  $\alpha$  is close to  $\lambda = 532$  nm. The maximum converges asymptotically to  $\alpha \approx 6$  which is a limit of Rayleigh scattering cross-section in the case of low absorption. Please note that we deliberately chose the ratio of forces at the limits of the interval rather than the standard gradient definition of  $(F_{d_1} - F_{d_2})/(d_1 - d_2)$ . The reason may be understood from Fig. 4.3b. Here, we can see that the average gradient in interval, at  $\lambda = 1064$  nm, is smaller than both the gradient at  $\lambda = 532$  nm and  $\lambda = 671$  nm in the interval (for the same incident intensity). However, scaling up the power for  $\lambda = 1064$  nm 10 times higher shows the true growth potential of  $\lambda = 1064$  nm. Please also note that the intersection of the  $\lambda = 532$  nm curve with  $\lambda = 1064$  nm curve shifts as we scale the power. This can be very useful for maximising the resolution of the method for certain particle sizes. However, this can be done only

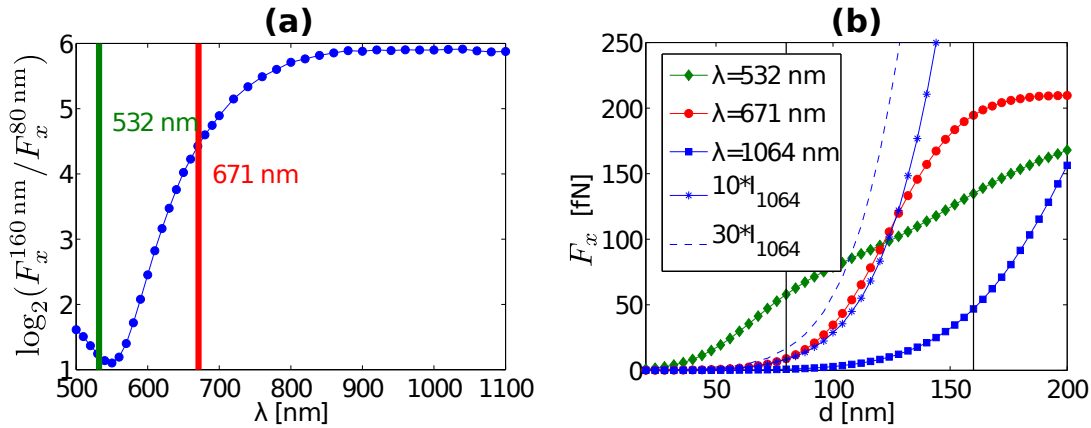


Fig. 4.3: (a) The force growth rate  $\alpha$  as a function of wavelength for the interval of interest (particle diameters from  $d = 80$  nm to  $d = 160$  nm). (b) Optical forces calculated for the same incident intensity of  $0.15 \text{ mW}/\mu\text{m}^2$ . Increasing the power of  $\lambda = 1064$  nm or  $\lambda = 671$  nm shifts the intersection point with  $\lambda = 532$  nm curve to smaller particle sizes. This can be used for optimisation of resolution for certain particle size intervals.

at the expense of an increase in power. Given the heating of a gold nanoparticle is negligible at both  $\lambda = 671$  nm and  $\lambda = 1064$  nm wavelengths, the former is a better choice as the absorption of water at  $\lambda = 1064$  nm is much higher than at  $\lambda = 671$  nm.

### 4.3.2 Forces and velocities in evanescent field

The interaction of metallic nanoparticles with the evanescent waves considered here is numerically studied in Figure 4.4. Figure 4.4a shows the forces experienced by the particle as a function of its diameter for the two wavelengths selected. You can indeed see that the growth factor  $\alpha$  is a good estimate of the gradient of the optical force profile in the interval of particle sizes. The profile of optical force for  $\lambda = 532$  nm is almost linear ( $\alpha \approx 1$ ) whereas the optical force profile for  $\lambda = 671$  nm is very steep ( $\alpha \approx 4.5$ ). The difference in behaviour is due to the plasmon resonance, which is highlighted in Figure 4.4b. The peaks in the force normalised by the geometrical cross-section give evidence of the increased coupling efficiency of the light into the nanoparticle due to the plasmon resonance. We remark that a dielectric particle on this size scale, and at these wavelengths, would not exhibit any resonance effect precluding their sorting using this approach.

A nanoparticle of a given size experiences a total force due to the cumulative effect of the two optical fields, with a terminal velocity shown in Figure 4.4c. The optical force and corresponding terminal velocity were calculated for a gap of 50 nm between the particle and the interface. The corrections due to the proximity of the interface were also included [112]. Altering the intensity ratio between the beams shifts the threshold diameter for which the velocity changes sign. In our specific case,

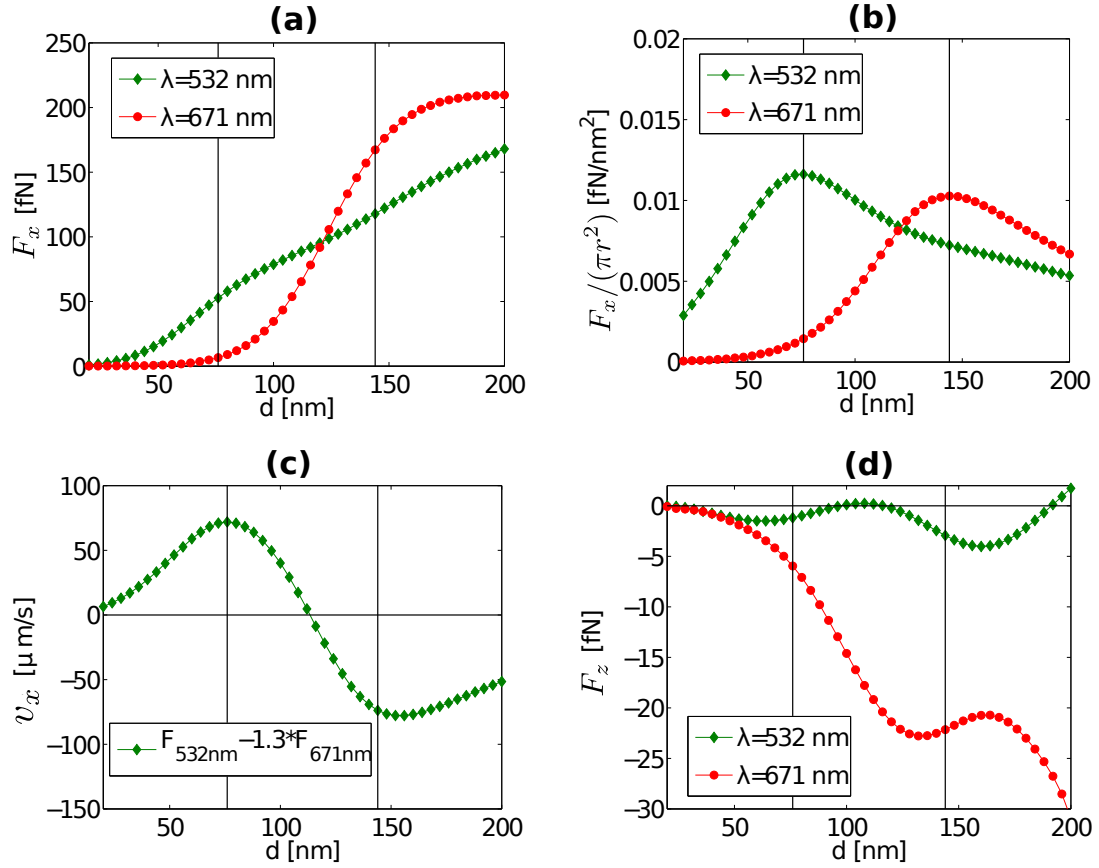


Fig. 4.4: (a) The in-plane ( $x, y$ ) optical force as a function of particle diameter calculated for a p-polarised plane-wave (incident intensity of  $0.15 \text{ mW}/\mu\text{m}^2$  for both wavelengths). We considered an incident angle of  $\theta = 62^\circ$  at the glass-water interface. (b) Interaction efficiencies as a function of nanoparticle size for the two wavelengths used. (c) Velocity of the particles in counter-propagating evanescent field with intensity  $I_{532} = 0.15 \text{ mW}/\mu\text{m}^2$  and  $I_{671} = 0.2 \text{ mW}/\mu\text{m}^2$  used in the experiment. (d) Vertical attractive forces ( $z$ -direction) acting on nanoparticles of different diameters.

selecting the value of the ratio as  $I_{671}/I_{532} = 1.3$  yields the threshold nanoparticle diameter of  $d = 110$  nm. Please note that the cumulative effect of the two evanescent fields attracts the particle toward the substrate (Fig. 4.4d), but notice that the main contribution to the attractive force is from  $\lambda = 671$  nm laser.

### 4.3.3 The experimental setup

The experimental scheme used for optical sorting of gold nanoparticles is shown in Figure 4.5. Two diode pumped solid state lasers (MGL-III-532-300mW,  $\lambda = 532$  nm, Laser 2000) and (MRL-III-671-300mW,  $\lambda = 671$  nm, Laser 2000) were focused to the opposite edges of the back-focal plane of a TIRF (NIKON Apo,  $NA = 1.49$ ) oil immersion objective. The objective's high NA allows for incident beam angles necessary for the generation of evanescent fields and a facile incident angle control when compared to the Kretschmann prism-coupling geometry. The focusing of the beams at the back-focal plane (angular spectrum plane) ensures a very narrow wavevector distribution of the field within the sample plane. The angle of incidence of the beams is controlled by two steering mirrors positioned in a plane conjugate to the sample plane. This configuration keeps the position of the beams fixed in the sample plane while enabling a variation of the incident angle. The beam waist of each of the two beams in the sample plane is equal to  $8.5 \mu\text{m}$ , which provides a sufficiently large two dimensional region for sorting. The critical angle for both lasers is found by detecting the scattered intensity from an immobile gold nanoparticle adhered to the glass-water interface. As the intensity at the interface peaks at the critical angle, the intensity scattered to CCD is maximum for this angle. The position of the two laser spots at the interface is then exactly overlapped by recording the scattering of an immobilised particle along several vertical and horizontal lines and detecting the position of the intensity maximum and the intensity drop along the lines. The light scattered from particles to CCD is also used for real-time particle identification. This method is feasible if the scattering cross-section changes significantly with particle size, which indeed we used in our subsequent diagnostics. Consequently, scattered light from the nanoparticles at  $\lambda = 671$  nm provides better nanoparticle size discrimination than the recorded scattered light at  $\lambda = 532$  nm (Fig. 4.6).

We have used a mixture of gold nanoparticles with diameter of 100 nm (CYTO-DIAGNOSTICS, CG-100-20, coefficient of variation  $CV = 0.08$ ) and 150 nm (CG-Custom-150nm,  $CV = 0.08$ ) for experimental demonstration of the sorting method. The coefficient of variation corresponds to a relative standard deviation in particle diameter of 8 nm for the 100 nm nanoparticles and 12 nm for the 150 nm nanoparticles respectively. This was confirmed from several images (Fig. 4.7) from a scanning electron microscope (SEM). The mixture was prepared by combining  $10 \mu\text{l}$  of each commercially available particle solution (both with concentration of nanoparticles of  $\sim 6 \times 10^{-15}$  mol/ml). The mixture was subsequently diluted with deionised water in ratio 1:1. The resulting particle concentration allows for reasonable frequency of sorting events and negligible probability of inter-particle interactions in the sorting

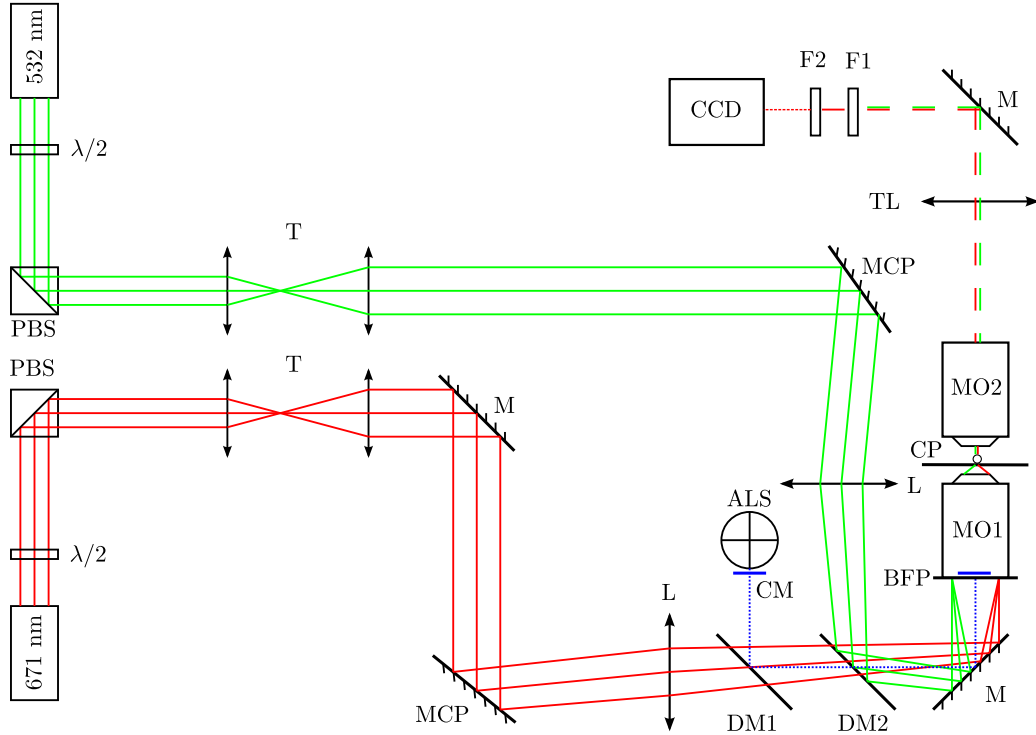


Fig. 4.5: Two diode pumped solid state lasers (MGL-III-532-300mW,  $\lambda = 532$  nm, Laser 2000) and (MRL-III-671-300mW,  $\lambda = 671$  nm, Laser 2000) pass through  $\lambda/2$  wave-plate and polarising beam-splitter (PBS). Both beams are enlarged by telescopes T (N-BK7; AR coated 350 – 700 nm plano-convex  $f_1 = 60$  mm,  $f_2 = 200$  mm for  $\lambda = 532$  nm path and AR coated 650 – 1050 nm plano-convex  $f_1 = 75$  mm,  $f_2 = 200$  mm for  $\lambda = 671$  nm path) to give optimal beam waist at the back-focal plane (BFP) of TIRF (NIKON Apo,  $NA = 1.49$ ) oil immersion objective (MO1). Both beams are steered at the BFP of MO1 by two mirrors (MCP) positioned in the conjugate plane (CP) of image plane. Two lenses L (N-BK7; AR coated 350 – 700 nm plano-convex  $f = 400$  mm for  $\lambda = 532$  nm path and AR coated 650 – 1050 nm plano-convex  $f = 400$  mm for  $\lambda = 671$  nm path) are used to focus the beams to BFP of MO1. Auxiliary light source (ALS) in standard Koehler illumination path is used for sample illumination. Additional circular mask (CM) is imaged to the BFP to get partial dark-field illumination for better contrast of small gold nanoparticles in sample plane in initial alignment step. Mask CM was printed on transparent foil by standard laser printer. Two dichroic mirrors DM1 (FF660-Di02, Semrock) and DM2 (FF494/540/650-Di01, Semrock) are used to combine all the light paths. Field scattered from gold nanoparticle is collected by objective MO2 (Nikon, 40x,  $NA=0.65$ ) and tube lens TL is used to image sample plane on the CCD (Basler, piA640-210gc). Two filters F1 (NF01-532U, Semrock) and F2 (home-built single edge filter to limit the intensity of  $\lambda = 671$  nm signal) are used to limit the intensity of signal on CCD. Vinyl spacer (thickness  $\sim 0.1$  mm) on top of glass cover-slip (thickness  $\sim 0.17$  mm) forms the sample chamber. The chamber is then filled with mixture of gold nanoparticles and covered with another cover-glass. The chamber is sealed using nail polish.

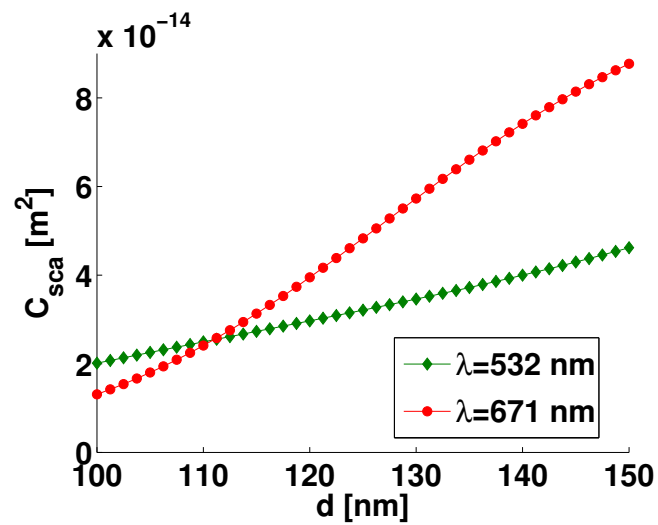


Fig. 4.6: The scattering cross-section  $C_{sca}$  exhibits much stronger variation with particle size for  $\lambda = 671$  nm. This renders the wavelength more suitable for detection because the on-line detection scheme relies on detected intensity for particle identification and steeper variation is desirable.

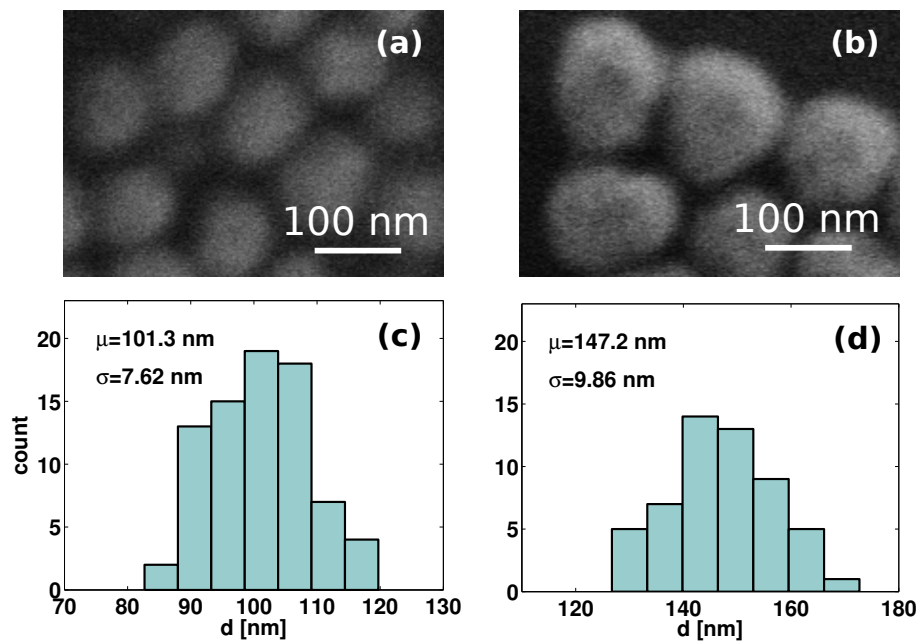


Fig. 4.7: SEM picture of nanoparticles with nominal diameter of (a) 100 nm and (b) 150 nm. Histograms of particle diameters with mean  $\mu$  and standard deviation  $\sigma$  values for (c) 100 nm and (d) 150 nm. (Special thanks to Andrea Di Falco for taking the SEM images.)

experiments.

### 4.3.4 Results of the sorting experiment

The sorting performance is presented in Fig. 4.8. Fig. 4.8a shows a time sequence for two typical sorting events in a mixture of gold nanoparticles using the real-time particle identification scheme. Both events are from the same video, recorded in the same region and with identical dual-wavelength illumination. As expected, the

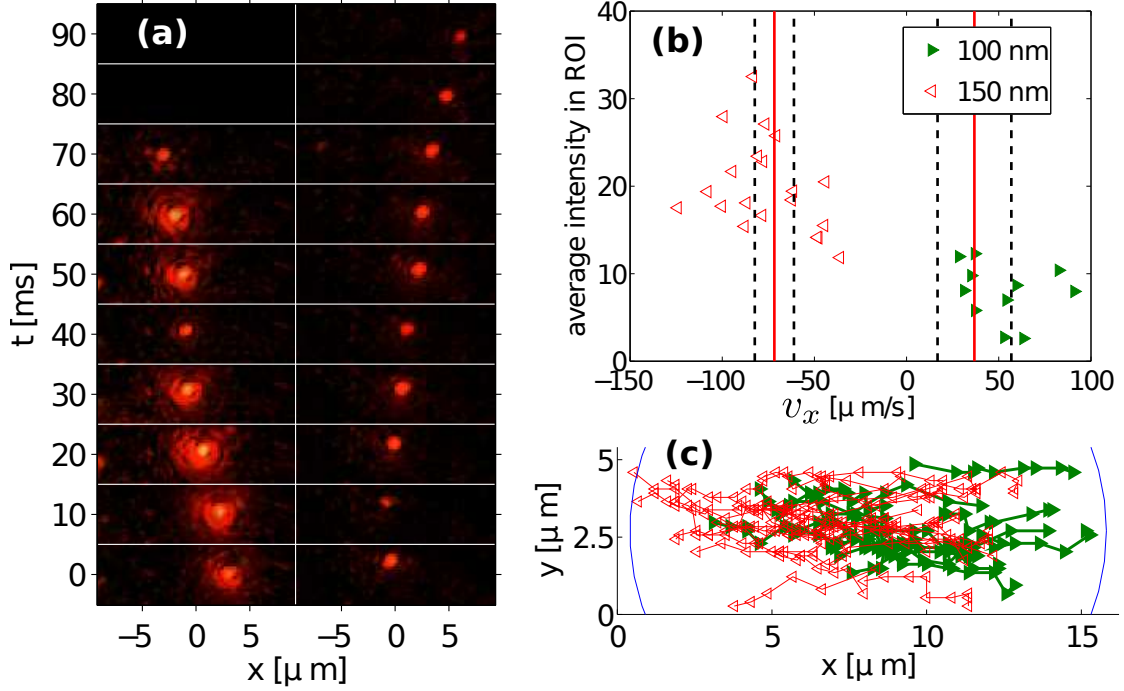


Fig. 4.8: (a) Sequence of frames for two selected particle events. The left sequence corresponds to the larger nanoparticle (150 nm), and the right sequence shows the smaller one (100 nm). (b) The statistics shows the separation into two separate clusters with velocities being in opposite directions as expected. The vertical full red lines show predicted mean velocities for normally distributed sizes in ensembles with mean diameter of 100 nm and 150 nm. The black dashed lines show standard deviation of velocities for the same ensembles. The ROI is the region of interest recorded by the camera and depicted in (a). (c) The trajectories of the particles corresponding to data points in (b). The blue curve shows the waists  $w_0$  of the incident light fields.

“low-intensity” scattering nanoparticle (100 nm) moves in one direction, while the “high-intensity” scattering particle (150 nm) moves in the opposite direction. We also remark that the “high-intensity” scattering nanoparticle slows down significantly at around  $t = 40$  ms when its intensity drops due to its diffusion away from the glass-water interface. This diffusion, together with particle size distribution,

introduces a variation of particle velocity and of detected intensity in Figure 4.8b, where the entire series of sorting events, from the same video as the sequence of Figure 4.8a, is presented. There are two clearly distinguishable clusters separated both in velocity and in detected intensity. These clusters are representative of the respective nanoparticle size ensembles in the mixed solution. We note that experiments with a single size distribution do not show any degree of separation. The vertical axis in Fig. 4.8b denotes the average intensity detected by the CCD over all the frames in the sorting experiment. The acquisition starts when the scattering intensity reaches a certain threshold and stops when the intensity drops below this threshold. The particle trajectories acquired in this way, for the data points in Fig. 4.8b, are shown in Fig. 4.8c. The trajectories show a clear overlap which excludes the possibility of observed behaviour due to misaligned laser spots.

Particle diffusion in the  $z$ -direction induces a large variation in the scattering intensity detected by the CCD. Therefore, in general, the dynamic range of the CCD does not allow the simultaneous tracking of low scattering nanoparticles without saturating some of the camera pixels for the high scattering ones. This leads to a systematic bias for the high intensity events, with expected intensity values for larger particles even higher than those measured in Fig. 4.8b. Consequently, using a camera with higher dynamic range would improve the separation of clusters on intensity axis.

The experimental results are supported by theoretically calculated values of ensemble velocities shown on Figure 4.8b as full red lines for mean ensemble velocity and as dashed black lines for standard deviation in velocity. The average temperature increase in the vicinity of the particle due to laser excitation was estimated [65] to be 18 K, which was accounted for in velocity calculation by setting water viscosity to  $\eta_{40^\circ\text{C}} = 0.65 \times 10^{-3} \text{ Pa} \cdot \text{s}$ . The theoretical and experimental values are in very good agreement. The much narrower expected variation of velocity for 150 nm ensemble, compared to velocity variation for 100 nm ensemble, is due to very flat velocity profile around  $d = 150 \text{ nm}$  in Fig. 4.4c. Also notice that the occurrence of larger particles in sorting events is slightly higher, which is due to stronger gradient force, more efficient for attracting the particles towards surface (see Fig. 4.4d).

Distinct separation of the velocity clusters in Fig. 4.8b and the flat velocity profile in Fig. 4.4c clearly indicate that the sorting scheme should be applicable for sorting of particles with smaller differences in sizes. Indeed, we have successfully repeated the experiment for particles of 100 nm and 130 nm in diameter. The experimental conditions were the same. Fig. 4.9 shows the results of 10 min video acquisition. There is still a clear gap in velocity between  $d = 100 \text{ nm}$  and  $d = 130 \text{ nm}$  clusters and the bidirectional character of sorting is maintained. The reason for the similar output to Fig. 4.8b is due to very flat velocity profile (Fig. 4.4c) near  $d = 150 \text{ nm}$ .

Please note that compared to Fig 4.8b, the variation of velocity for  $d = 130 \text{ nm}$  particles falls within the standard deviation boundaries. Also, even though the expected variation for  $d = 150 \text{ nm}$  was smaller in Fig. 4.8b, the measured variation was much higher than the expected one. One possible explanation for this behaviour could be a higher variability of shapes or a more significant surface roughness for

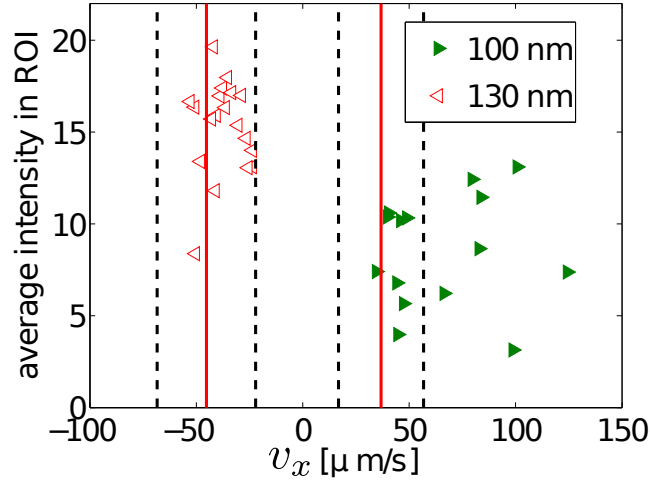


Fig. 4.9: Two distinguishable clusters were detected for mixture containing gold nanoparticles of  $d = 100$  nm and  $d = 130$  nm. The cluster for  $d = 130$  nm has on average lower intensity than the  $d = 150$  nm cluster in Fig. 4.8b. This expected intensity drop introduces ambiguity to detection scheme as the detected intensities have significant overlap.

$d = 150$  nm case.

The drop in detected intensity for  $d = 130$  nm also introduces ambiguity to our on-line detection scheme as the cluster intensities exhibit significant overlap. As a result, unique identification of particle from its scattered intensity is lost. An improved detection scheme would overcome this limitation. Importantly, the velocity clusters have a significant velocity gap between them. With improvements on the detection site, the expected optical resolution of the method is much higher.

### 4.3.5 Resolution of the method

For successful sorting, the difference in particle velocities has to be significantly larger than the diffusion speed. In other words, the distance travelled by particles due to optically induced forces needs to be significantly larger than the mean square displacement due to diffusion in a given time interval. In our experimental demonstration, the particles reach the beam waist in approximately  $t = 0.1$  s, at which point, they are separated by  $17 \mu\text{m}$ . Mean square displacement due to diffusion in the same time is given by

$$\sqrt{\langle x^2 \rangle} = \sqrt{\frac{2tk_B T}{6\pi\eta r}} \quad (4.3)$$

and is equal to approximately  $1 \mu\text{m}$  for both particle sizes. This means that for mean values, the particles are still separated by approximately  $15 \mu\text{m}$ . The calculated gradient of velocity further shows that for 108 nm and 120 nm, the particles would

reach the beam waist in roughly 0.5 s. Due to diffusion the separation is reduced from 17  $\mu\text{m}$  to 12  $\mu\text{m}$ . Even the 112 nm and 116 nm case generates 10  $\mu\text{m}$  separation with diffusion included which is still usable. Also, further increasing the power might improve this separation significantly.

We have also performed Monte Carlo simulations of particle trajectories (an example for one particular particle trajectory is depicted in Fig. 4.10) to characterise

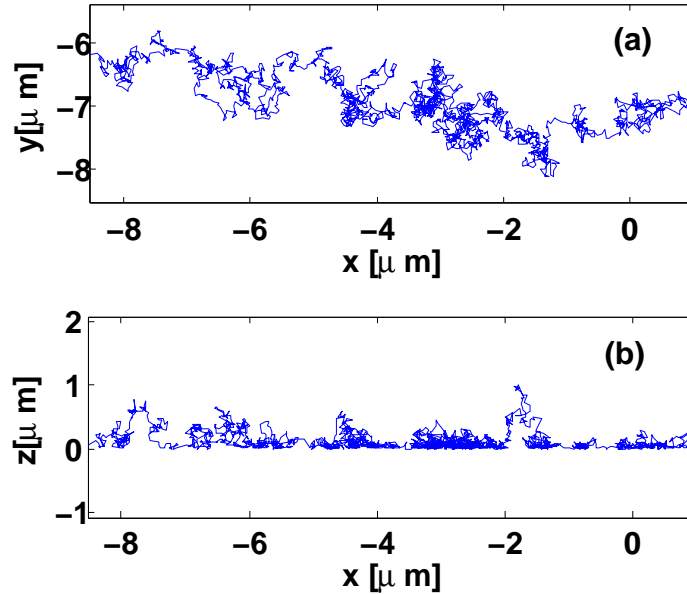


Fig. 4.10: Simulation of the Brownian motion for the particle of diameter  $d = 150$  nm in the (a)  $xy$ -plane and (b)  $xz$ -plane. The particle in (a) is randomly dropped in ROI and moves to the left. Brownian motion in (b) is restricted by the interface ( $z = 0$ ) and the evanescent field ensures particle confinement close to the interface.

the resolution of the method. If we assume that the mixture contains  $N$  particles of nominal diameters  $d_1$  and  $d_2$ , where  $d_1 > d_2$ , then the simulation of resolution consists of the following steps.  $N/2$  particles with diameter  $d_1$  and  $N/2$  particles with diameter  $d_2$  are “dropped” into the beam waist (dual-beam illuminated region) and their trajectories are simulated for a period of time  $t$ . The position of the “drop” (in  $x$  and  $y$ ) is selected from normal distribution with  $\sigma$  equal to beam waist  $w_0$ . The normal distribution is truncated at  $(9/10) \cdot w_0$ , which ensures that all particles start within the beam waist boundaries, but not exactly at the boundary. The initial  $z$ -position is assumed to be fixed at the glass-water interface. Further, two detectors (pick-up positions) are positioned at the distances  $x_1 = -w_0$  (larger particle detector) and  $x_2 = w_0$  (smaller particle detector). The truncation of normal distribution avoids the issue of “dropping” the particles too close to the detector, which would bias the results. There are four possible outcomes of the “drop”:

- Particle hits its correct detector within the simulation time. The sorting is considered successful. ( $N_{\text{correct}}$ )

$d_1$ [nm]	$d_2$ [nm]	$N_{\text{correct}}$	$N_{\text{escape}}$	$N_{\text{unresolved}}$	$R$	$\gamma$
150	100	364	549	73	0.96	1
130	100	249	653	85	0.95	1
120	110	115	755	109	0.84	1
120	110	347	482	160	0.97	2
116	112	392	379	209	0.95	3

Tab. 4.2: Relative power requirements compared to power used in experiment (factor  $\gamma$ ) for different combinations of particle sizes. For combinations of particle sizes sorted in the experiment, the actual power employed in the experiment appears to be sufficient to resolve the particles. For the particle combination 110 nm and 120 nm the power needs to be increased by a factor of  $\gamma = 2$  to resolve the particles. Particles of even smaller difference in diameter require the power to be scaled by at least a factor of  $\gamma = 3$  to be resolved efficiently.

- Particle hits the incorrect detector. The sorting failed. ( $N_{\text{incorrect}}$ )
- Particle does not hit any detector in the simulated time interval but stays within the evanescent field at any given time. ( $N_{\text{unresolved}}$ )
- Particle escapes from the evanescent field. The threshold distance is given by the height  $h$ . ( $N_{\text{escaped}}$ )

Since we cannot detect particles that immediately escape from the evanescent field, we subtract  $N_{\text{escaped}}$  in our calculations. The  $N_{\text{unresolved}}$  are particles that are not yet resolved. As we are only interested in size of particles already being in pick-up positions, this term is also subtracted from the total number of events.

If we define the limit of size resolution as a point when 95% of the observed particles are detected with the correct detector, then we can find the particle sizes and conditions for which the requirement holds using the following relation:

$$R = \frac{N_{\text{correct}}}{N - N_{\text{escaped}} - N_{\text{unresolved}}}. \quad (4.4)$$

Tab. 4.2 shows the particle size differences that can be resolved under various conditions. simulations were performed using  $N = 1000$  particles for each combination of sizes; the time was set to  $t = 1$  s and the threshold height for which the particle was considered as escaped was set to  $h = 2 \mu\text{m}$ . The factor  $\gamma$  is then the ratio between power used in the simulation to the power used in the experiment.

We can clearly see, that for particle sizes used in experiment, the used power is sufficient for efficient sorting. As we decrease the particle size difference, a significant fraction of particles are registered on the incorrect detector. However, increasing the power only slightly - by a factor of  $\gamma = 2$  for 110 nm and 120 nm case, and by a factor of  $\gamma = 3$  for 112 nm and 116 nm - allows for efficient particle sorting even for these differences.

We can conclude, from these results, that it should be possible to optically sort gold nanoparticles with size difference of less than 5%.

### 4.3.6 Further improvements

Significant improvement of the method could be achieved by implementing a better confinement of particles near the substrate. In the present configuration, the confinement of the particle near the substrate is relatively weak (Fig. 4.11b). In fact,

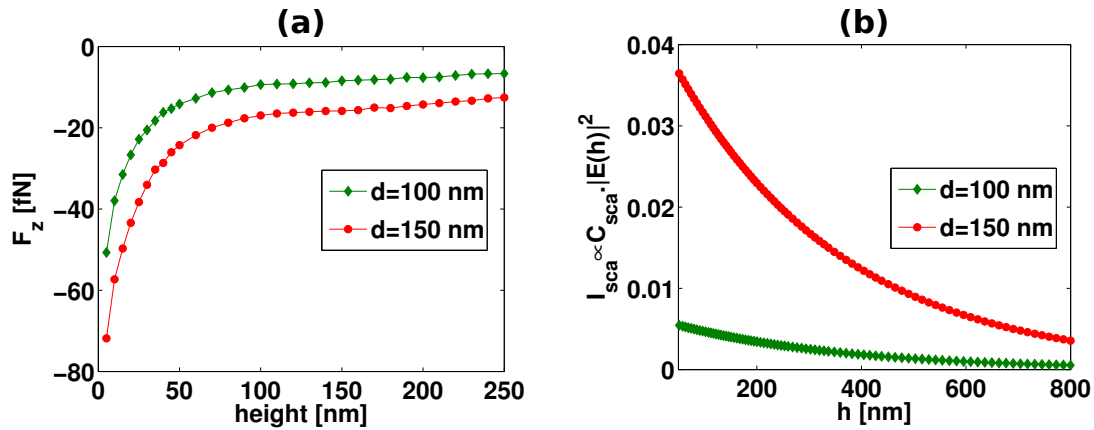


Fig. 4.11: (a) Vertical force  $F_z$  acting on gold nanoparticles in evanescent field generated by p-polarised plane-wave incident at the angle of  $62^\circ$  at glass-water interface. Incident intensity is  $0.15 \text{ mW}/\mu\text{m}^2$  for  $\lambda = 532 \text{ nm}$  and  $0.20 \text{ mW}/\mu\text{m}^2$  for  $\lambda = 671 \text{ nm}$ . (b) Estimate of scattered intensity shows a significant difference between  $d = 100 \text{ nm}$  and  $d = 150 \text{ nm}$  case. Please note that the experimental intensity was averaged over the whole region detected by CCD and some frames were saturated as well. As a result, the observed intensity difference is much smaller than the predicted difference.

the integration of curves in Fig. 4.11a from 5 nm to 250 nm results in the optical well depth of  $\sim k_B T$ . This unfortunately introduces strong variation to particle velocity. This means that even if the particles are of exactly the same size, they will, in general, have different average velocity in the sorting region. The average velocity will correlate with the average height at which the particle moved through the sorting field. If we force all the particles to a very narrow region near the substrate, we would remove this variation and consequently improve to resolution.

The relatively weak confinement further influences the detection scheme as the detected intensity also changes with height of the particle above the substrate (Fig. 4.11b). Again, this kind of variation could be minimised by better confinement of particles near the substrate.

For any practical applications, it is also necessary to develop a mechanism able to confine the particles that are about to leave the dual illuminated region.

### 4.3.7 Limitations of the method

The red-shift of the plasmon resonance is a key ingredient for efficient bidirectional sorting of the particles. Unfortunately the red-shift of dipole mode resonance for smaller gold nanoparticles is negligible (Fig. 4.12c). The consequence of small plasmon resonance shift is very flat  $\alpha$  profile (Fig. 4.12a) in this smaller particle size range compared to  $\alpha$  profile in Fig. 4.3a.

The subtraction of force profiles with maximum difference in force growth rate is optimal in this case. Even then, much higher laser intensity is needed for only modest particle speeds (4.12d). This is partly due to smaller particle size and partly due to non-optimum nature of wavelengths used.

Small attractive forces (4.12e) would also generate negligible optical potential well for smaller particles. As a result, particles would not be confined near the substrate by the evanescent field. This would add significant variation to both, detected intensity and velocity. However, methods suggested in conclusion might significantly improve this vertical confinement of smaller particles.

## 4.4 Conclusion

In summary, we have demonstrated the first experimental realisation of size-selective optical sorting of gold nanoparticles. Our dual wavelength configuration utilised the red-shift of the plasmon resonance that appears with increasing particle size, to tailor the forces acting on nanoparticles such that nanoparticles of different sizes move in opposite directions. The method, in its current implementation, allows for separation of particles with a diameter difference of 30 nm, for the nominal diameters of 100 nm and 130 nm. The present resolution limit stems from the limitation of the real-time detection scheme, which is hampered by non-negligible z-diffusion of the particles.

Various approaches exist for reducing the z-diffusion to improve the technique such as using a weakly focused non-resonant auxiliary laser to push nanoparticles towards the glass-water interface. Alternatively, coating the substrate with nanolayer of gold or the use of a dielectric resonator [50] may significantly enhance the gradient forces attracting the nanoparticle to the surface. In the case of a gold layer, the coupling of surface plasmon polaritons into gold layer would increase both the intensity of field at the interface and the gradient force attracting the particles towards the interface [113, 114]. Intriguingly, the coupling between surface plasmon polaritons within the gold layer and localised surface plasmon supported by the nanoparticle might also offer additional degrees of freedom for tailoring the sensitivity of optical force to particle size. Finally an improvement of particle confinement is also possible through the use of shaped light fields [115] or standing wave traps [116].

The method should be also applicable for sorting of various particle shapes. In fact, the shape variation is one of the reasons for bigger than expected velocity variation in Fig. 4.8b. Actually, the SEM images reveal that a tiny fraction of the fabricated particles have a completely different shapes such as triangles or rods (Fig. 4.13). These shapes will have, in general, very different resonance frequency

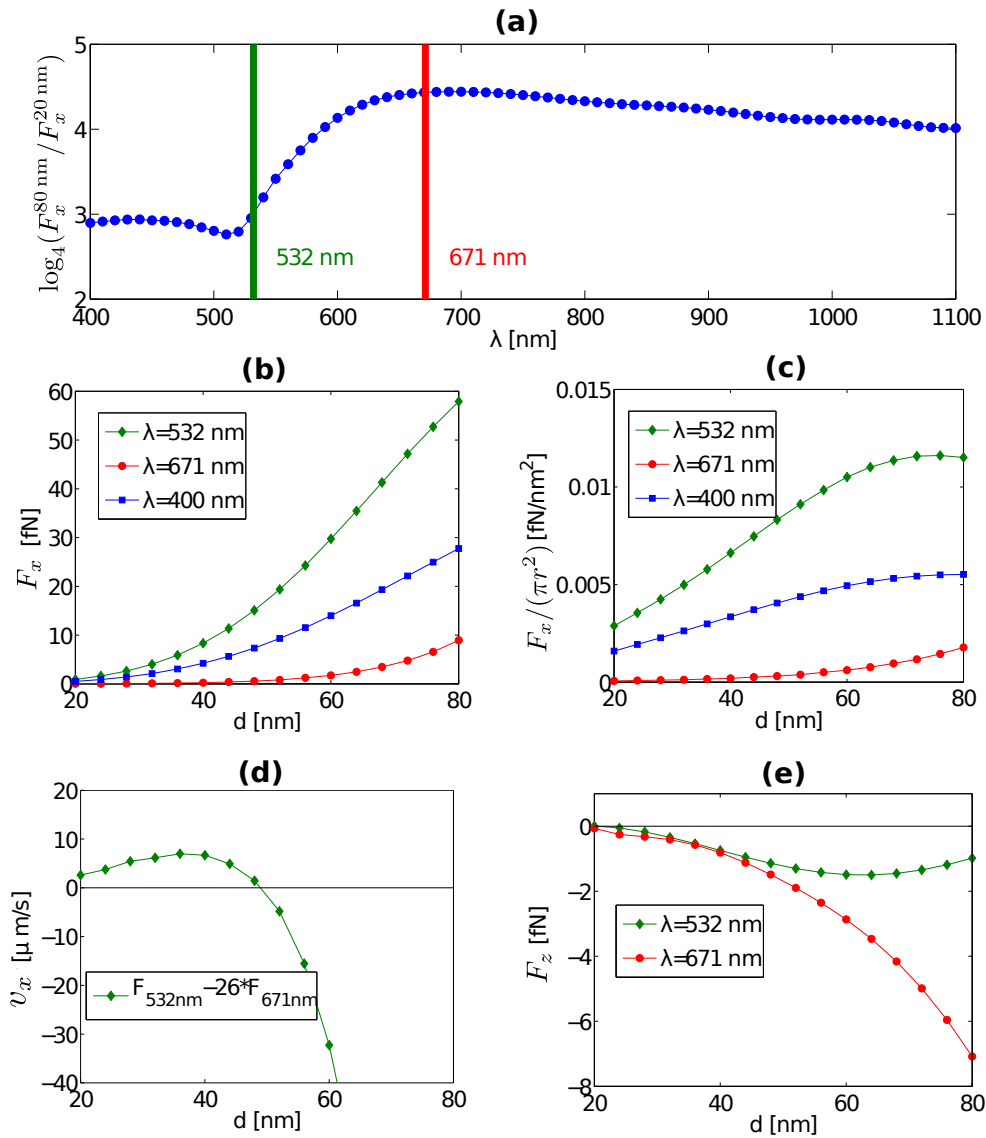


Fig. 4.12: (a) Same laser wavelengths as those used in manuscript are suitable for sorting of gold nanoparticles in the range of 20 nm to 80 nm; (b) In-plane forces for powers equal to  $I = 0.15 \text{ mW}/\mu\text{m}^2$ ; (c) The positioning of the resonance peak to smaller particle diameter renders very difficult as the resonance shifts negligibly with shorter wavelengths. (d) The bidirectional pattern for velocity is still achievable, however, at the expense of significantly increased power of the red laser. (e) Vertical forces attract the nanoparticles to substrate for all particle diameters and for both wavelengths.

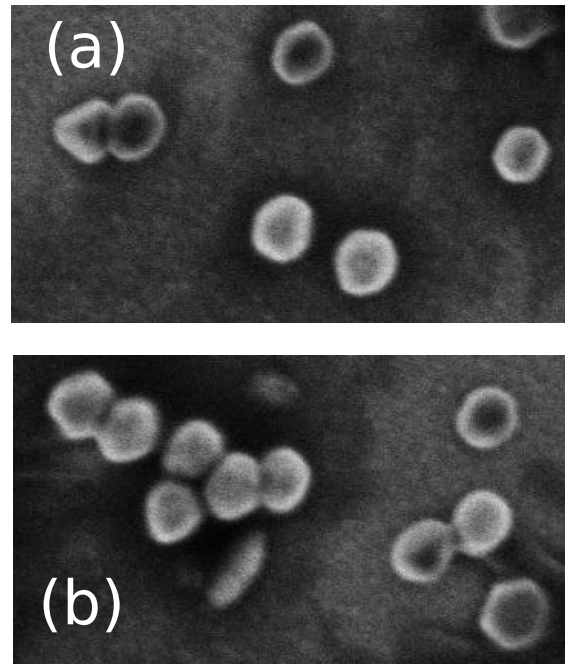


Fig. 4.13: Small fraction of nanoparticles in the mixture does not have a spherical shape. The SEM images above show nanoparticles with a shape of (a) triangle and (b) rod.

and their cross-section will differ significantly from a spherical shape. We have observed these unusual shapes very sporadically in our sorting experiments (accounting for roughly 1 in 100 events). They usually exhibit itself by moving noticeably faster or slower than the expected velocities for the ensemble in the mixture. Unfortunately, the unique identification of these stray particles is not possible in current implementation of the detection. We plan to resolve this problem by improving the detection scheme by introducing additional camera into the system. This additional camera would record scattering intensity for the  $\lambda = 532$  nm laser. The parallel acquisition of the scattered intensity at two wavelengths should provide more specific information about particle shape and size. For example, each gold nanoparticle size, in the explored size range, should have a unique ratio of scattering intensity (Fig. 4.14). This approach could thus also remove some of the uncertainty of the detection scheme introduced through particle diffusion in the  $z$ -direction.

There is also a need to develop a method able to pick up the particles in the region where they are about to leave the field confining them to the interface. Without a mechanism able to pick and immobilise the sorted nanoparticles at the end of the sorting region, the particles diffuse. One possible solution is to build a simple setup that would recognise the particle moving in one direction (CCD particle tracking framerate is sufficient) and trigger a strong optical trap for confinement in a position where the particle is about to leave the evanescent field. Also, specially designed microfluidic chambers may be used to collect the sorted fractions to obviate this

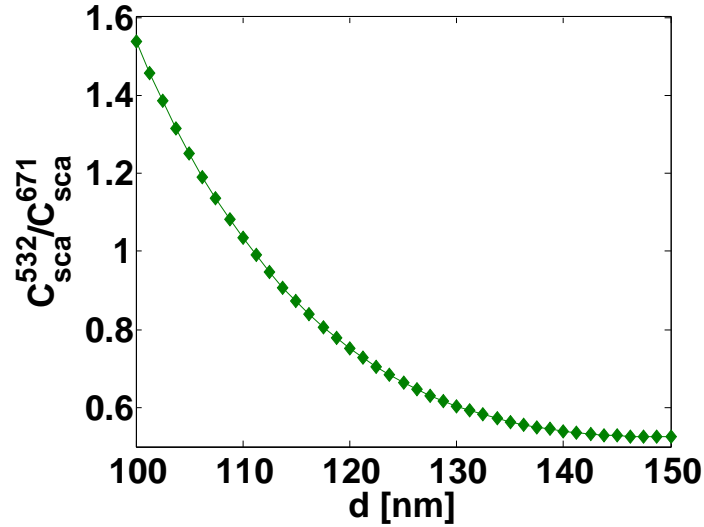


Fig. 4.14: The ratio of the scattering cross-section as a function of gold nanoparticle diameter. The ratio is particularly sensitive to particle diameter in the region from 100 nm to 120 nm. The knowledge of the ratio provides a more specific information about the particle size than the currently recorded average intensity of the particle in ROI.

edge diffusion to some extent.

For the above mentioned reasons we believe that the gold nanoparticle sorting by light promises an interesting new avenue exploiting the rich dynamics of the interplay between optical forces and particle resonances. Also bear in mind that the research presented in this chapter is only a proof of principle concept and as such it can be significantly improved. One possible improvement involves already mentioned beam-shaping of light fields [115] realising the sorting of particles.

This brings us to the last chapter of the thesis where we introduce a method, published in Ref. [115], that represents a first step towards beam-shape and wavelength optimisation of plasmon based sorting. The method was published before the experimental sorting realisation. Due to its heavy computational load the method was studied only in 2D scenario and for this reason it was not applied for our proof-of-principle sorting experiment. Nevertheless, the method forms a very elegant theoretical framework for optimising optical sorting and as such it is well worth studying.



## Chapter 5

# Optimisation of optical sorting of gold nanoparticles<sup>1</sup>

The previous chapter presented an experimental method for size-based optical sorting of gold nanoparticles based on the red-shift of plasmon resonance for increasing particle size. The sorting was realised in a region illuminated by two counter-propagating Gaussian beams incident at the critical angle on the glass-water interface. However, the question that remains unanswered is whether the Gaussian beam illumination provides optimal near-field for such a sorting application<sup>2</sup>. One can envision, for example, a completely different beam shape that would couple very strongly with the larger particle while, at the same time, had a minimum coupling to a smaller one. Furthermore, one can even envision a beam shape with those properties that would, simultaneously, achieve this with minimal heating of the system.

In this chapter we present a general method, published in Ref. [115], that can be readily used to find such a beam shape. Since any beam shape is completely determined by its far-field, the fundamental task is to find the amplitude and phase of this optimal beam in the far-field plane. In the case of the microscope objective the far-field plane is identical to a back-focal plane (Fig. 5.1). Our method, based on **force optical eigenmodes** (FOEi) [117], is able to find the optimal amplitude and phase of such a beam by testing the response of the system to a certain set of interfering plane-waves. The solution obtained in this way can be experimentally implemented by the phase and amplitude spatial light modulator (SLM) in the conjugate plane to the back-focal plane of the microscope objective.

Due to the complexity of the FOEi method, let us first begin by demonstration of the FOEi method in a comparatively simpler case of finding the beam-shape optimising the push force acting on the particle. This simple approach will be later extended to optimise the force difference between two particles of different sizes over

---

<sup>1</sup>Part of the chapter reprinted from [115]. Copyright 2011 OSA.

<sup>2</sup>We do not consider here the possibility to change the near-field through introduction of additional layer of gold or through any other physical modification of the near-field. We only consider the problem of finding the optimal far-field illumination that optimises the near-field pattern for sorting purposes.

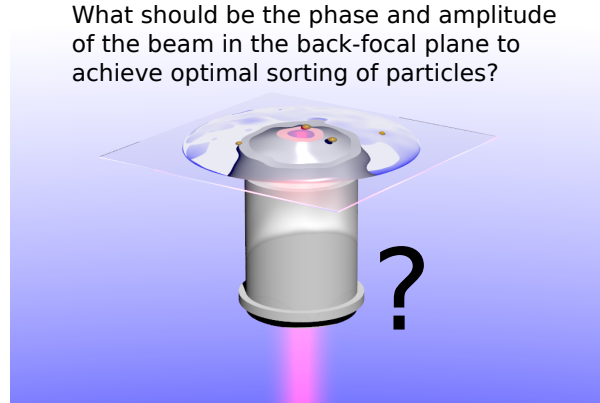


Fig. 5.1: The fundamental problem of this chapter is to find the phase and amplitude of the beam in the back-focal plane of the objective such that the force difference between particles of different sizes is maximised.

a certain region of interest.

## 5.1 The beam-shape for the optimal push force

Our aim is to optimise the incident electromagnetic field  $\mathbf{E}_{inc}$  in a way that maximises the exerted force  $F^{\mathbf{u}} = \mathbf{F} \cdot \mathbf{u}$  in a specified direction  $\mathbf{u}$  for a given particle type (Fig. 5.2). Since our incident field of angular frequency  $\omega$  can be decomposed into a sum of  $\mu$  monochromatic plane waves ( $e^{i\omega t}$ ), we can write (using summation over repeating indices)

$$\mathbf{E}_{inc} = a^\mu \mathbf{E}_{inc}^\mu, \quad (5.1)$$

where  $a^\mu$  are the complex expansion coefficients and  $\mathbf{E}_{inc}^\mu$  are the incident plane waves. The  $a^\mu$  coefficients modulate both phase and amplitude of each and single plane wave independently. The scattered field generated upon interaction with the particle has the same expansion coefficients, so that we can write  $\mathbf{E}_{sca} = a^\mu \mathbf{E}_{sca}^\mu$ . The final field  $\mathbf{E}$ , which is a sum of incident and scattered field, can then be written as

$$\mathbf{E} = a^\mu (\mathbf{E}_{inc}^\mu + \mathbf{E}_{sca}^\mu) = a^\mu \mathbf{E}^\mu, \quad (5.2)$$

where  $\mathbf{E}^\mu$  is a solution of the scattering problem for an incident field given by plane wave  $\mathbf{E}_{inc}^\mu$ .

The optical-cycle averaged electromagnetic force in the direction  $\mathbf{u}$  is given by

$$F^{\mathbf{u}} = \langle F_i \rangle u_i = \oint_C \langle \sigma_{ij} \rangle n_j u_i ds, \quad (5.3)$$

where  $n_j$  is outward unit normal to an element  $ds$  of the curve  $C$  enclosing the particle for which we optimise the force and  $\langle \cdot \rangle$  is optical-cycle average. The Maxwell

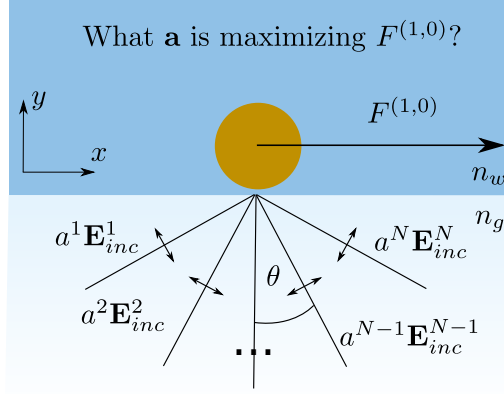


Fig. 5.2: We look for an amplitude and phase  $\mathbf{a}$  of a given set of plane waves such that the force  $F^{(1,0)}$  is maximised.

stress tensor,  $\sigma_{ij}$ , can be written for the final field  $\mathbf{E}$  as [56]

$$\langle \sigma_{ij} \rangle = \frac{1}{4} \left[ \epsilon_0 \epsilon_m E_i^* E_j + \mu_0 \mu_m H_i^* H_j + \epsilon_0 \epsilon_m E_i E_j^* + \mu_0 \mu_m H_i H_j^* - \delta_{ij} (\epsilon_0 \epsilon_m E_k^* E_k + \mu_0 \mu_m H_k^* H_k) \right]. \quad (5.4)$$

Using Eq. (5.2), we can rewrite Eq. (5.4) as

$$\langle \sigma_{ij} \rangle = \frac{1}{4} \left[ \epsilon_0 \epsilon_m (a^\mu E^\mu)_i^* (a^\nu E^\nu)_j + \mu_0 \mu_m (a^\mu H^\mu)_i^* (a^\nu H^\nu)_j + \epsilon_0 \epsilon_m (a^\nu E^\nu)_i (a^\mu E^\mu)_j^* + \mu_0 \mu_m (a^\nu H^\nu)_i (a^\mu H^\mu)_j^* - \delta_{ij} (\epsilon_0 \epsilon_m (a^\mu E^\mu)_k^* (a^\nu E^\nu)_k + \mu_0 \mu_m (a^\mu H^\mu)_k^* (a^\nu H^\nu)_k) \right] \quad (5.5)$$

and after rearrangement of the expansion coefficients  $a^\mu$  we obtain

$$\langle \sigma_{ij} \rangle = (a^\mu)^* \left( \frac{1}{4} \left[ \epsilon_0 \epsilon_m (E^\mu)_i^* E_j^\nu + \mu_0 \mu_m (H^\mu)_i^* H_j^\nu + \epsilon_0 \epsilon_m E_i^\nu (E^\mu)_j^* + \mu_0 \mu_m H_i^\nu (H^\mu)_j^* - \delta_{ij} (\epsilon_0 \epsilon_m (E^\mu)_k^* E_k^\nu + \mu_0 \mu_m (H^\mu)_k^* H_k^\nu) \right] \right) a^\nu. \quad (5.6)$$

Substituting Eq. (5.6) into Eq. (5.3) gives

$$F^{\mathbf{u}} = (a^\mu)^* \left[ \oint_C \left( \frac{1}{4} \left[ \epsilon_0 \epsilon_m (E^\mu)_i^* E_j^\nu + \mu_0 \mu_m (H^\mu)_i^* H_j^\nu + \epsilon_0 \epsilon_m E_i^\nu (E^\mu)_j^* + \mu_0 \mu_m H_i^\nu (H^\mu)_j^* - \delta_{ij} (\epsilon_0 \epsilon_m (E^\mu)_k^* E_k^\nu + \mu_0 \mu_m (H^\mu)_k^* H_k^\nu) \right] \right) n_j u_i ds \right] a^\nu \quad (5.7)$$

or more simply in matrix form

$$F^{\mathbf{u}} = \mathbf{a}^\dagger \mathbf{M} \mathbf{a}, \quad (5.8)$$

where the matrix coefficients  $M^{\mu\nu}$  are given by the line integrals in Eq. (5.8) and  $\mathbf{a}$  is the vector form of  $a^\mu$ . We remark that the matrix  $\mathbf{M}$  is Hermitian ( $\mathbf{M} = \mathbf{M}^\dagger$ ) and thus its eigenvalues are real. This means that the force  $F^{\mathbf{u}}$  is in a symmetric sesquilinear form, which is just an extension of quadratic form ( $\mathbf{x}^T \mathbf{M} \mathbf{x}$ ) to complex numbers. Any symmetric sesquilinear form can be visualised as an ellipsoid with the length of principal axes equal to the eigenvalues  $\lambda_n$  of the matrix  $\mathbf{M}$ . This has far reaching implications for our optimisation process since the surface of the ellipsoid generated<sup>3</sup> by the symmetric sesquilinear form is extremised at the end points of principal axes. This means that finding the eigenvalues  $\lambda_n$  of the matrix  $\mathbf{M}$  (we have used the Cholesky method implemented in MATLAB) and selecting the largest one from the set extremises our problem. The eigenvector (force optical eigenmode)  $\mathbf{a}_n^{max}$  corresponding to maximum eigenvalue  $\lambda_n^{max}$  (given by  $\mathbf{M} \mathbf{a}_n^{max} = \lambda_n^{max} \mathbf{a}_n^{max}$ ), then provides the necessary information about amplitude and phase of incident plane waves  $\mathbf{E}_{inc}^\mu$  in Eq. (5.1) so that the force is maximised. Experimentally, the optimised  $\mathbf{a}_n^{max}$  can be created using spatial light modulator (offering control of both phase and amplitude) in the system placed in the conjugate plane [117] with respect to the back-focal plane of a microscope objective.

We remark that the above described method optimises the force on one type of particle at a single point only. However, the method can be easily extended to provide the optimised illumination for the force difference over the whole sorting region for two types of nanoparticles. This is discussed later in the chapter.

## 5.2 Numerical modelling

We use again the COMSOL Multiphysics v4.1 RF module in scattering formulation to calculate the total field solutions  $\mathbf{E}^\mu$  for corresponding incident plane waves  $\mathbf{E}_{inc}^\mu$ . We first find the solutions  $\mathbf{E}^\mu$  for particle  $p_1$ . We subsequently use the solutions  $\mathbf{E}^\mu$  to find the elements  $M_1^{\mu\nu}$  of matrix  $\mathbf{M}_1$  and determine the eigenvalues and corresponding eigenvectors. The principal eigenvector gives the optimum force for particle  $p_1$  in a single position. The same procedure is repeated for a second type of particle,  $p_2$ , delivering matrix  $\mathbf{M}_2$ . The matrices  $\mathbf{M}_1$  and  $\mathbf{M}_2$  then encode all the information about interactions of the incident fields with the particles. Finding the matrix elements  $M^{\mu\nu}$  of matrix  $\mathbf{M}$  is computationally very intensive as combinations of  $N(N+1)/2$  solutions need to be constructed and integrated over a sphere boundary. Here  $N$  denotes number of plane waves in the angular spectrum representation and thus the number of pixels on spatial light modulator. As the azimuthal discretization of angular spectrum representation increases the number of combinations in 3D significantly, we have restricted the simulations to 2D to illustrate the method.

We can obtain educated estimates of 3D values from 2D values by extruding the

---

<sup>3</sup>The surface of the ellipsoid is used here as a simplifying concept. Arbitrary vector  $\mathbf{x}$  is going to experience some transformation ("rotation") after matrix  $\mathbf{M}$  acts on it. For eigenvectors, no "rotation" appears, just vector scaling. Since the scalar product of two vectors, where one of them is rotated, is always smaller than scalar product of the identical vectors, finding the maximum eigenvalue truly maximises the force.

2D circle of radius  $r$  by  $d$  such that it creates a cylinder with a volume equal to the volume of the sphere with the same radius. The extrusion factor  $d$  is given by

$$\pi r^2 d = \frac{4}{3} \pi r^3 \rightarrow d = \frac{4}{3} r. \quad (5.9)$$

The validity of the COMSOL model was tested in 3D by comparing the optical forces and scattering and absorption efficiencies with Mie theory. The difference between the COMSOL model and the Mie model was less than 2 percent. In 2D, optical forces and scattering and absorption efficiencies were calculated using several independent methods to ensure the model validity. This revealed a maximum error of less than 1% in 2D.

### 5.3 Heating effects in the system

We choose as our testing system gold nanoparticles [46] of radius  $r_1 = 50$  nm and  $r_2 = 40$  nm. We consider a substrate of glass with refractive index  $n_g = 1.5$ . The particles are assumed to be dispersed in water with  $n_w = 1.33$  (Fig. 5.2).

We have seen in the previous chapter that the red-shift of plasmon resonances offers exceptional sensitivity on particle size. However, for nanoparticles of very similar sizes, the force difference generated solely by the plasmon resonance in the system is still rather small. In case of dielectrics, increasing the intensity offers simple solution in such a situation. Unfortunately, plasmon resonances are associated with non-negligible heat generation, and as such, increasing the intensity may produce increased diffusion rates and convective currents, which will interfere with sorting efforts. It is thus beneficial to find a wavelength for which the heating is minimised while the force difference, between particles of distinct size, is maximised.

In the following, we will adopt the FOEi method for single wavelength only and we will find the beam-shape that optimises the force difference for this particular wavelength. The method, however, can be also used to solve for optimum illumination utilising dual wavelength geometry. In such a scenario, the matrices  $\mathbf{M}_1$  and  $\mathbf{M}_2$  have to be constructed independently for both wavelengths.

We choose the p-polarisation for the incident plane waves as the kind of plasmon resonance supported by the sphere appears in 2D for p-polarisation. The s-polarisation would only induce movement of electrons along the infinite cylinder. Fig. 5.3a shows the scattering  $Q_{sca}$  and absorption  $Q_{abs}$  efficiencies for  $r_1 = 50$  nm gold nanoparticle. Note that the 3D efficiencies calculated from Mie theory and the corresponding 2D efficiencies (transformed to 3D) for p-polarisation follow very similar pattern, which differs only in amplitude and a slight blue shift of 2D resonance peaks with respect to 3D resonances. Fig. 5.3b shows the 3D forces along the substrate acting on the gold nanoparticles calculated for plane-wave incident at near critical angle of  $\theta = 64^\circ$ . The slight shift in resonances due to the different sizes of nanoparticles creates a force difference that peaks around 550 nm (black curve in Fig. 5.3b).<sup>4</sup>

---

<sup>4</sup>Please note that this optimal wavelength was calculated for the force difference at constant

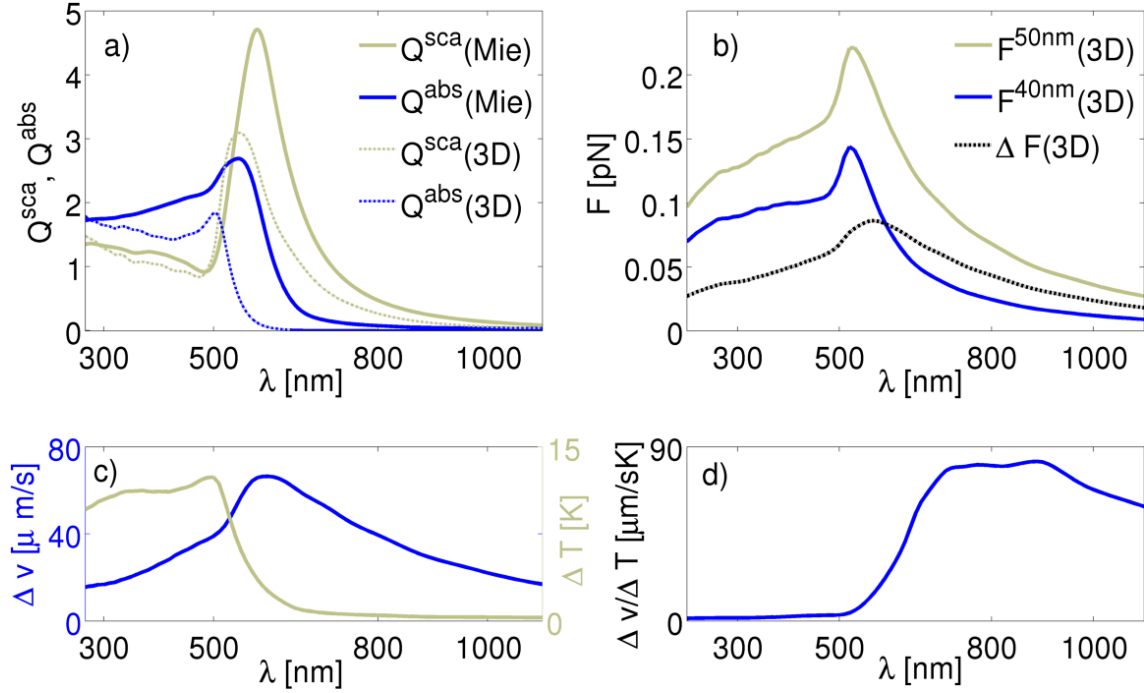


Fig. 5.3: a) Scattering  $Q_{sca}$  and absorption  $Q_{abs}$  efficiencies calculated using Mie theory for 3D nanoparticle of  $r_1 = 50$  nm and the corresponding 2D values converted to 3D equivalents. Nanoparticle is in water with  $n_w = 1.33$ ; b) Forces and their respective difference  $\Delta F$  acting on  $r_1 = 50$  nm and  $r_2 = 40$  nm gold nanoparticles. Forces are parallel to the substrate plane. The illumination is a plane-wave at near critical angle of  $\theta = 64^\circ$  with power density corresponding to  $1 \text{ mW}/\mu\text{m}^2$ ; c) Speed difference  $\Delta v$  and temperature increase  $\Delta T$  for the same illumination as in b); d) Speed difference normalised with respect to the temperature increase in the system.

If we do not take into account the proximity of the spheres to the surface (Faxen's correction [118]) and assume we are in a low Reynolds number regime, then the drag force is given by the Stokes equation. Neglecting inertial effects we can equal optical and drag force and obtain the expression for the particle speed in 3D as

$$v_{3D} = \frac{2F_{2D}}{9\pi\eta}, \quad (5.10)$$

where the force  $F_{2D}$  was calculated in 2D using Eq. (5.8) and the dynamic viscosity of water at  $T = 20^\circ\text{C}$  is  $\eta = 1.002 \times 10^{-3} \text{ Pa}\cdot\text{s}$ . Fig. 5.3c shows the speed difference generated by force differences in Fig. 5.3b and the average temperature increase as the particle enters the sorting field. The estimate of average temperature increase was calculated using [65] (neglecting particle movement and proximity of glass surface)

$$\Delta T = \frac{1}{4\pi} \frac{\mathcal{Q}_1 + \mathcal{Q}_2}{\kappa_0 \cdot \left(\frac{r_1+r_2}{2}\right)}, \quad (5.11)$$

where  $\mathcal{Q}_1$  and  $\mathcal{Q}_2$  are 3D powers of heat generation in nanoparticles with radius  $r_1$  and  $r_2$  and  $\kappa_0 = 0.6 \text{ W}\cdot\text{m}^{-1}\cdot\text{K}^{-1}$  is the thermal conductivity of water. This temperature increase is reached very quickly as the particles enter the sorting field.<sup>5</sup>

Results in Fig. 5.3c,d suggest, that heating at wavelengths above 700 nm is quite low and the velocity difference remains high. For this reason we set the vacuum wavelength for the FOEi method to  $\lambda_0 = 700 \text{ nm}$ .

This treatment also reveals that the wavelength of  $\lambda = 532 \text{ nm}$  used in the sorting method presented in Chapter 4 was by no means optimal in terms of heating. In fact, most of the temperature increase in the system, which was estimated to 18 K can be attributed to this wavelength. Unfortunately, the  $\lambda = 532 \text{ nm}$  wavelength seems to be unique as it demonstrates very low gradient of force profile as a function of particle size. No other wavelength manifests such a low gradient of force profile. It is thus very difficult to avoid using this wavelength for bidirectional sorting because such sorting heavily relies on the combination of steep and flat gradient of force.

## 5.4 Optimising the force difference in the region of interest (ROI)

Using the optimum wavelength from previous section we can proceed with optimisation of the beam shape. We introduce a 10 nm separation between the lowest point of particle and interface, which closely mimics a typical experimental situation. The set of  $N$  incident plane waves defined by  $\mathbf{k}_\theta$  vectors ( $\theta = \langle -70^\circ, \dots, 70^\circ \rangle$ ) with a step

---

incident power for the combination of particle diameters of 80 nm and 100 nm. Such approach gives different results than the growth factor  $\alpha$  approach, which was defined as the ratio of forces for a different interval of sizes. The advantage of force difference approach, presented here, is in the fact that it allows for direct comparison of heating in the system for various wavelengths.

<sup>5</sup>We use the average size of the particle  $(r_1 + r_2)/2$  to estimate the temperature increase due to both particle types being in the sorting field.

of  $2^\circ$ ) is used for discretization (see Fig. 5.2). The limits of  $\theta$  correspond to experimental limitation for NA = 1.4 oil immersion objective. The goal is to optimise the force difference along the direction given by vector  $\mathbf{u} = (1, 0)$ .

Using matrices  $\mathbf{M}_1$  and  $\mathbf{M}_2$ , the equation for force difference at a single point for our choice of particles is

$$\Delta F = F_1^{\mathbf{u}} - F_2^{\mathbf{u}} = \mathbf{a}^\dagger (\mathbf{M}_1^{\mathbf{u}} - \mathbf{M}_2^{\mathbf{u}}) \mathbf{a} = \mathbf{a}^\dagger \mathbf{D}_{12}^{\mathbf{u}} \mathbf{a}. \quad (5.12)$$

Due to the symmetry of the system, two optimum solutions exists - one optimising the force difference in  $+x$  direction and the second for  $-x$  direction. In subsequent discussions we always choose the solution optimising the force in  $+x$  direction. The field locally optimising the force difference for gold nanoparticles of our choice is on Fig. 5.4. Notice that the field creates a very strong field gradient in the  $+x$  direction around point  $x = 0$ , where we want to maximise the force difference for our testing particles. Also notice that the back focal plane pattern corresponding to this field has significant contributions from plane waves propagating in the opposite  $-x$  direction. Although this might seem surprising, we need to realise that the final goal of our method is to interfere the plane waves in such a way to create the strongest gradient in  $+x$  direction. Apparently the counter-propagating waves increase the number of degrees of freedom for efficient interference leading to strong gradient and are thus utilised automatically by the FOEi method. It also makes sense that the increased intensity at the back focal plane appears for near critical angle plane waves as those plane waves contribute the most to the intensity near the glass/water interface. Note that the phase at the back focal plane is also significantly altered to maximise the force difference.

So far our method optimises the force difference locally. To expand this approach to a larger region we need to optimise  $\Delta F$  over a certain range, in our case line segment defined by  $x = \langle -l, l \rangle$ . Displacing the particle in  $x$ -direction causes the particle to experience different relative phases between the fields  $\mathbf{E}^\mu$ . Since we use combination of solutions to calculate matrix  $\mathbf{M}$  this relative phase can be taken into account using

$$M^{\mu\nu}(x) = e^{ik_w \sin(\theta_t^\mu)x} [M^{\mu\nu}] e^{-ik_w \sin(\theta_t^\nu)x} \quad (5.13)$$

where  $k_w = (2\pi/\lambda_0)n_w$  and  $\theta_t^\mu$  is the angle of the plane wave after the glass/water interface for each incident plane wave  $\mathbf{E}_{inc}^\mu$ .  $M^{\mu\nu}$  is the matrix calculated for particle at position  $x = 0$ . Using the above translation relation for matrix  $M^{\mu\nu}$ , we obtain

$$\begin{aligned} \Delta F(l) &= (a^\mu)^* \left[ \frac{1}{2l} \int_{-l}^l e^{ik_w x (\sin(\theta_t^\mu) - \sin(\theta_t^\nu))} dx \right] (M_1^{\mathbf{u}} - M_2^{\mathbf{u}})^{\mu\nu} a^\nu \\ &= (a^\mu)^* \left[ \text{sinc}(k_w l (\sin(\theta_t^\mu) - \sin(\theta_t^\nu))) (M_1^{\mathbf{u}} - M_2^{\mathbf{u}})^{\mu\nu} \right] a^\nu \\ &= \mathbf{a}^\dagger \mathbf{R}_{12}^{\mathbf{u}}(l) \mathbf{a}. \end{aligned} \quad (5.14)$$

The illumination optimisation is then performed on the modified matrix  $\mathbf{R}_{12}^{\mathbf{u}}(l)$ , which has the same input matrices  $M_1^{\mathbf{u}}$  and  $M_2^{\mathbf{u}}$  for all values of  $l$ . Finding the

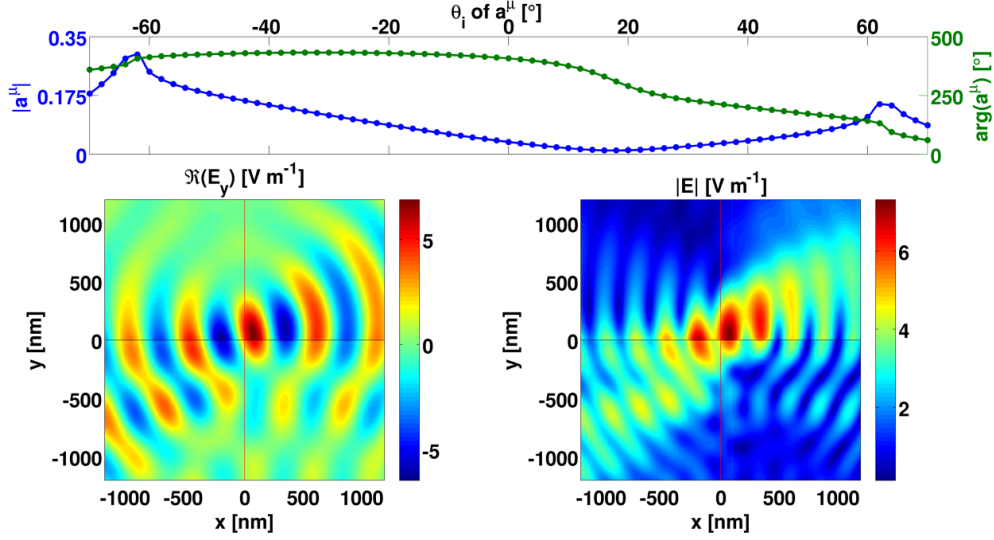


Fig. 5.4: Field optimising the force difference  $\Delta F$  for gold nanoparticles of radius  $r_1 = 50$  nm and  $r_2 = 40$  nm in a single point  $x = 0$  with corresponding amplitude  $|a^\mu|$  and phase  $\arg(a^\mu)$  for each plane wave from angular spectrum. The  $|a^\mu|$  and  $\arg(a^\mu)$  correspond to the pattern at the back focal plane of the objective. This illumination of the back focal plane forms a very strong field gradient in  $+x$  direction in the focal plane, which maximises the force difference for our testing particles. Note that scattering from the particles is not included.

optimum illumination for a ROI of any size is thus very efficient as we have to find the elements of matrices  $M_1^u$  and  $M_2^u$  in one point only.<sup>6</sup>

Optimal illumination for ROI sizes of  $l = 500$  nm (Fig. 5.5) and  $l = 5 \mu\text{m}$  (Fig. 5.6) differs significantly from the single point optimised problem (Fig. 5.4).

The optimised field corresponds in its bulk to the focusing of light into ROI. The solution is quite close to the Gaussian beam sent to the edge of the back focal plane of the objective. However, the phase for plane waves above critical angle is significantly modulated and the intensity profile is not entirely Gaussian. The width of the beam at the back-focal plane optimising the  $l = 5 \mu\text{m}$  situation is also noticeable smaller than for the case of  $l = 500$  nm. This is a direct consequence of Eq. (5.14). As we increase  $l$ , the off-diagonal terms in matrix  $\mathbf{R}_{12}^u(l)$  become less important due to the behaviour of the sinc function as  $l$  increases. In the limit  $l \rightarrow \infty$  only the diagonal terms remain. This means that the eigenmodes (eigenvectors of  $\mathbf{R}_{12}^u(l)$ ) in this case correspond to single plane waves as defined in our initial set. The eigenmode (plane wave) with maximum eigenvalue optimises our problem for an infinitely large ROI. The solution found by the FOEi method for  $l = 100$  nm (Fig. 5.7) is the plane wave near the critical angle. As the phase of  $a^\mu$  for zero amplitude  $|a^\mu|$  is not well defined, it is not displayed in the graph. The result validates that the

<sup>6</sup>The translation relation of matrices cannot be used in the direction perpendicular to the interface. In such a case, separate set of scattering problems for a particle at a higher position have to be found in order to construct the shifted matrix elements.

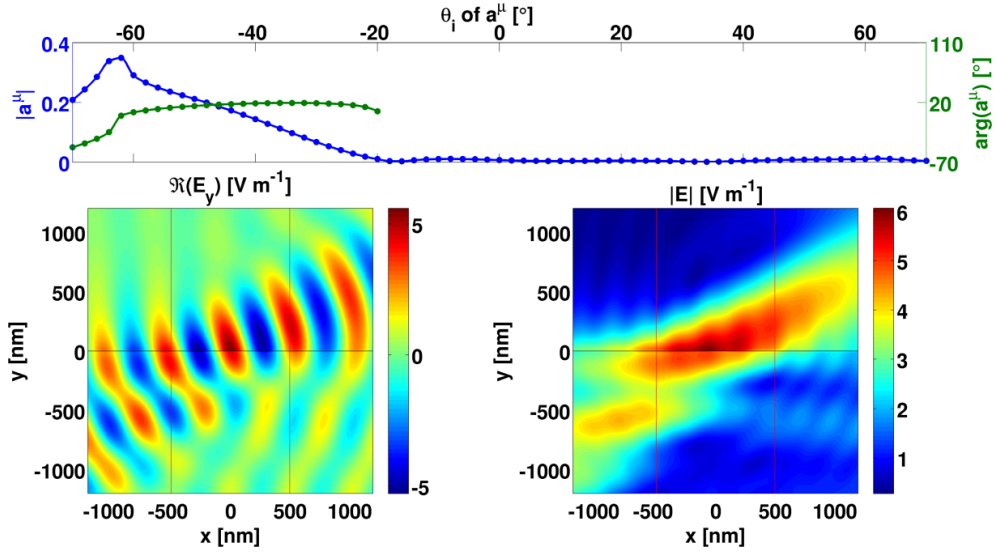


Fig. 5.5: Field optimising the force difference  $\Delta F$  for  $l = 500$  nm. The phase of  $a^\mu$  is plotted in the region where it is well-defined. Notice that the field is focused into the ROI. The left edge of the back focal plane contributes the most to the optimised field in the focal plane. The phase at the back focal plane is slightly modulated as well.

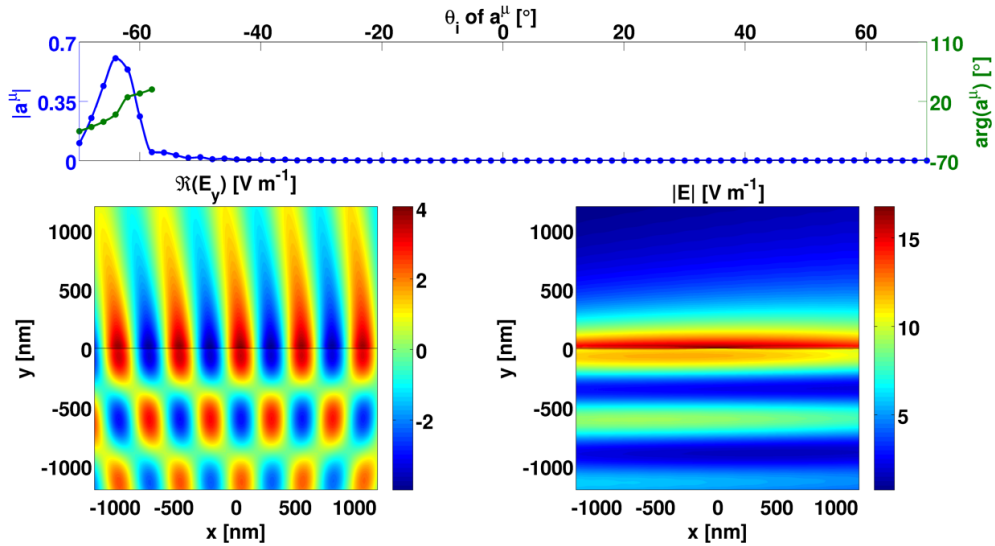


Fig. 5.6: Field optimising the force difference  $\Delta F$  for  $l = 5 \mu\text{m}$ . The shape of the beam at the back-focal plane of the objective has a narrow distribution of amplitude in the proximity of critical angle.

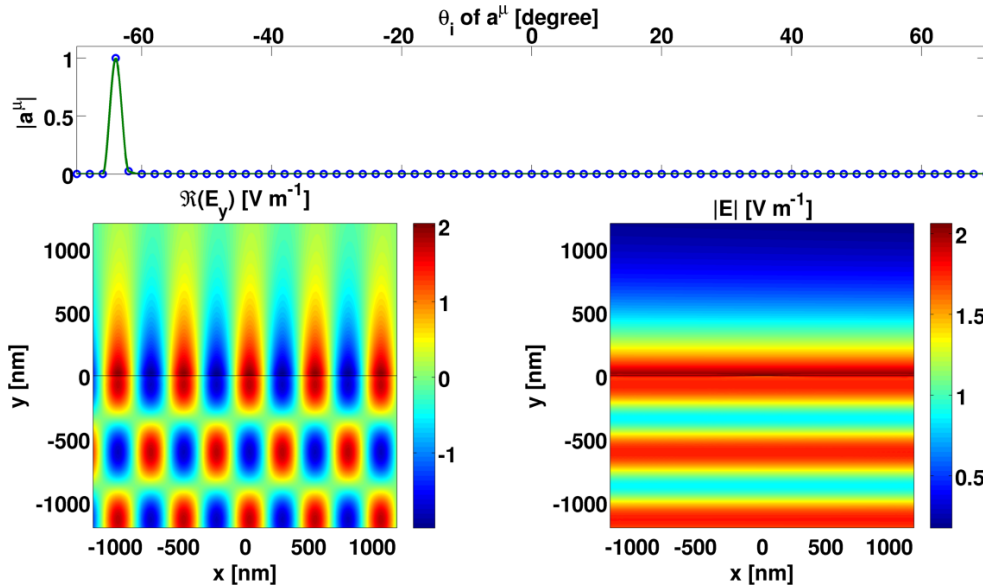


Fig. 5.7: Field optimising the force difference  $\Delta F$  for  $l \rightarrow 100$  mm. As the phase of  $a^\mu$  for zero amplitude  $|a^\mu|$  is not well defined, it is not displayed in the graph. The optimum angle plane wave is  $64^\circ$ , which is close to critical angle for given interface.

FOEi method is working correctly, as the near critical angle plane wave provides the highest intensity and force difference at the interface for infinite system.

The force difference is significantly increased in the cases of small ROI sizes compared with plane wave illuminated system that optimises the sorting for infinite sorting space (Fig. 5.8a). The bulk of this improvement is due to increased intensity of light in ROI, but the periodic pattern of forces indicates a more complex response of the system. This periodic pattern is not related to the discretisation of  $\mathbf{k}$ -space, where we expect periodicity to appear around  $14 \mu\text{m}$ .

Naturally, we do not wish the sorting ROI to become too small as the experimental realisation would become increasingly complicated. It is interesting to look at the dependence of  $\Delta F$  on the size of ROI. To show the improvement compared to infinite system, we normalise  $\Delta F$  by  $\Delta F_{pw}$ , where  $\Delta F_{pw}$  is the force difference for optimised infinite system (pw stands for plane wave). The result (Fig. 5.8b) indicates that the gain is significant for a wide range of experimentally interesting ROI sizes. The dip around  $l = 14 \mu\text{m}$  is present due to discretisation of  $\mathbf{k}$ -space described above. The increase in ratio  $\Delta F/\Delta F_{pw}$  for  $l > 14 \mu\text{m}$  is then equivalent to the formation of second beam focus in ROI due to onset of periodicity.<sup>7</sup>

## 5.5 Deflection of particles in a microfluidic channel

(Part of the section reprinted from [119]. Copyright 2011 AIP.)

<sup>7</sup>This effect is similar to the beating in acoustics. In simplest case, two plane-waves of slightly different  $\mathbf{k}$  will interfere constructively when having the same phase and this effect appears with certain periodicity.

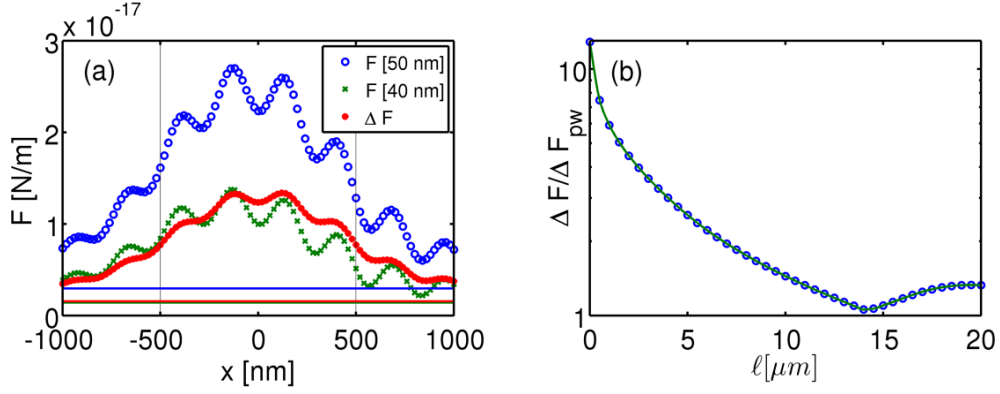


Fig. 5.8: (a) Blue and green points show forces acting on individual particles in optimised field for  $l = 500 \text{ nm}$ . Red points show the force difference. The coloured lines show the same but for plane wave illumination optimising the infinite system. (b) The ratio  $\Delta F / \Delta F_{pw}$  as a function of ROI size (logarithmic scale). The dip around  $l = 14 \mu\text{m}$  is due to  $\mathbf{k}$ -space discretisation of angular spectrum representation. The gain in  $\Delta F$  is significant in the experimentally interesting region.

The optimal beam shape can be effectively used in microfluidic channel environment to sort the particles into separate chambers. The simplified situation is shown on Fig. 5.9. Calculating the speed  $v(x)$  of particles in every point of ROI (note

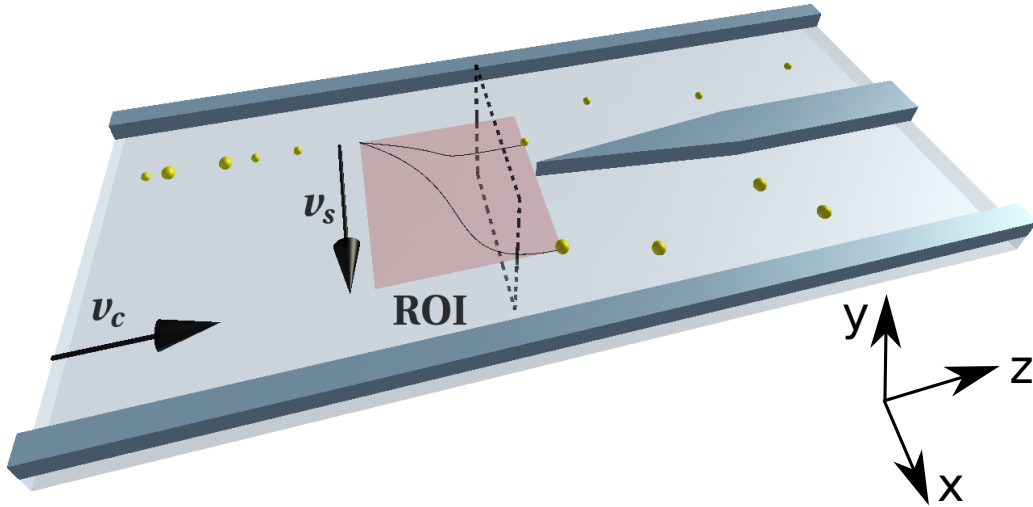


Fig. 5.9: Sorting of nanoparticles in microfluidic channel environment with laminar fluid speed of  $v_c$ . We assume that the nanoparticles are hydrodynamically focused in such a way to enter the ROI in approximately at the same position. Here the ROI is assumed to be composed of 2D cross sections (dashed square) that are equal to 2D fields calculated in previous sections. The speed difference  $\Delta v$  between nanoparticle sorting speeds  $v_s$  then results in space separation and particles continue to flow into separate chambers.

that the ROI is now a composition of 2D solutions from the previous section (see Fig. 5.9)) and solving the set of equations

$$\frac{\partial x(t)}{\partial t} = v(x(t)); \frac{\partial z(t)}{\partial t} = v_c; x(0) = z(0) = -l, \quad (5.15)$$

gives the particle trajectories in ROI. Here, the  $v_c$  should be set in such a way that the faster particle travels across the whole ROI.

Fig. 5.10a shows the trajectories of particles for optimal beam shape calculated

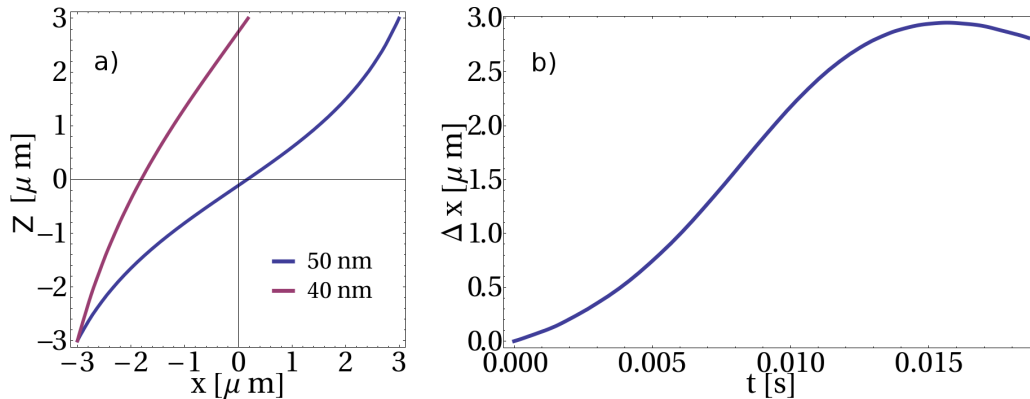


Fig. 5.10: (a) Trajectories of gold nanoparticles of different sizes in optimised fields for ROI size of  $l = 3 \mu\text{m}$ . (b) The maximum space separation of  $\Delta x = 3 \mu\text{m}$  is reached in time of 15 ms.

for ROI with  $l = 3 \mu\text{m}$ . For this ROI, the maximum space separation of  $3 \mu\text{m}$  between particles is reached in  $t = 15 \text{ ms}$  (Fig. 5.10b). The joint diffusion distance of both particles in the same amount of time is just 700 nm, which basically forbids diffusion intermixing. The optimal laminar flow speed in the channel is about  $v_c = 300 \mu\text{m/s}$  and the power density is approximately  $1 \text{ mW}/\mu\text{m}^2$ , which is both reasonable experimentally.

We note that similar approach can be adopted for integration of bidirectional sorting into microfluidic channel. Unfortunately, the current, evanescent implementation of sorting, ensures effective sorting only for particles near the interface. This means that the bulk of particles in the microfluidic channel would be unaffected by the sorting field. This restriction could be removed by introducing loosely focused counter-propagating beams with identical operating wavelengths to those in evanescent scheme. In this modified configuration, particles at any height would be influenced by the sorting field. However, the real-time particle detection would not be possible due to defocusing of the particles. In fact, the choice of the evanescent configuration was intentional as it actually proves useful for our proof of principle concept. Crucially, the confinement of particles close to surface can be used for real-time particle identification, which is based on monitoring of light intensity scattered by particle into far-field. Real-time identification of particles at a random height

would not be possible due to defocusing and subsequent change of detected intensity. Of course, one can fabricate a microfluidic channel with branches at specific positions followed by containers, which would be able to store the sorted particles. One can then use SEM images to identify the particles in respective containers. This is, however, an off-line particle identification method. We believe that the in situ and real-time detection of particle size through amount of scattering is a very powerful and practical approach with future prospects in many applications. It is also inherent to the experiment as the detection laser is also used for sorting. Nevertheless, the off-line particle identification and sorting of particles in microfluidic environment should be also possible.

## 5.6 Conclusion

The FOEi method is capable of finding the optimal beam shape for illumination such that the force difference is maximised over the whole sorting region. The computationally intensive calculation of matrices  $\mathbf{M}_1$  and  $\mathbf{M}_2$  is compensated by the fact that the same matrices can be used for finding optimal illumination for any size of sorting region. We note that even though the solution does not optimise the vertical force pointing towards the substrate, we found that this is the case for all our solutions. However, the sign of this force is wavelength and particle size dependent and as such the attractive vertical force is not a general feature of the method. Further, the vertical force is not constant in the sorting region, which might introduce some modulation of force difference due to the Faxen correction. To resolve this one may minimise the vertical force and use an auxiliary beam with constant vertical force over the whole sorting region. This would restrict the diffusion of particles in vertical direction in more controlled way. It is possible to modify the method to simultaneously optimise for several parameters of the system. In our case, the full optimised solution for sorting applications of plasmon nanoparticles would involve simultaneous maximisation of force difference in ROI, minimisation of vertical force, and minimisation of heating. Such a problem reduces to finding matrices (operators) for all parameters of interest and choosing the eigenmodes optimising for such a set of parameters. It is very interesting, for plasmonic sorting in general, to find the beam shape of the field maximising the force difference and minimising the heating. This would also clearly identify the contribution of focusing to the overall improvement of force difference. At this moment it seems that the optimised beam is very similar in shape to a Gaussian beam with a modulation of phase. However, the phase modulation is not very complex which means that the use of simple and cheap optical elements, like glass wedges, can be more economical than the use of SLM. The question thus arises whether the gain in force difference, for small phase variations not achievable by simple optical elements, offsets the high cost of the SLM in the system. The role of the small phase variations is a focus of our ongoing research.

To summarise, we have successfully optimised the illumination for sorting gold nanoparticles using our two step approach. Firstly, we found the optimal wavelength

maximising the nanoparticle separation and minimising the temperature increase in the system. This is an important consideration in plasmonic systems as the excessive heat increases diffusion and convective effects. Secondly, we have found the optimum beam shape of the illumination field for sorting using the method of force optical eigenmodes (FOEi). The applicability of the method was numerically demonstrated for the special case of sorting gold nanoparticles of different size. We plan to extend our approach and perform simultaneous optimisation of several parameters of interest for sorting applications, e.g., minimised heating, maximised force difference along substrate and maximised (minimised) vertical force. This involves finding operators for all of parameters of interest and choosing the eigenmodes optimising them. This will be subject of further work along with the efficient extension of the FOEi method to 3D case. We also plan to apply the FOEi method to the optimisation of bidirectional sorting scheme presented in Chapter 4. The plan includes calculation of far-field illumination optimising the near-field for both - the simple case of glass-water interface and also for the more complex multi-layered system of glass, gold and water.



# Chapter 6

## Summary and Outlook

This thesis investigated the advantages and possible disadvantages of utilising the plasmon resonances for optical manipulation of nanoscale objects. The thesis provided a brief general introduction into the phenomenon of plasmon resonance in Chapter 1. This was followed, in Chapter 2, by detailed discussion of the role of plasmon resonance for light confinement into sub-diffraction volume. Such a strong field confinement was shown to be imperative in any application attempting to trap nanoscale objects at reasonable incident intensities. Unfortunately, such a strong field confinement is accompanied by inevitable heating of nanostructures that generate the field confinement and this represents a serious obstacle for any trapping application.

The intriguing interplay between the strong field confinement and related heating of the system was a motivation for theoretical research presented in Chapter 3. This chapter explored the optical forces, acting on a dielectric nanosphere, in the near-field of resonant nanoantenna. The calculations of the optical forces, based on the Maxwell stress tensor approach, revealed relatively weak optical forces for incident powers presented in Ref. [4]. The optical potential well generated by the near-field of the resonant nanoantenna was, in fact, only a fraction of the thermal energy ( $k_B T$ ), which precludes the possibility of stable optical trap. On the other hand, the increase of incident power yielding deeper potential well, is accompanied by strong heating effects [6], including bubble formation for certain threshold incident intensity. This suggest that the observed trapping in Ref. [4] was due to means other than optical forces. The heating induced convection and thermophoresis, chemical binding, or surface roughness induced field enhancement might be the possible alternative explanations of the first trapping experiments using plasmonic nanostructures.

In the mean-time, the new trapping experiments using plasmonic nanostructures significantly reduced the generated heat by integrating a heat-sink [6], made of gold and copper layer, underneath the nanostructure. This research, partially inspired by our rather negative results regarding the very weak optical forces near a nanoantenna [5], represents one of the most significant steps in plasmonic trapping so far and provides a working, all-optical nanotweezer based on the plasmon resonance.

We also believe that the exciting and complex interplay between electromagnetism, thermodynamics and mechanics in plasmonic tweezing applications will maintain a high level of research interest in this area for years to come.

Chapter 4 of the thesis studies the optical effects of plasmon resonances for a fundamentally different application - size-based optical sorting of gold nanoparticles. Here, the plasmon resonances are not utilised for sub-diffraction light confinement but rather for their ability to increase the apparent cross-section of the particles for their respective resonant sizes. Exploiting these resonances, we realise sorting in a system of two counter-propagating evanescent waves, each at different wavelength that selectively guide gold nanoparticles of different sizes in opposite directions. The method was experimentally demonstrated for bidirectional sorting of gold nanoparticles of either 150 or 130 nm in diameter from those of 100 nm in diameter within a mixture. The research presented in Chapter 4 is the first experimental realisation of size-based optical sorting of metal nanoparticles. To date, optical sorting realisations have mainly focused on dielectric particles or cells, largely at the micron size scale with only a few theoretical studies [109,110] exploring the possibility to extend the range of this powerful method to the case of plasmonic nanoparticles such as gold and silver. And since the optical forces acting on metallic nanoparticles vary significantly with particle properties such as size and composition, particularly when close to plasmon resonance conditions, there was an opportunity for optical sorting utilising this behaviour. Furthermore, our method, based on the resonant behaviour related strongly to the particle size, has a promise to deliver better resolution of the sizes simply because of the utilisation of the intrinsic resonant property. This might be a major advantage over methods such as sedimentation or centrifugation that rely solely on the differentiation of the actual geometrical size.

Our sorting technique is based on the red-shift of the plasmon resonance with increasing particle size. As a result, smaller nanoparticles predominantly interact with shorter wavelengths whereas larger nanoparticles are mainly influenced by longer wavelengths. Selecting the optimal wavelengths and power ratio between the counter-propagating beams we generate a force field within the illuminated region that guides nanoparticles of different sizes in opposite directions to one another, thus realising sorting. The presented configuration extends optical sorting methods to the distinct case of plasmonic nanoparticles and size scales typically one order of magnitude lower than previously realised with dielectric objects [10,105–108].

The importance of the presented optical sorting method lies in the fact that gold nanoparticles are used for an exceptionally wide range of biomedical applications [71]. They are commonly employed for Surface Enhanced Raman Spectroscopy (SERS) and as fluorescence enhancers in various applications - e.g. intracellular biochemical composition imaging [72], DNA and RNA detection [73] and tumor targeting [74]. Additionally, they are used as mechanical carriers through cell membranes for DNA and drug delivery [75] and as localised heaters for photothermal therapy [76]. Crucially, gold nanoparticles show immense promise for multimodal biomedical applications [77] - e.g. mechanical delivery with subsequent biochemical sensing and imaging. In all these cases, the physical shape and size of the gold

nanoparticles dictate their performance. For example, size is a crucial parameter for the cell uptake rate of gold nanoparticles as mechanical carriers [78,79], the intensity of a SERS signal [80,81], the biochemical [82], optical [83] and toxicity [84] properties of nanoparticles. It is thus necessary to tailor this parameter to a high degree of accuracy for each specific application. This results in a burgeoning need for size selective controlled separation and manipulation of gold nanoparticles in solution.

The resolution of the method, in its current implementation, suffers from significant diffusion in the direction of the fading evanescent field. However, various approaches exist for reducing this diffusion to improve the technique. For example, we can decrease the diffusion by using a weakly focused non-resonant auxiliary laser to push nanoparticles towards the glass-water interface. Alternatively, coating the substrate with nanolayer of gold or the use of a dielectric resonator [50] may significantly enhance the gradient forces attracting the nanoparticle to the surface. In the case of a gold layer, the coupling of surface plasmon polaritons into gold layer would increase both the intensity of field at the interface and the gradient force attracting the particles towards the interface [113,114]. Intriguingly, the coupling between surface plasmon polaritons within the gold layer and localised surface plasmon supported by the nanoparticle might also offer additional degrees of freedom for tailoring the sensitivity of optical force to particle size. Finally an improvement of particle confinement is also possible through the use of shaped light fields [115] or standing wave traps [116].

The investigation of optimal beam-shape for optical sorting [115], presented in Chapter 5, concludes the thesis. The developed theoretical framework, based on the force optical eigenmode method, is able to find an illumination of the back-focal plane of the objective such that the force difference between nanoparticles of various sizes, in the sample plane, is maximised. We plan to extend our approach and perform simultaneous optimisation of several parameters of interest for sorting applications, e.g., minimised heating, maximised force difference along substrate and maximised (minimised) vertical force. This involves finding operators for all of parameters of interest and choosing the eigenmodes optimising them. Unfortunately, the process of simultaneous optimisation is restricted to special circumstances. For example, the considered operators have to commute. The study of these constraints will be subject of further work along with the efficient extension of the FOEi method to 3D case. If the 3D results yield a significant improvement of the force difference over the standard Gaussian beam, we also plan to apply the FOEi method to the optimisation of bidirectional sorting scheme presented in Chapter 4. The plan includes calculation of far-field illumination optimising the near-field for both - the simple case of glass-water interface and also for the more complex multi-layered system of glass, gold and water.

We firmly believe that the optical manipulation utilising plasmon resonances holds promise for a vibrant future full of exciting discoveries.



# Appendix A

## Dispersion relation of SPP mode

If we substitute Eq. (2.27) into the curl of Eq. (2.26) and use the constitutive relations we get

$$\nabla \times \nabla \times \mathbf{E}(\mathbf{r}, t) = -\frac{1}{c^2} \frac{\partial^2(\epsilon \mathbf{E}(\mathbf{r}, t))}{\partial t^2}. \quad (\text{A.1})$$

This can be further simplified by using the identity  $\nabla \times \nabla \times \mathbf{E} \equiv \nabla(\nabla \cdot \mathbf{E}) - \nabla^2 \mathbf{E}$  together with Eq. (2.28)

$$\nabla \cdot \mathbf{D} = \nabla \cdot (\epsilon \mathbf{E}) \equiv (\nabla \epsilon) \cdot \mathbf{E} + \epsilon \nabla \cdot \mathbf{E} = 0. \quad (\text{A.2})$$

In the course of this thesis, we will only be concerned with piecewise homogeneous media which means that we can set  $\nabla \epsilon(\mathbf{r}) = 0$ . As a result, Eq. (A.1) can be cast into a well-known wave equation

$$\nabla^2 \mathbf{E}(\mathbf{r}, t) - \frac{\epsilon}{c^2} \frac{\partial^2 \mathbf{E}(\mathbf{r}, t)}{\partial t^2} = 0. \quad (\text{A.3})$$

We can match the solutions of this equation in respective piecewise media by using appropriate boundary conditions. Finally, assuming time-harmonic solutions  $e^{i\omega t}$  (no transient effects) leads to the Helmholtz equation for the electric field  $\mathbf{E}$ :

$$\nabla^2 \mathbf{E}(\mathbf{r}, \omega) + k_0^2 \epsilon \mathbf{E}(\mathbf{r}, \omega) = 0, \quad (\text{A.4})$$

where  $k_0 = \omega^2/c^2 = 2\pi/\lambda_0$ , where  $\lambda_0$  is the vacuum wavelength. Similarly for magnetic field  $\mathbf{H}$

$$\nabla^2 \mathbf{H}(\mathbf{r}, \omega) + k_0^2 \epsilon \mathbf{H}(\mathbf{r}, \omega) = 0. \quad (\text{A.5})$$

Function  $f$  is an eigenmode of the system if and only if the following equation is satisfied

$$\hat{A}f = bf, \quad (\text{A.6})$$

where  $\hat{A}$  can be any linear operator and  $b$  is the scaling factor. This essentially means that if we find a solution to the Helmholtz equation, then this solution is naturally an eigenmode of the system. Let us find the solution for a situation shown in Fig. A.1.

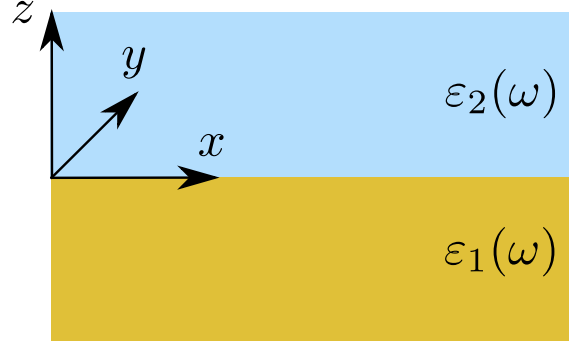


Fig. A.1: We look for a solution of Helmholtz equation (Eq. A.4) that is confined at the interface of two media. The negative half-space,  $z < 0$ , has permittivity  $\varepsilon_1$  whereas the positive half-space,  $z > 0$ , has permittivity  $\varepsilon_2$ .

The general solution of Eq. (A.4) and Eq. (A.5) in respective half-spaces is a simple plane-wave or any superposition of plane-waves. Using boundary conditions, we can match the solutions in two half-spaces and find the eigenfunction or eigenmodes of the whole space. In further discussion, we will also require this mode to be confined to interface in both half-spaces. Dropping this requirement would lead to a solution of plane-wave partially reflected and transmitted at the interface, which is not a very interesting eigenmode of the system.

We can write the solution in the first ( $j = 1$ ) and in the second ( $j = 2$ ) medium either as p-polarised plane-wave

$$\mathbf{E}_j = \begin{pmatrix} E_{j,x} \\ 0 \\ E_{j,z} \end{pmatrix} e^{-i(k_x x + k_{j,z} z - \omega t)}, \quad (\text{A.7})$$

or as s-polarised plane-wave

$$\mathbf{E}_j = \begin{pmatrix} 0 \\ E_{j,y} \\ 0 \end{pmatrix} e^{-i(k_x x + k_{j,z} z - \omega t)}, \quad (\text{A.8})$$

where  $k_x$  is the same in both media (consequence of Snell's law). It is useful, for further analysis, to express the solution for s-polarised plane-wave in terms of the magnetic field. Using Eq. (2.26) we get

$$\mathbf{H}_j = \frac{1}{\omega \mu_0} \begin{pmatrix} -k_{j,z} E_{j,y} \\ 0 \\ k_x E_{j,y} \end{pmatrix} e^{-i(k_x x + k_{j,z} z - \omega t)}. \quad (\text{A.9})$$

Let us first study the case of s-polarised plane-waves. Inserting Eq. (A.9) back into Eq. (A.5) results in the following relation for wave-vectors

$$k_x^2 + k_{j,z}^2 = \varepsilon_j k_0^2. \quad (\text{A.10})$$

At the same time the continuity of tangential field components has to be satisfied. The condition satisfying continuity for tangential component of electric field is

$$E_{1,y} = E_{2,y}. \quad (\text{A.11})$$

Similarly the condition for continuity of tangential components of magnetic field requires

$$k_{2,z}E_{2,y} - k_{1,z}E_{1,y} = 0 \rightarrow k_{1,z} = k_{2,z}. \quad (\text{A.12})$$

At this point we can see that the conditions imposed by Eq. (A.10) and Eq. (A.12) cannot be fulfilled simultaneously since the right hand side of Eq. (A.10) is different for each medium (index  $j$ ), while, at the same time, the left hand side is required to be constant in both media. This leads to a very important result that the solution (eigenmode) at the interface does not exist for the case of s-polarised plane-waves.<sup>1</sup>

Let us now turn our attention to the case of p-polarised plane-wave. Using Eq. (2.28) for p-polarised plane-wave, given by Eq. (A.7), leads to the following set of equations

$$k_x E_{1,x} + k_{1,z} E_{1,z} = 0 \quad (\text{A.13})$$

$$k_x E_{2,x} + k_{2,z} E_{2,z} = 0 \quad (\text{A.14})$$

in medium 1 and medium 2 respectively. To satisfy the continuity of tangential electric field  $E_x$  and normal electric displacement  $D_z$ , we further require

$$E_{1,x} - E_{2,x} = 0, \quad (\text{A.15})$$

$$\varepsilon_1 E_{1,z} - \varepsilon_2 E_{2,z} = 0. \quad (\text{A.16})$$

This set of equations represents a homogeneous system of four equations for unknown electric field. The non-trivial solution exists only if the determinant of the following matrix is zero

$$\begin{vmatrix} k_x & 0 & k_{1,z} & 0 \\ 0 & k_x & 0 & k_{2,z} \\ 1 & -1 & 0 & 0 \\ 0 & 0 & \varepsilon_1 & -\varepsilon_2 \end{vmatrix} = k_x(k_{1,z}\varepsilon_2 - k_{2,z}\varepsilon_1), \quad (\text{A.17})$$

which is fulfilled either for the trivial case of  $k_x = 0$  or for a condition  $k_{1,z}\varepsilon_2 - k_{2,z}\varepsilon_1 = 0$ . This condition, together with Eq. (A.10), which is also valid for the case of p-polarised plane-wave, leads to the following dispersion relations for the existing mode

$$k_x^2 = \frac{\varepsilon_1 \varepsilon_2}{\varepsilon_1 + \varepsilon_2} \frac{\omega^2}{c^2}, \quad (\text{A.18})$$

$$k_{j,z}^2 = \frac{\varepsilon_j^2}{\varepsilon_1 + \varepsilon_2} \frac{\omega^2}{c^2}. \quad (\text{A.19})$$

---

<sup>1</sup>The solution for s-polarised plane-wave can only be found by adding reflected wave to Eq. (A.9), however, such a change leads to a solution that is not confined at the interface and thus cannot represent an interface confined mode.

Let us now derive the necessary conditions for the existence of the interface confined mode. Let us assume for simplicity that the imaginary parts of the complex permittivities  $\varepsilon_1, \varepsilon_2$  are very small. We are looking for an interface mode that is confined to the interface in both half-spaces and at the same time propagates along the x-axis. This requires a real  $k_x$  and a purely imaginary  $k_{j,z}$ . The necessary condition for an interface mode to exist thus requires the following constraints on the respective permittivities  $\varepsilon_1, \varepsilon_2$ :

$$\varepsilon_1(\omega) \cdot \varepsilon_2(\omega) < 0, \quad \varepsilon_1(\omega) + \varepsilon_2(\omega) < 0, \quad (\text{A.20})$$

which basically means that the values of permittivity  $\varepsilon_1, \varepsilon_2$  need to have opposite sign and the absolute value of negative permittivity has to be larger than the absolute value of the positive one. This is indeed possible for the case of metal (negative permittivity in the optical range for gold) and dielectric. The surface confined mode can thus exist. We would like to note that if we allow for real valued perpendicular wavevectors then the derived dispersion relations simply describe the Brewster effect.

We can also cast Eq. (A.18) and Eq. (A.19) into a form used for interpretation of some of the results contained within the thesis

$$k_x = \sqrt{\frac{\varepsilon_1 \varepsilon_2}{\varepsilon_1 + \varepsilon_2}} \frac{\omega}{c}, \quad (\text{A.21})$$

$$k_{j,z} = -\sqrt{\frac{\varepsilon_j^2}{\varepsilon_1 + \varepsilon_2}} \frac{\omega}{c}. \quad (\text{A.22})$$

Here, the minus sign in Eq. (A.22) was selected because the solution without the minus sign corresponds to diverging field solution in the z-direction.

# Appendix B

## Derivation of LSPP mode

We want to find a solution of Laplace equation

$$\nabla^2\Phi = 0. \quad (\text{B.1})$$

for a spherical nanoparticle and it is thus convenient to solve this equation in spherical coordinates

$$\frac{1}{r^2 \sin \theta} \left[ \sin \theta \frac{\partial}{\partial r} \left( r^2 \frac{\partial}{\partial r} \right) + \frac{\partial}{\partial \theta} \left( \sin \theta \frac{\partial}{\partial \theta} \right) + \frac{1}{\sin \theta} \frac{\partial^2}{\partial \varphi^2} \right] \Phi(r, \theta, \varphi) = 0. \quad (\text{B.2})$$

The above equation can be solved by the method of separation of variables.

Let us solve this equation for the specific case of gold sphere (permittivity given by  $\varepsilon_1$ ) of radius  $a$  located in a uniform electric field  $\mathbf{E}_0 = E_0 \hat{z}$  in water (permittivity given by  $\varepsilon_2$ ) (Fig. B.1). The applied field  $\mathbf{E}_0$  induces a charge distribution

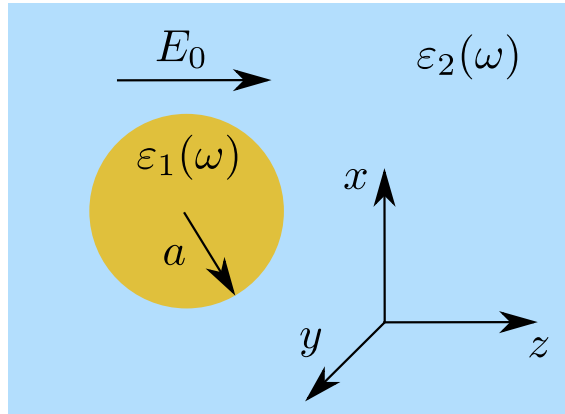


Fig. B.1: The gold sphere of radius  $a$  with permittivity  $\varepsilon_1(\omega)$  surrounded with water ( $\varepsilon_2$ ) is exposed to electrostatic field given by  $\mathbf{E}_0 = E_0 \hat{z}$ .

in the sphere that maintains azimuthal symmetry of the problem. The separation of variables in such a symmetric case leads to the following general solution for the

electrostatic potential

$$\Phi(r, \theta) = \sum_{l=0}^{\infty} [A_l r^l + B_l r^{-l-1}] P_l(\cos \theta), \quad (\text{B.3})$$

where  $P_l(\cos \theta)$  are the Legendre polynomials. Since the potential  $\Phi$  needs to be finite inside the sphere<sup>1</sup>, we can write the potential inside and outside of the sphere as

$$\Phi_1 = \sum_{l=0}^{\infty} A_l r^l P_l(\cos \theta), \quad (\text{B.4})$$

$$\Phi_2 = \sum_{l=0}^{\infty} [C_l r^l + D_l r^{-l-1}] P_l(\cos \theta). \quad (\text{B.5})$$

Let us now determine the coefficients  $A_l$ ,  $C_l$  and  $D_l$ . At a large distance from the sphere  $r \rightarrow \infty$ , potential  $\Phi_2$  should be unaffected by the presence of the sphere. The potential should thus converge to  $\Phi_2 \rightarrow -E_0 z = -E_0 r \cos \theta$ . As a result,  $C_l = 0$  for  $l \neq 1$  and  $C_l = -E_0$  for  $l = 1$ . We further require continuity of tangential components of the electric field and the continuity of the normal components of the electric displacement at the surface of the sphere ( $r = a$ )

$$\left. \frac{\partial \Phi_1}{\partial \theta} \right|_{r=a} = \left. \frac{\partial \Phi_2}{\partial \theta} \right|_{r=a}, \quad (\text{B.6})$$

$$\varepsilon_1 \left. \frac{\partial \Phi_1}{\partial r} \right|_{r=a} = \varepsilon_2 \left. \frac{\partial \Phi_2}{\partial r} \right|_{r=a}. \quad (\text{B.7})$$

For  $l \neq 1$  this leads to the following set of equations

$$A_l a^l = D_l a^{-l-1}, \quad A_l l a^{l-1} + \frac{\varepsilon_2}{\varepsilon_1} D_l (l+1) a^{-l-2} = 0, \quad (\text{B.8})$$

which has a solution only if  $A_l = D_l = 0$ . For the case  $l = 1$  we get

$$A_1 a = -E_0 a + D_1 a^{-2}, \quad A_1 = \frac{\varepsilon_2}{\varepsilon_1} (-E_0 - 2D_1 a^{-3}), \quad (\text{B.9})$$

which gives the following coefficients

$$D_1 = E_0 a^3 \frac{\varepsilon_1 - \varepsilon_2}{\varepsilon_1 + 2\varepsilon_2}, \quad A_1 = -E_0 \frac{3\varepsilon_2}{\varepsilon_1 + 2\varepsilon_2}. \quad (\text{B.10})$$

Inserting the calculated coefficients back into Eq. (B.4) and Eq. (B.5) gives the following electrostatic potentials inside and outside of the sphere

$$\Phi_1 = -\frac{3\varepsilon_2}{\varepsilon_1 + 2\varepsilon_2} E_0 r \cos \theta, \quad (\text{B.11})$$

$$\Phi_2 = -E_0 r \cos \theta + \frac{\varepsilon_1 - \varepsilon_2}{\varepsilon_1 + 2\varepsilon_2} E_0 a^3 \frac{\cos \theta}{r^2}. \quad (\text{B.12})$$

---

<sup>1</sup>The potential  $\Phi$  can be infinite outside of the sphere.

We can easily transform these potential equations into the Cartesian coordinate system using  $z = r \cos \theta$  which finally results in

$$\Phi_1 = -\frac{3\varepsilon_2}{\varepsilon_1 + 2\varepsilon_2} E_0 z, \quad (\text{B.13})$$

$$\Phi_2 = -E_0 z + \frac{\varepsilon_1 - \varepsilon_2}{\varepsilon_1 + 2\varepsilon_2} E_0 a^3 \frac{z}{r^3}. \quad (\text{B.14})$$



## BIBLIOGRAPHY

- [1] P. R. West, S. Ishii, G. V. Naik, N. K. Emani, V. M. Shalaev, and A. Boltasseva. Searching for better plasmonic materials. *Laser and Photonics Reviews*, 4(6):795–808, 2010.
- [2] F. H. L. Koppens, D. E. Chang, and F. J. García de Abajo. Graphene Plasmonics: A Platform for Strong Light-Matter Interactions. *Nano Letters*, 11(8):3370–3377, 2011.
- [3] S. A. Maier. *Plasmonics: Fundamentals and Applications*. Springer, 2007.
- [4] M. Righini, P. Ghenuche, S. Cherukulappurath, V. Myroshnychenko, F. J. García de Abajo, and R. Quidant. Nano-optical Trapping of Rayleigh Particles and Escherichia coli Bacteria with Resonant Optical Antennas. *Nano Letters*, 9(10):3387–3391, 2009.
- [5] M. Plöschner, M. Mazilu, T. F. Krauss, and K. Dholakia. Optical forces near a nanoantenna. *Journal of Nanophotonics*, 4:041570, 2010.
- [6] K. Wang, E. Schonbrun, P. Steinvurzel, and K. B. Crozier. Trapping and rotating nanoparticles using a plasmonic nano-tweezer with an integrated heat sink. *Nature Communications*, 2, 2011.
- [7] S. Noda, M. Fujita, and T. Asano. Spontaneous-emission control by photonic crystals and nanocavities. *Nature Photonics*, 1(8):449–458, 2007.
- [8] M. Kuttge, F. J. García de Abajo, and A. Polman. Ultrasmall mode volume plasmonic nanodisk resonators. *Nano Letters*, 10(5):1537–1541, 2010.
- [9] N. Liu, L. Langguth, T. Weiss, J. Kastel, M. Fleischhauer, T. Pfau, and H. Giessen. Plasmonic analogue of electromagnetically induced transparency at the Drude damping limit. *Nature Materials*, 8(9):758–762, 2009.
- [10] T. Čižmár, M. Šiler, M. Šerý, P. Zemánek, V. Garcés-Chavéz, and K. Dholakia. Optical sorting and detection of submicrometer objects in a motional standing wave. *Physical Review B*, 74(3):035105, 2006.
- [11] K. Svoboda, C. F. Schmidt, B. J. Schnapp, and S. M. Block. Direct observation of kinesin stepping by optical trapping interferometry. *Nature*, 365(6448):721–727, 1993.

- [12] M. D. Wang, H. Yin, R. Landick, J. Gelles, and S. M. Block. Stretching DNA with optical tweezers. *Biophysical Journal*, 72(3):1335–1346, 1997.
- [13] M. Kerker. *The scattering of light and other electromagnetic radiation*. Academic Press, 1969.
- [14] L. Novotny and B. Hecht. *Principles of Nano-Optics*. Cambridge University Press, 2006.
- [15] M. Dienerowitz, M. Mazilu, P. J. Reece, T. F. Krauss, and K. Dholakia. Optical vortex trap for resonant confinement of metal nanoparticles. *Opt. Express*, 16(7):4991–4999, 2008.
- [16] A. E. Siegman. *Lasers*. University Science Books, 1986.
- [17] A. Einstein. Über die von der molekularkinetischen Theorie der Wärme geforderte Bewegung von in ruhenden Flüssigkeiten suspendierten Teilchen. *Annalen der Physik*, 322(8):549–560, 1905.
- [18] A. Ashkin, J. M. Dziedzic, J. E. Bjorkholm, and S. Chu. Observation of a single-beam gradient force optical trap for dielectric particles. *Optics Letters*, 11(5):288–290, 1986.
- [19] G. Raschke, S. Kowarik, T. Franzl, C. Sonnichsen, T. A. Klar, J. Feldmann, A. Nichtl, and K. Kurzinger. Biomolecular recognition based on single gold nanoparticle light scattering. *Nano Letters*, 3(7):935–938, 2003.
- [20] J. Homola, S. S. Yee, and G. Gauglitz. Surface plasmon resonance sensors: review. *Sensors and Actuators B-Chemical*, 54(1-2):3–15, 1999.
- [21] J. N. Anker, W. P. Hall, O. Lyandres, N. C. Shah, J. Zhao, and R. P. Van Duyne. Biosensing with plasmonic nanosensors. *Nature Materials*, 7(6):442–453, 2008.
- [22] J. Stehr, C. Hrelescu, R. A. Sperling, G. Raschke, M. Wunderlich, A. Nichtl, D. Heindl, K. Kurzinger, W. J. Parak, T. A. Klar, and J. Feldmann. Gold nanostoves for microsecond DNA melting analysis. *Nano Letters*, 8(2):619–623, 2008.
- [23] P. K. Jain, I. H. El-Sayed, and M. A. El-Sayed. Au nanoparticles target cancer. *Nano Today*, 2(1):18–29, 2007.
- [24] R. F. Oulton, V. J. Sorger, D. A. Genov, D. F. P. Pile, and X. Zhang. A hybrid plasmonic waveguide for subwavelength confinement and long-range propagation. *Nature Photonics*, 2(8):496–500, 2008.
- [25] S. Lal, S. Link, and N. J. Halas. Nano-optics from sensing to waveguiding. *Nature Photonics*, 1(11):641–648, 2007.

- [26] J. A. Dionne, L. A. Sweatlock, H. A. Atwater, and A. Polman. Plasmon slot waveguides: Towards chip-scale propagation with subwavelength-scale localization. *Physical Review B*, 73(3), 2006.
- [27] S. I. Bozhevolnyi, J. Erland, K. Leosson, P. M. W. Skovgaard, and J. M. Hvam. Waveguiding in surface plasmon polariton band gap structures. *Physical Review Letters*, 86(14):3008–3011, 2001.
- [28] F. J. Garcia-Vidal, L. Martin-Moreno, and J. B. Pendry. Surfaces with holes in them: new plasmonic metamaterials. *Journal of Optics a-Pure and Applied Optics*, 7(2):S97–S101, 2005.
- [29] J. Henzie, M. H. Lee, and T. W. Odom. Multiscale patterning of plasmonic metamaterials. *Nature Nanotechnology*, 2(9):549–554, 2007.
- [30] S. A. Maier, M. L. Brongersma, P. G. Kik, S. Meltzer, A. A. G. Requicha, and H. A. Atwater. Plasmonics - a route to nanoscale optical devices. *Advanced Materials*, 13(19):1501–+, 2001.
- [31] P. Anger, P. Bharadwaj, and L. Novotny. Enhancement and quenching of single-molecule fluorescence. *Physical Review Letters*, 96(11), 2006.
- [32] K. Kneipp, Y. Wang, H. Kneipp, L. T. Perelman, I. Itzkan, R. Dasari, and M. S. Feld. Single molecule detection using surface-enhanced Raman scattering (SERS). *Physical Review Letters*, 78(9):1667–1670, 1997.
- [33] S. M. Nie and S. R. Emery. Probing single molecules and single nanoparticles by surface-enhanced Raman scattering. *Science*, 275(5303):1102–1106, 1997.
- [34] A. N. Grigorenko, N. W. Roberts, M. R. Dickinson, and Y. Zhang. Nanometric optical tweezers based on nanostructured substrates. *Nature Photonics*, 2(6):365–370, 2008.
- [35] Ch. Chen, M. L. Juan, Y. Li, G. Maes, G. Borghs, P. Van Dorpe, and R. Quidant. Enhanced optical trapping and arrangement of nano-objects in a plasmonic nanocavity. *Nano Letters*, 12(1):125–132, 2012.
- [36] V. Garcés-Chavéz, R. Quidant, P. J. Reece, G. Badenes, L. Torner, and K. Dholakia. Extended organization of colloidal microparticles by surface plasmon polariton excitation. *Physical Review B*, 73(8), 2006.
- [37] M. L. Juan, R. Gordon, Y. Pang, F. Eftekhari, and R. Quidant. Self-induced back-action optical trapping of dielectric nanoparticles. *Nature Physics*, 5(12):915–919, 2009.
- [38] M. L. Juan, M. Righini, and R. Quidant. Plasmon nano-optical tweezers. *Nature Photonics*, 5(6):349–356, 2011.

- [39] Y. Pang and R. Gordon. Optical trapping of 12 nm dielectric spheres using double-nanoholes in a gold film. *Nano Letters*, 11(9):3763–3767, 2011.
- [40] Y. Pang and R. Gordon. Optical trapping of a single protein. *Nano Letters*, 12(1):402–406, 2012.
- [41] M. Righini, G. Volpe, Ch. Girard, D. Petrov, and R. Quidant. Surface plasmon optical tweezers: Tunable optical manipulation in the femtonewton range. *Physical Review Letters*, 100(18), 2008.
- [42] M. Righini, A. S. Zelenina, Ch. Girard, and R. Quidant. Parallel and selective trapping in a patterned plasmonic landscape. *Nature Physics*, 3(7):477–480, 2007.
- [43] B. J. Roxworthy, K. D. Ko, A. Kumar, K. H. Fung, E. K. C. Chow, G. L. Liu, N. X. Fang, and Jr. Toussaint, K. C. Application of Plasmonic Bowtie Nanoantenna Arrays for Optical Trapping, Stacking, and Sorting. *Nano Letters*, 12(2):796–801, 2012.
- [44] K. Wang, E. Schonbrun, P. Steinvurzel, and K. B. Crozier. Scannable plasmonic trapping using a gold stripe. *Nano Letters*, 10(9):3506–3511, 2010.
- [45] W. Zhang, L. Huang, Ch. Santschi, and O. J. F. Martin. Trapping and sensing 10 nm metal nanoparticles using plasmonic dipole antennas. *Nano Letters*, 10(3):1006–1011, 2010.
- [46] P. B. Johnson and R. W. Christy. Optical-constants of noble-metals. *Physical Review B*, 6(12):4370–4379, 1972.
- [47] T. W. Ebbesen, H. J. Lezec, H. F. Ghaemi, T. Thio, and P. A. Wolff. Extraordinary optical transmission through sub-wavelength hole arrays. *Nature*, 391(6668):667–669, 1998.
- [48] J. Pendry. Applied physics - playing tricks with light. *Science*, 285(5434):1687–1688, 1999.
- [49] M. Born and E. Wolf. *Principles of Optics*. Cambridge University Press, 1997.
- [50] P. J. Reece, V. Garcés-Chavéz, and K. Dholakia. Near-field optical micromanipulation with cavity enhanced evanescent waves. *Applied Physics Letters*, 88(22):221116, 2006.
- [51] A. H. J. Yang, S. D. Moore, B. S. Schmidt, M. Klug, M. Lipson, and D. Erickson. Optical manipulation of nanoparticles and biomolecules in sub-wavelength slot waveguides. *Nature*, 457(7225):71–75, 2009.
- [52] F. Fornel. *Evanescent Waves: From Newtonian Optics To Atomic Optics*. Springer, 2001.

- [53] L. Huang, S. J. Maerkl, and O. J. F. Martin. Integration of plasmonic trapping in a microfluidic environment. *Opt. Express*, 17(8):6018–6024, 2009.
- [54] Y. Seol, A. E. Carpenter, and T. T. Perkins. Gold nanoparticles: enhanced optical trapping and sensitivity coupled with significant heating. *Optics Letters*, 31(16):2429–2431, 2006.
- [55] H. Fischer and O. J. F. Martin. Engineering the optical response of plasmonic nanoantennas. *Optics Express*, 16(12):9144–9154, 2008.
- [56] J. D. Jackson. *Classical Electrodynamics*. John Wiley & Sons, Inc., 1999.
- [57] M. I. Mishchenko, L. D. Travis, and D. W. Mackowski. T-matrix computations of light scattering by nonspherical particles: A review. *Journal of Quantitative Spectroscopy and Radiative Transfer*, 55(5):535–575, 1996.
- [58] J. P. Berenger. A perfectly matched layer for the absorption of electromagnetic waves. *Journal of Computational Physics*, 114:185, 1994.
- [59] A. Taflov and S. C. Hagness. *Computational Electrodynamics: The Finite-Difference Time-Domain method*. Artech House, Boston, 2000.
- [60] B. Goldberg. New computations of the Mie scattering functions for spherical particles. *J. Opt. Soc.*, 43:1221, 1953.
- [61] C. Schalen. *Uppsala Astr. Observ. Ann*, 1(9), 1945.
- [62] M. W. Knight and N. J. Halas. Nanoshells to nanoeggs to nanocups, optical properties of reduced symmetry core-shell nanoparticles beyond the quasistatic limit. *New Journal of Physics*, 10:105006, 2008.
- [63] T. A. Nieminen, V. L. Y. Loke, A. B. Stilgoe, G. Knoener, A. M. Branczyk, N. R. Heckenberg, and H. Rubinsztein-Dunlop. Optical tweezers computational toolbox. *Journal of Optics a-Pure and Applied Optics*, 9(8):S196–S203, 2007.
- [64] D. C. Marinica, A. K. Kazansky, P. Nordlander, J. Aizpurua, and A. G. Borisov. Quantum plasmonics: Nonlinear effects in the field enhancement of a plasmonic nanoparticle dimer. *Nano Letters*, 12(3):1333–1339, 2012.
- [65] G. Baffou, R. Quidant, and C. Girard. Heat generation in plasmonic nanostructures: Influence of morphology. *Applied Physics Letters*, 94(15):153109, 2009.
- [66] D. Braun and A. Libchaber. Trapping of DNA by thermophoretic depletion and convection. *Physical Review Letters*, 89(18), 2002.
- [67] J. Arines and J. Ares. Minimum variance centroid thresholding. *Optics Letters*, 27(7):497–499, 2002.

- [68] Z. Zhang and Ch. Menq. Three-dimensional particle tracking with subnanometer resolution using off-focus images. *Applied Optics*, 47(13):2361–2370, 2008.
- [69] M. Plöschner, T. Čižmár, M. Mazilu, A. Di Falco, and K. Dholakia. Bidirectional optical sorting of gold nanoparticles. *Nano letters*, 12(4):1923–7, 2012.
- [70] V. Myroshnychenko, J. Rodriguez-Fernandez, I. Pastoriza-Santos, A. M. Funston, C. Novo, P. Mulvaney, L. M. Liz-Marzan, and F. J. García de Abajo. Modelling the optical response of gold nanoparticles. *Chemical Society Reviews*, 37(9):1792–1805, 2008.
- [71] A. S. Thakor, J. Jokerst, C. Zavaleta, T. F. Massoud, and S. S. Gambhir. Gold nanoparticles: A revival in precious metal administration to patients. *Nano Letters*, 11(10):4029–4036, 2011.
- [72] J. Ando, K. Fujita, N. I. Smith, and S. Kawata. Dynamic SERS imaging of cellular transport pathways with endocytosed gold nanoparticles. *Nano Letters*, 11(12):5344–5348, 2011.
- [73] Y. W. C. Cao, R. C. Jin, and C. A. Mirkin. Nanoparticles with Raman spectroscopic fingerprints for DNA and RNA detection. *Science*, 297(5586):1536–1540, 2002.
- [74] X. Qian, X. Peng, D. O. Ansari, Q. Yin-Goen, G. Z. Chen, D. M. Shin, L. Yang, A. N. Young, M. D. Wang, and S. Nie. In vivo tumor targeting and spectroscopic detection with surface-enhanced Raman nanoparticle tags. *Nature Biotechnology*, 26(1):83–90, 2008.
- [75] G. F. Paciotti, L. Myer, D. Weinreich, D. Goia, N. Pavel, R. E. McLaughlin, and L. Tamarkin. Colloidal gold: A novel nanoparticle vector for tumor directed drug delivery. *Drug Delivery*, 11(3):169–183, 2004.
- [76] A. M. Gobin, M. H. Lee, N. J. Halas, W. D. James, R. A. Drezek, and J. L. West. Near-infrared resonant nanoshells for combined optical imaging and photothermal cancer therapy. *Nano Letters*, 7(7):1929–1934, 2007.
- [77] J. Choi, Y. Jun, S. Yeon, H. Ch. Kim, J. Shin, and J. Cheon. Biocompatible heterostructured nanoparticles for multimodal biological detection. *Journal of the American Chemical Society*, 128(50):15982–15983, 2006.
- [78] B. D. Chithrani, A. A. Ghazani, and W. C. W. Chan. Determining the size and shape dependence of gold nanoparticle uptake into mammalian cells. *Nano Letters*, 6(4):662–668, 2006.
- [79] B. Devika Chithrani and Warren C. W. Chan. Elucidating the mechanism of cellular uptake and removal of protein-coated gold nanoparticles of different sizes and shapes. *Nano Letters*, 7(6):1542–1550, 2007.

- [80] P. K. Jain, K. S. Lee, I. H. El-Sayed, and M. A. El-Sayed. Calculated absorption and scattering properties of gold nanoparticles of different size, shape, and composition: Applications in biological imaging and biomedicine. *Journal of Physical Chemistry B*, 110(14):7238–7248, 2006.
- [81] A. M. Kern and O. J. F. Martin. Excitation and reemission of molecules near realistic plasmonic nanostructures. *Nano Letters*, 11(2):482–487, 2011.
- [82] W. Jiang, B. Y. S. Kim, J. T. Rutka, and W. C. W. Chan. Nanoparticle-mediated cellular response is size-dependent. *Nature Nanotechnology*, 3(3):145–150, 2008.
- [83] K. L. Kelly, E. Coronado, L. L. Zhao, and G. C. Schatz. The optical properties of metal nanoparticles: The influence of size, shape, and dielectric environment. *Journal of Physical Chemistry B*, 107(3):668–677, 2003.
- [84] Y. Pan, S. Neuss, A. Leifert, M. Fischler, F. Wen, U. Simon, G. Schmid, W. Brandau, and W. Jahnen-Dechent. Size-dependent cytotoxicity of gold nanoparticles. *Small*, 3(11):1941–1949, 2007.
- [85] J. Kimling, M. Maier, B. Okenve, V. Kotaidis, H. Ballot, and A. Plech. Turkevich method for gold nanoparticle synthesis revisited. *Journal of Physical Chemistry B*, 110(32):15700–15707, 2006.
- [86] G. Frens. Controlled nucleation for regulation of particle-size in monodisperse gold suspensions. *Nature-Physical Science*, 241(105):20–22, 1973.
- [87] S. D. Perrault and W. C. W. Chan. Synthesis and surface modification of highly monodispersed, spherical gold nanoparticles of 50-200 nm. *Journal of the American Chemical Society*, 131(47):17042–17043, 2009.
- [88] C. Contado and R. Argazzi. Size sorting of citrate reduced gold nanoparticles by sedimentation field-flow fractionation. *Journal of Chromatography A*, 1216(52):9088–9098, 2009.
- [89] J. P. Novak, C. Nickerson, S. Franzen, and D. L. Feldheim. Purification of molecularly bridged metal nanoparticle arrays by centrifugation and size exclusion chromatography. *Analytical Chemistry*, 73(23):5758–5761, 2001.
- [90] T. Kaneta, Y. Ishidzu, N. Mishima, and T. Imasaka. Theory of optical chromatography. *Analytical Chemistry*, 69(14):2701–2710, 1997.
- [91] M. Pelton, K. Ladavac, and D. G. Grier. Transport and fractionation in periodic potential-energy landscapes. *Physical Review E*, 70(3):031108, 2004.
- [92] K. Xiao and D. G. Grier. Multidimensional optical fractionation of colloidal particles with holographic verification. *Phys. Rev. Lett.*, 104(2):028302, 2010.

- [93] M. P. MacDonald, G. C. Spalding, and K. Dholakia. Microfluidic sorting in an optical lattice. *Nature*, 426(6965):421–424, 2003.
- [94] A. Jonáš and P. Zemánek. Light at work: The use of optical forces for particle manipulation, sorting, and analysis. *Electrophoresis*, 29(24):4813–4851, 2008.
- [95] R. F. Marchington, M. Mazilu, S. Kuriakose, V. Garcés-Chavéz, P. J. Reece, T. F. Krauss, M. Gu, and K. Dholakia. Optical deflection and sorting of microparticles in a near-field optical geometry. *Opt. Express*, 16(6):3712–3726, 2008.
- [96] D. W. Galbraith, M. T. Anderson, and L. A. Herzenberg. Flow cytometric analysis and FACS sorting of cells based on GFP accumulation. *Methods in Cell Biology*, 58:315–341, 1999.
- [97] T. N. Buican, M. J. Smyth, H. A. Crissman, G. C. Salzman, C. C. Stewart, and J. C. Martin. Automated single-cell manipulation and sorting by light trapping. *Applied Optics*, 26(24):5311–5316, 1987.
- [98] K. Grujic, O. G. Helleso, J. P. Hole, and J. S. Wilkinson. Sorting of polystyrene microspheres using a y-branched optical waveguide. *Opt. Express*, 13(1):1–7, 2005.
- [99] S. C. Chapin, V. Germain, and E. R. Dufresne. Automated trapping, assembly, and sorting with holographic optical tweezers. *Opt. Express*, 14(26):13095–13100, 2006.
- [100] P. J. Rodrigo, R. L. Eriksen, V. R. Daria, and J. Gluckstad. Interactive light-driven and parallel manipulation of inhomogeneous particles. *Opt. Express*, 10(26):1550–1556, 2002.
- [101] P. T. Korda, M. B. Taylor, and D. G. Grier. Kinetically locked-in colloidal transport in an array of optical tweezers. *Physical Review Letters*, 89(12):128301, 2002.
- [102] K. Ladavac, K. Kasza, and D. G. Grier. Sorting mesoscopic objects with periodic potential landscapes: Optical fractionation. *Physical Review E*, 70(1):010901, 2004.
- [103] G. Milne, D. Rhodes, M. MacDonald, and K. Dholakia. Fractionation of polydisperse colloid with acousto-optically generated potential energy landscapes. *Opt. Lett.*, 32(9):1144–1146, 2007.
- [104] Y. Y. Sun, L. S. Ong, and X. C. Yuan. Composite-microlens-array-enabled microfluidic sorting. *Applied Physics Letters*, 89(14):141108, 2006.
- [105] I. Ricárdez-Vargas, P. Rodríguez-Montero, R. Ramos-García, and K. Volke-Sepúlveda. Modulated optical sieve for sorting of polydisperse microparticles. *Applied Physics Letters*, 88(12):121116, 2006.

- [106] P. Jákł, T. Čiřmár, M. řerý, and P. Zemáne. Static optical sorting in a laser interference field. *Applied Physics Letters*, 92(16):161110, 2008.
- [107] L. Paterson, E. Papagiakoumou, G. Milne, V. Garcés-Chavéz, S. A. Tatarkova, W. Sibbett, F. J. Gunn-Moore, P. E. Bryant, A. C. Riches, and K. Dholakia. Light-induced cell separation in a tailored optical landscape. *Applied Physics Letters*, 87(12):123901, 2005.
- [108] D. M. Gherardi, A. E. Carruthers, T. Čiřmár, E. M. Wright, and K. Dholakia. A dual beam photonic crystal fiber trap for microscopic particles. *Applied Physics Letters*, 93(4):041110, 2008.
- [109] A. S. Zelenina, R. Quidant, G. Badenes, and M. Nieto-Vesperinas. Tunable optical sorting and manipulation of nanoparticles via plasmon excitation. *Optics Letters*, 31(13):2054–2056, 2006.
- [110] R. Quidant, S. Zelenina, and M. Nieto-Vesperinas. Optical manipulation of plasmonic nanoparticles. *Applied Physics A - Materials Science & Processing*, 89(2):233–239, 2007.
- [111] S. Kawata and T. Sugiura. Movement of micrometer-sized particles in the evanescent field of a laser-beam. *Optics Letters*, 17(11):772–774, 1992.
- [112] J. Leach, H. Mushfique, S. Keen, R. Di Leonardo, G. Ruocco, J. M. Cooper, and M. J. Padgett. Comparison of Faxen’s correction for a microsphere translating or rotating near a surface. *Physical Review E*, 79(2):026301, 2009.
- [113] K. Wang, E. Schonbrun, P. Steinvurzel, and K. B. Crozier. Scannable plasmonic trapping using a gold stripe. *Nano Letters*, 10(9):3506–3511, 2010.
- [114] V. Garcés-Chavéz, R. Quidant, P. J. Reece, G. Badenes, L. Torner, and K. Dholakia. Extended organization of colloidal microparticles by surface plasmon polariton excitation. *Physical Review B*, 73(8):085417, 2006.
- [115] M. Plöschner, M. Mazilu, T. Čiřmár, and K. Dholakia. Numerical investigation of passive optical sorting of plasmon nanoparticles. *Optics Express*, 19:13922–13933, 2011.
- [116] V. Demergis and E. Florin. High precision and continuous optical transport using a standing wave optical line trap. *Optics Express*, 19(21):20833–20848, 2011.
- [117] M. Mazilu, J. Baumgartl, S. Kosmeier, and K. Dholakia. Optical eigenmodes; exploiting the quadratic nature of the energy flux and of scattering interactions. *Opt. Express*, 19(2):933–945, Jan 2011.
- [118] K. Svoboda and S. M. Block. Biological applications of optical forces. *Annual Review of Biophysics and Biomolecular Structure*, 23:247–285, 1994.

- [119] M. Plöschner, M. Mazilu, T. Čižmár, and K. Dholakia. Passive optical sorting of plasmon nanoparticles: Numerical investigation of optimal illumination. *AIP Conf. Proc.*, 1398:85–87, 2011.